UC Berkeley
UC Berkeley Electronic Theses and Dissertations

Title
Understanding and Controlling the Optical Properties of Quasi Two-Dimensional Materials

Permalink
https://escholarship.org/uc/item/1g99q98r

Author
Cao, Ting

Publication Date
2018

Peer reviewed|Thesis/dissertation

eScholarship.org Powered by the California Digital Library
University of California

Understanding and Controlling the Optical Properties of Quasi Two-Dimensional Materials

by

Ting Cao

A dissertation submitted in partial satisfaction of the

requirements for the degree of

Doctor of Philosophy

in

Physics

in the

Graduate Division

of the

University of California, Berkeley

Committee in charge:

Professor Steven G. Louie, Chair
Professor Jeffrey Neaton
Professor Ali Javey

Fall 2018

Understanding and Controlling the Optical Properties of Quasi Two-Dimensional Materials

Copyright 2018

by

Ting Cao

Abstract

Understanding and Controlling the Optical Properties of Quasi Two-Dimensional Materials

by

Ting Cao

Doctor of Philosophy in Physics

University of California, Berkeley

Professor Steven G. Louie, Chair

In this thesis, I discuss the understanding and control of the optical properties of quasi-two-dimensional materials, an emerging field since the discovery of graphene. This thesis not only aims to understand and predict the distinct optical properties of quasi-two-dimensional materials from theoretical and numerical approaches, but also incorporates and quantitatively explains relevant experimental data when available. This thesis is organized as follows:

- In the first chapter, I give a brief background overview on 1) research on excited states in general, 2) first-principles GW-BSE method that calculates the electron quasiparticle bands and exciton properties, and 3) recent progress on the optical properties of two-dimensional semiconductors and light-matter interactions in these materials.
- In the second chapter, I review the valley physics in transition metal dichalcogenide monolayers [1, 2], which builds the foundation of the more advanced topics that we discuss in the next chapters.
- In the third chapter, I present several studies on the unusual optical properties of transition metal dichalcogenide monolayers arising from the novel exciton physics, including strongly-bound non-hydrogenic exciton series [3], light-like exciton dispersion [4], and magnetic brightening of the dark states [5]. These results show the distinct optical properties of two-dimensional semiconductors compared with those in other dimensions.
- In the fourth chapter, I demonstrate some consequences of topological effects on optical transitions in two-dimensional semiconductors [6], which leads to a new set of optical

selection rules dictated by the winding number of interband optical matrix elements. The new selection rules go beyond the selection rules for conventional semiconductors which have been used for over 6 decades [7], and explains the experimental results on the photo-current spectroscopy of gapped bilayer graphene [8].

- In the last chapter, I present materials engineering aspects of two-dimensional materials via van der Waals interfacial engineering. We show that by changing the interlayer stacking configurations and by applying out-of-plane electric fields, the electronic and optical properties of van der Waals layers can be rationally engineered and controlled [9, 10].

To the long lasting friendship between China and the United States

Contents

Contents **ii**

List of Figures **iv**

List of Tables **xi**

1 Introduction **1**
1.1 Excited-State Quantum Phenomena in Materials 1
1.2 The GW-BSE Method 2
1.3 Excite-State Quantum Phenomena and Light-Matter Interactions in Two-dimensional Materials 5

2 Valley Physics in Two-Dimensional Materials **7**
2.1 Valley-Selective Circular Dichroism in Transition Metal Dichalcogenide Monolayers 7
2.2 Valley Hall Effect in Transition Metal Dichalcogenide Monolayers 12

3 Exciton Physics in Two-Dimensional Materials **14**
3.1 Stongly Bound Excitons in WS_2 Monolayers 14
3.2 Exciton Dispersions in Transition Metal Dichalcogenide Monolayers 19
3.3 Exciton Dark States and Magneto-Optics in Transition Metal Dichalcogenide Monolayers 29

4 Topological Effects and Optical Selection Rules **34**
4.1 A New Selection Rule at Two-Dimensions: Topology and Winding Numbers 35
4.2 Applications of the Selection Rule: Gapped Graphene Systems 38
4.3 The Experimental Probe of Excitons in Gapped Bilayer Graphene and Other Proposed Experiments 45

5 Van der Waals Engineering of Optical Transitions **48**
5.1 Twist-Angle Dependent Optical Properties of Transition Metal Dichalcogenide Bilayers 49
5.2 Electric Field Tunable Optical Properties of Black Phosphorus Bilayers . . . 55

Bibliography **65**

List of Figures

1.1 The crystal structure of monolayer MoS_2. (a) Coordination environment of Mo (blue sphere) in the structure. Sulfur is shown as golden spheres. (b) A top view of the monolayer MoS_2 lattice, emphasizing the connection to a honeycomb lattice. 6

2.1 Valley-selective circular dichroism of monolayer MoS_2. (a) Top valence band (blue) and bottom conduction band (pink). The center hexagon is the Brillouin zone color-coded by the degree of circular polarization, $\eta(\boldsymbol{k})$, as defined in the text. The vector connecting K (K_+) and K' (K_-) is perpendicular to Mo-S bond in the crystal structure in Fig. 1.1 b. (b) Schematic of phase winding on the MoS_2 lattice that gives rise to the chiral optical selectivity. Left panel: the contribution to phase winding from the Bloch lattice phase, where $\tau = \pm 1$ is the valley index, and $s = 1, 2$ corresponding to the S and Mo sites (isospin index). Right panel: the phase winding under a three-fold rotation. The green axes indicate the rotation of local atomic coordinates that leads to the azimuth dissynchronization. 10

2.2 The blue curve corresponds to the top of valence bands. The red curve corresponds to the bottom of conduction bands. The Berry curvatures of the states along the $K'(K_-) - \Gamma - K(K_+)$ path of the Brillouin zone are plotted. The value of Berry curvature is large for the conduction band at the zone centre, where bands are degenerate. 13

3.1 (a), The optical absorption of the A (black) and B (red) exciton series considering electron-hole interaction. The blue curve is the optical absorption spectrum, obtained without considering electron-hole interaction, where the quasiparticle bandgap is about 2.7 eV (blue arrow). The excitonic states of A and B exciton series, with electron-hole interaction included, are calculated (shown in (b)-(f), see below) and labeled (in a) by black and red arrows, respectively, up to 2.5 eV. The computed $1s$, $2p$ and $3p$ states of the A exciton are at 2.05 eV, 2.28 eV and 2.49 eV, respectively, and are in excellent agreement with the experimental measurements. Although the orbital notation of a two-dimensional hydrogen atom is adopted to label the exciton states, the excitonic series significantly deviates from a hydrogenic series, as discussed in the main text. The degeneracy labels in the superscript include both the degeneracy of valleys and orbital angular momentum. (b)-(f), The plots are modulus squared of the real-space exciton wavefunction projected onto the WS_2 plane, with the hole position fixed near a W atom at the center of the plot. These wavefunctions share similar in-plane nodal structures with the excited states in a hydrogen atom, and therefore enable the eigenstates to be labeled with a principal and an orbital quantum number. The Wannier nature of the excitons is clear, with the radii much larger than the unit cell. The color scale is the normalized wavefunction probability and applies to panels (b)-(f). 16

3.2 Two-photon absorption (blue) and one-photon absorption (green) spectra are measured in single-layer WS_2 at 10 K. In the two-photon absorption spectrum, $2p$ and $3p$ resonances are observed at 2.28 eV and 2.48 eV, respectively, on top of a plateau background. For comparison, the one-photon absorption spectrum, measured as the relative reflectance signal ($\delta R/R$), exhibits no corresponding features except a B exciton ($1s$) related absorption resonance at 2.45 eV. Additionally, the A exciton ($1s_{ex}$) and trion ($1s_{tr}$) absorption peaks are detected consistently with the two-photon luminescence peaks, with a 20 meV Stoke shift, and are marked at 2.04 and 2 eV, respectively, by black dashed lines. The energy difference between the A exciton 1s state emission peak and the 3p state absorption peak is 0.44 eV, which yields the lower bound for the exciton binding energy in monolayer WS_2. This binding energy is extraordinarily large for a Wannier exciton, and implies a dominating excitonic mechanism for the intense light-matter interaction in two-dimensional transition metal dichalcogenides. The total excitation scan is achieved by tuning an output beam of an optical parametric oscillator over a 600 meV span, with a scanning resolution of about 15 meV. Similar results are repeated in more than 5 flakes. 18

3.3 (a), Quasiparticle band structure of monolayer MoS_2. Lowest energy transitions corresponding to electron-hole excitations with momentum transfers of $\boldsymbol{Q} = 0$ and $\boldsymbol{Q} = \boldsymbol{K}$ are shown with the labeled arrows. (b-c), Schematics of interactions between two electron-hole pairs with momentum near $\boldsymbol{Q} = 0$, corresponding to BSE matrix elements $\langle cv, \boldsymbol{kQ}|\hat{K}^{eh}|c'v', \boldsymbol{k'Q}\rangle$ for (b), two like-spin transitions within one valley and (c), two like-spin transitions from different valleys. (d), Schematic of two electron-hole pairs with momentum near $\boldsymbol{Q} = \boldsymbol{K}$ giving rise to BSE matrix elements for like-spin transitions. 21

3.4 Exciton dispersion of monolayer MoS_2 near (a), $\boldsymbol{Q} = 0$ and (b), $\boldsymbol{Q} = \boldsymbol{K}$ along the $K - \Gamma - K'$ direction. Red (blue) lines indicate states arising from like-spin (unlike-spin) transitions. The label A refers to states involving transitions from the highest valence band at K and K'. "B" states involving transitions from the second highest valence band are similar and shown in the Supplemental Material of [4]. 22

3.5 (a) Closeup of dispersion of A_{1s} near $\boldsymbol{Q} = 0$. first-principles results are stars. Fit to effective Hamiltonian (Eq. 3.12) are solid lines. Red (blue) lines indicate states arising from like-spin (unlike-spin) transitions. (b) Valley pseudospin texture of the (upper) nonanalytic like-spin transition band around $\boldsymbol{Q} = 0$ for states of fixed energy in $\boldsymbol{Q}$ space. (c) Valley pseudospin texture of the (lower) parabolic like-spin transition band. (d) Optical absorbance of linearly polarized light at fixed incidence as the polarization vector $\hat{\boldsymbol{e}}$ is rotated over 360°. The angle of the polarization vector, θ', is defined with respect to the vector formed by the intersection of the polarization plane (blue) and the $x - y$ plane. Red (black) indicates the absorbance of states arising from the lower (upper) like-spin band. (e) Energy difference between the upper and lower like-spin bands that is probed as ϕ, the angle between the wave vector of light and the z axis is changed, for light of $\hbar\omega \approx 2eV$. The inset shows how θ, ϕ, and θ' are defined. 27

3.6 (a), False-color plot of the measured emission spectrum for monolayer WSe_2 at a temperature of 30 K as a function of the strength of the applied $\boldsymbol{B}_{\parallel}$. The displayed energy range includes emission from the neutral A exciton (X_0) and the associated trion state (X_T). Emission features from the dark exciton (X_D) and dark trion (X_{DT}) grow with increasing $\boldsymbol{B}_{\parallel}$. The scale bar represents the normalized photoluminescence intensity. (b), For monolayer WSe_2, electrons in the lower conduction band (CB2) have spin opposite that in the upper valence band (VB), rendering the lowest transition optically dark. Only transitions from the upper CB (at energy $h\nu_0$) are allowed. The spin-split CBs, CB1 and CB2, can be described as the result of an effective out-of-plane magnetic field $\boldsymbol{B}_{int}$ acting on the electron magnetic moment. The blue and red lines represent bands with electrons' spin up and down, respectively. The arrows indicate the spin of the electron/hole in an excitonic state. (c), Under an external in-plane magnetic field $B_{\parallel}$, the total effective field $\boldsymbol{B}_{eff} = \boldsymbol{B}_{int} + \boldsymbol{B}_{\parallel}$ is tilted away from the surface normal, resulting in tilted spin polarization of the CB electrons. Optical transitions at energy $h\nu_D$ from an exciton formed mainly from the lower CB and corresponding to the dark exciton then become weakly allowed. 31

3.7 The blue and red lines represent spin-up and spin-down bands, respectively. (a), The spin-valley configuration of neutral bright and dark excitons. ΔE_{CB} denotes the energy splitting of the two CBs. The black line represents the e-h exchange interaction E^x for the ($S_z = 0$) bright exciton, which is absent for the ($S_z = \pm 1$) dark exciton. (b), Spin-valley configuration of the lowest-energy n-type bright and dark trion states. An e-h exchange interaction $E^{x'}$ is present for the intervalley ($S_z = 0$) e-h pair, as shown. 32

4.1 Schematic structures of gapped graphene systems. (a) Structure of monolayer graphene with inequivalent sublattices. The carbon atoms on top of boron and nitrogen atoms are colored white and grey, respectively. The hexagonal boron nitride monolayer placed below the graphene layer makes the two graphene sublattices inequivalent. (b, c) Structure of Bernal-stacked bilayer and rhombohedral- (ABC-) stacked trilayer graphene. The dashed lines represent vertical carbon bonds between neighboring layers. The carbon atoms forming these bonds are colored black 38

4.2 Calculated band structure and pseudospin (orbital components) winding of gapped graphene systems. Bottom conduction band and top valence band of monolayer graphene with broken A and B sublattice symmetry (a), biased Bernal-stacked bilayer graphene (b), and biased rhombohedral-stacked trilayer graphene (c). Red solid lines and black dashed lines are GW and DFT-LDA bands, respectively. The K point is set at $k = 0$. Positive and negative k values denote the $K - \Gamma$ and $K - M$ direction, respectively. (d) Orbital pseudospin winding in biased bilayer graphene. Inset: Structure of biased bilayer graphene. The carbon atoms forming bonds with a neighboring layer are colored black. 40

4.3 $K-$valley interband optical transition matrix elements and $1s$ exciton envelope function in $\boldsymbol{k}$-space. The K point is placed at the origin. Optical interband transition matrix element and its winding number for light of (a) left circular polarization $p_{\boldsymbol{k}_+}$ and (b) right circular polarization $p_{\boldsymbol{k}_-}$ in monolayer graphene with inequivalent sublattices. The direction and length of an arrow denote, respectively, the phase and the magnitude of the corresponding matrix element. (d) $p_{\boldsymbol{k}_+}$ and (e) $p_{\boldsymbol{k}_-}$ in biased bilayer graphene. (g) $p_{\boldsymbol{k}_+}$ and (h) $p_{\boldsymbol{k}_-}$ in biased trilayer graphene. (c),(f),(i) $1s$ exciton envelope function in $\boldsymbol{k}$-space in gapped monolayer graphene, biased bilayer graphene, and biased trilayer graphene, respectively. The envelope functions show in color scale the magnitude of the free electron-hole pair excitation at each $\boldsymbol{k}$, normalized to its largest value in each plot. 41

4.4 K-valley and K'-valley exciton energy levels and valley-exciton selective circular dichroism in (a) monolayer graphene with inequivalent A and B sublattices, (b) biased bilayer graphene, and (c) biased-trilayer graphene. Left (right) part of each panel depicts the K-valley (K'-valley) exciton energy levels. The first six lowest-energy excitons are shown in each plot. Black lines indicate dark states (with maximum oscillator strength $< 1\%$ of the brightest exciton in each plot). The oscillator strength (I) of each bright state is expressed in terms of that of the brightest state, for unpolarized light. Blue and red lines (or circles) indicate bright states that are excitable from the ground state with left- and right- circularly polarized light, respectively. 44

4.5 (a) Normalized photocurrent spectrum at displacement field D = 0.69, 1.03, and 1.37 V/nm in gapped bilayer graphene. Both exciton peaks blue-shift as D increases and the bandgap opens more. All spectra converge to a line at energies above the higher-energy peak. (b) Calculated optical absorbance as a function of energy at D = 1.3 V/nm in gapped bilayer graphene. 45

4.6 In gapped bilayer graphene, (a) schematic optical excitation and photoluminescence in the K valley using resonant σ_- excitations of the $1s$ exciton; (b) schematic optical excitation and photoluminescence in the K valley using resonant σ_+ excitations of the $2p$ exciton. 47

5.1 (a) Schematics of MoS_2 bilayers with AA, AB and different twisted configurations. Mo atoms are shown as green spheres; two S atoms of the same horizontal position are presented by one yellow sphere. Interlayer distance variations are exaggerated for illustration. The interlayer separation is ~ 0.61 nm for AA_1 and AB_1 stacking, ~ 0.62 nm for AB_2 stacking, ~ 0.68 nm for AA_3 and AB_3 stacking and ~ 0.65 nm for the four twisted bilayers. (b) Calculated values for the Kohn-Sham K-valley direct bandgap (orange) and indirect bandgap (dark yellow) for the energetically favorable structures at each twist angle. (c) The calculated Kohn-Sham bandgap as a function of the interlayer distance for different stacking configurations (symbols). The dashed curve shows the bandgap values for AA_1 stacking with artificially varied interlayer separation. Their comparison indicates that the electronic coupling in MoS_2 bilayer is largely determined by the interlayer separation and does not depend explicitly on the horizontal registration of the two layers. 50

5.2 (a) Photoluminescence spectra of MoS_2 monolayer and bilayers with twist angles of $\theta = 0°$, $15°$ and $60°$. (b) Dependence of photoluminescence peak energies on the twist angle for 44 MoS_2 bilayers. The peak I energy is almost identical for all bilayers. The peak II energy is lowest for AA- and AB-stacked bilayers, and is higher but at a nearly constant value for other twist angles. (c,d) Calculated Kohn-Sham band structure of a MoS_2 monolayer using the local density approximation (c) and of the most energetically favorable AA-stacked bilayer (d). Transition I is associated with the K-valley direct bandgap (peak I in photoluminescence spectra). The indirect bandgap transitions II and II have nearly degenerate energy and either may be associated with the peak II in the photoluminescence spectra. 52

5.3 Structure and electronic structure of $90°$ twisted bilayer black phosphorus. (a) Structure of a $90°$ twisted bilayer black phosphorus. The phosphorus atoms in the top and bottom layers are colored by cyan and purple, respectively. The interlayer distance is 3.3 Å from first-principles density functional theory calculations using the PBE functional with a van der Waals correction. (b) Schematic of the Brillouin zone of bilayer black phosphorus in its natural stacking order (rectangle) and the Brillouin zone of a 5×7 supercell of $90°$ twisted bilayer black phosphorus (shaded square). (c) GW quasiparticle band structure of naturally stacked bilayer black phosphorus. (d) GW quasiparticle band structure of $90°$ twisted bilayer black phosphorus, with the color representing the layer localization function defined in the main text. (e, f) Contour plots of the wave functions of (e) The valence band maximum and (f) the conduction band minimum of a monolayer black phosphorus at a height of 1.6 Å above the phosphorus atoms, respectively. The wave function is normalized to its maximum amplitude in each plot. The solid and dashed lines represent positive and negative values of the wave functions, respectively. The solid and hollow purple circles denote the phosphorus atoms at the top and bottom of a monolayer, respectively. 56

5.4 Top valence band and bottom conduction band in the first Brillouin zone of 90° twisted black phosphorus bilayer. A three-dimensional plot (energy vs. in-plane wavevector) of the top valence band and the bottom conduction band are shown. 57
5.5 Electronic structure of the 90° twisted bilayer black phosphorus under out-of-plane electric displacement field. (a,b) GW quasiparticle band structure of the 90° twisted bilayer black phosphorus in a perpendicular electric displacement field of 0.2 V/Å and -0.2 V/Å, respectively. The color represents the layer localization function defined in the main text. (c,d) Schematics of effective mass under electric displacement field of (c) 0.2 V/Å and (d) -0.2 V/Å. The hole and electron effective masses are shown in white and black, respectively. The effective masses are in unit of the bare electron mass. The green arrow denotes the direction of the displacement field. (e) Splitting of the 2-fold degenerate valence band maximum (VBM) as a function of the electric displacement field. The lines are visual guides. (f) The change in bandgap as a function of the electric displacement field. Red squares and black circles denote the bandgap change in 0° naturally stacked bilayer and 90° twisted bilayer, respectively. The lines are visual guides. 60
5.6 Optical transitions of the 90° twisted black phosphorus bilayer under different electric displacement field from first principles. (a) Schematic of optical transitions from VBb states to CB states (blue arrow) and VBt states to CB states (red arrow) under the electric displacement field of 0.2 V/Å. (b) Oscillator strength of optical transitions from VBb-CB (blue) and VBt-CB (red) at Γ as a function of the direction of the light polarization. The oscillator strength is plotted in arbitrary unit as a function of the polarization angle, with 0° along the x axis, and 90° along the y axis. (c) Optical absorption spectra of linearly polarized light along x-axis (red) and y-axis (blue) under electric displacement field from -0.2 V/Å to 0.2 V/Å. 62

List of Tables

5.1 Calculated interlayer distance of MoS_2 bilayers in different configurations. 54

Acknowledgments

I thought I would have a lot to say in this acknowledgment to memorize my six years at graduate school. However, after struggling for a while, it seems that words fall short when these colorful days start to flash in my memory.

First, I would like to thank Professor Steven Gwon Sheng Louie, my advisor. Thank you for landing me at the leading edge of condensed matter physics and materials science; for inspiring me to think independently and critically about physics; for challenging me to work on the most important yet difficult problems; for training me to be a responsible scientist; for helping me through all the hardship in a foreign country; for enlightening me on a future career path. Thank you, all in all, for being my academic advisor.

To all the (theory) comrades with whom I have been working along in the Louie group: Andrea, Brad, Chin-Shen, Derek, Diana, Fangzhou, Felipe, Gabriel, Jamal, Jingwei, Johannes, Liang, Meng, Sang, Sinisa, Yang-Hao, Yea-Lee, Zhenglu. You are the best. I will miss the laughter, the readings and papers, the stories, and the happy hours that we shared. I hope you a bright future, in academia or beyond.

To my (experiment) collaborators at Berkeley (many have already started their own group all around the world): Chen Chen, Yen-Chia Chen, Michael Crommie, Felix Fischer, Graham Fleming, Cheng Gong, Danny Haberer, Xiaoping Hong, Chenhao Jin, Trinity Joshi, Long Ju, Jonghwan Kim, Kaihui Liu, Giang Nguyen, Zahra Pedramrazi, Ziqiang Qiu, Daniel Rizzo, Sufei Shi, Feng Wang, Ying Wang, Jun Xiao, Ziliang Ye, Yu Ye, Liming Zhang, Xiang Zhang, Qin Zhou, Hanyu Zhu. When reviewing my scientific publications at Berkeley, I realize that more than half of them were published together with you. These exciting discoveries help put Berkeley at the top of the field. From you, I learned so much more about realistic science, academic skills, and academic life.

To Anne, Katherine, and Arica, thank you for the sincere help and support during my graduate school.

To my collaborators outside Berkeley: Tony Heinz, Qian Niu, Lei Wang, Shiwei Wu, Xiaoxiao Zhang. You expanded not just my social networks. I think much broader about research, academia, and life, because of you.

To Enge Wang and Ji Feng. Without your help, advice, and recommendations, I would never have a chance gotten into Berkeley, not to say discovering such a whole new world in life. I fulfilled my wish of studying condensed matter physics using computational approaches here.

To my parents, grandparents, and families. Thank you for all the unconditional support and

understandings.

To Yi. There are so many differences between physics and psychology, between a male and a female, between a northerner and a southerner, between UC Berkeley and BGSU, and between the "big rural area" and the SF bay. But we have gone through similar ups and downs, and gone after similar goals, in undergraduate and graduate schools. Academia is as hard for us. Life is as hard for us. Isn't it amazing that we have had each other all along this path?

Chapter 1

Introduction

1.1 Excited-State Quantum Phenomena in Materials

Excited states describe the quantum states of a system, which have higher energies than the ground state. The behaviors of excited states not only give rise to various fascinating properties and phenomena in condensed matter, but also play vital roles in modern technologies such as electronics, optoelectronics, and energy generation and harvesting.

Although prominent discoveries in solid state physics of the 20th century have been made largely in the research of condensed matter systems at (or loosely speaking, at an energy close to) the ground state (See, for example [11–14]). The past several decades have seen a surge in the research of the excited state phenomena in materials systems. The excited states, on the one hand, carry all the beauty and complexity just like the ground state does, such as symmetry, topological phases, and electron-electron interactions; on the other hand, they contain much more information in the energy and time domain than a ground state (e.g., naively speaking, there are infinite number of excited states of a real material system). As a result, the development of this field requires great efforts challenging both theorists and experimentalists.

The theoretical studies of the excited-state phenomena come with significant diversity of the research methodology and philosophy. For example, the studies of the the Sachdev-Ye-Kitaev model usually employ analytical and numerical calculations of ensemble properties [15, 16], yet the quasiparticles are no longer good approximations in this model; the studies of periodically (in time) driven systems sometimes uses the Floquet theory which maps the Hamiltonian into a quasi-stationary one [17], and greatly simplifies the problem; the research of solar cells involves modelling of photocarrier dynamics using time-dependent density functional theory calculations [18], which render real-time evolution of the photocarrier wavefunction and dictate the solar-energy conversion process.

In this thesis, we focus on the excited-state quantum phenomena of real materials. By coupling light with materials, study of optical excitations has enable research on excited states to make numerous fascinating discoveries. As part of this dissertation research, we present a variety of highly unexpected light-matter phenomena, as well as novel optical selection rules owing to topological effects, in atomically thin two-dimensional materials.

Despite these discoveries and findings, many interesting questions and challenges in this area have emerged and remain much unexplored: Can excitons form different orders in different dimensions? How does band topology affect light-matter interactions in other processes? Is there a unified first-principles theory of excited-state dynamics at varying temporal and spatial scales? We expect the research of these topics to benefit from the further development of methodologies in quantum many-body physics and statistical physics, materials modelling, and high-performance computing.

1.2 The GW-BSE Method

The excited-state properties of an interacting many-electron system, at the first glance, could be solved by direct diagonalization of the system's Hamiltonian and calculations of the expectation values of certain operators. However, this approach is almost impossible to implement due to the large number of electrons (that lead to exponentially growing size of basis sets) and the infinite number of eigenstates that exist in a realistic physical system. The GW-BSE method investigates one- and two-particle excited-state properties using a many-body perturbation theory based on the Green's function formalism [19–22]. This method significantly reduces the computational cost of the quasiparticle and exciton energies compared with many other methods, while remains accurate for systems with weak and medium electron correlations [23, 24]. (For the ground states, several standard numerical approaches, such as the density functional theory [25, 26] and quantum Monte Carlo method [27], have been successfully applied to a variety of physical systems ranging from molecules to solids.)

Since the GW-BSE method is based on the Green-function theory, the central quantities of interests are therefore the propagators. For the single-particle properties, we have

$$G_1(1,2) \equiv -i \langle N,0|T(\hat{\psi}(1)\hat{\psi}^\dagger(2))|N,0\rangle \tag{1.1}$$

This single-particle Green's function is relevant to the properties of quasi-electron and quasi-hole. In the two-particle case,

$$G_2(12,1'2') \equiv -i \langle N,0|T(\hat{\psi}(1)\hat{\psi}(2)\hat{\psi}^\dagger(2)\hat{\psi}^\dagger(1'))|N,0\rangle \tag{1.2}$$

This two-particle Green's function is relevant to the properties of excitons (and other forms of two-particle excitations). Here, the state $|N, 0\rangle$ is the ground state of the N-electron system. $\hat{\psi}$ and $\hat{\psi}^\dagger$ are the annihilation and creation operators of electrons. We have used the time-ordered Green's functions in this section. The labels 1, 2, $1'$, and $2'$ contain information about position, spin, and time of an electron.

The Green's functions, in general, can be solved by the Dyson-like equations, if the form of interactions is known. For example, for the single-particle Green's function, we have,

$$G_1(1,2) = G_1^0(1,2) + G_1^0(1,3)\Sigma(3,4)G_1(4,2), \tag{1.3}$$

where $\Sigma(3,4)$ is the self-energy operator, and is also the "kernel" of the Dyson-like equation. $G_1^0(1,2)$ is a "non-interacting" Green's function obtained by mean-field calculations, such as the density functional theory calculations. In this section, unless we note otherwise, the repeated indices are implicitly summed over.

In the GW approximation [19, 20], the self energy Σ is approximated as,

$$\Sigma(1,2) = iG_1(1,2)W(1^+,2) \tag{1.4}$$

where

$$W(1,2) = v(1,2) + v(1,3)P(3,4)W(4,2) \tag{1.5}$$

and

$$P(1,2) = -iG_1(1,2^+)G_1(2,1) \tag{1.6}$$

where v is the bare Coulomb interaction.

Calculations using these nested equations above will give rise to a self-consistent single-particle Green's function of the system. However, this self-consistent solution is not only computationally intensive, but in general does not give the optimal quasiparticle energy spectra compared with the experimental data (we note here that this point of view is currently debated in the community). In this thesis, we use the so called G_0W_0 method [20], where the above equations are casted into a one-shot calculation of the quasiparticle self energy:

$$\Sigma(1,2) = iG_1^{0,DFT}(1,2)W^0(1^+,2) \tag{1.7}$$

where

$$W^0(1,2) = \frac{v(1,3)}{\epsilon(3,2)} \tag{1.8}$$

Here, $\epsilon(3,2)$ is the dielectric matrix [20], which can be constructed from the wavefunctions and energy spectrum obtained from a mean-field calculation. The term $W^0(1,2)$ thus carries the explicit meaning of the screened Coulomb interaction. The non-interacting Green's function $G_1^{0,DFT}$ is constructed from the wavefunctions obtained from density functional theory calculations.

There is an important assumption in using the G_0W_0 method to calculate the quasiparticle energies: we assume that long-lived particle-like excitations exist, which appear as well-defined sharp peaks (or as poles) in the spectrum of $G_1(1,2)$ and $G_1^0(1,2)$. With this assumption, the equation of motion for the quasiparticle reads,

$$H^{DFT}\psi_n(\boldsymbol{r}) + \int d\boldsymbol{r'}[\Sigma(\boldsymbol{r},\boldsymbol{r'},\epsilon_n) - v_{xc}(\boldsymbol{r'})]\psi_n(\boldsymbol{r'}) = \epsilon_n\psi_n(\boldsymbol{r}) \tag{1.9}$$

where ψ_n is the quasiparticle wavefunction with its self energy Σ taken from Eq. 1.7, v_{xc} the exchange-correlation potential from the mean-field density functional theory calculations. Within the lowest order perturbation theory, the quasiparticle energy under the G_0W_0 approximation is,

$$E_n^{QP} = E_n^{DFT} + \langle\psi_n|\Sigma(E_n^{DFT}) - v_{xc}|\psi_n\rangle \tag{1.10}$$

where the wavefunction ψ_n is taken from the mean-field density functional theory calculations.

In the BSE approach, the Dyson-like equation of the two-particle correlation function is,

$$L(12;1'2') = L_0(12;1'2') + L_0(14;1'3)K(35;46)L(62;52'), \tag{1.11}$$

called the Bethe-Salpeter equation (BSE). Here, the non-interacting $L_0(12;1'2')$ is equal to $G_1(1,2')G_1(2.1')$, describing the non-interacting quasielectron-quasihole propagation.

In the quasiparticle basis, the BSE can be casted into an eigenvalue problem [22],

$$A^S_{cv,\boldsymbol{k}}(E_{c,\boldsymbol{k}} - E_{v,\boldsymbol{k}}) + \Sigma_{c'v',\boldsymbol{k'}}A^S_{c'v',\boldsymbol{k'}}\langle cv,\boldsymbol{k}|\hat{K}^{eh}|c'v',\boldsymbol{k'}\rangle = A^S_{cv,\boldsymbol{k}}\Omega^S, \tag{1.12}$$

where $\hat{K}^{eh}$ is the interacting kernel, including an exchange term and direct term [22]. $A^S_{cv,\boldsymbol{k}}$ gives the amplitude of each free electron-hole transition at $(cv, \boldsymbol{k})$, contributing to the exciton state. Ω^S is the transition energy of an excitonic state. Here, we have assumed that electron part and hole part of the exciton wavefunction come from the conduction bands and the valence bands, respectively. The full derivation of Eq. 1.12 can be found in [22]. The physical meaning and consequences of Eq. 1.12 will be discussed in chapters III and IV.

The optical activity of an exciton S is given by its oscillator strength I^S_e ($\boldsymbol{e}$ is the photon polarization unit vector), which is

$$I^S_e = \frac{2|\Sigma_{cv,\boldsymbol{k}} A^S_{\boldsymbol{cv},\boldsymbol{k}} \boldsymbol{e} \cdot \langle \phi_{c,\boldsymbol{k}} | \hat{\boldsymbol{p}} | \phi_{v,\boldsymbol{k}} \rangle|^2}{\Omega^S} \tag{1.13}$$

The oscillator strength is a critical quantity to many results presented in this thesis, and will be discussed in chapters III, IV, and V.

1.3 Excite-State Quantum Phenomena and Light-Matter Interactions in Two-dimensional Materials

As introduced in section I, the research on the excited-state phenomena covers many domains of science. This thesis will focus on a specific topic, i.e., the optically excited states in two-dimensional semiconductors, and how optical properties of two-dimensional semiconductors are affected and related to these optically excited states. This research topic is particularly interesting, because the two-dimension nature of materials gives distinct symmetries, greater tunability, and enhanced electron-electron (and electron-hole) interactions compared with conventional three-dimensional semiconductors such as GaAs.

Our first example of two-dimensional semiconductors is monolayer MoS_2. Since its first isolation [28, 29], monolayer MoS_2 has attracted immense attention. Many measurements have been performed to characterize the optical and transport properties of this material (See, for example [28–30]). In monolayer MoS_2, the two outside layers of sulfur atoms in a two-dimensional hexagonal lattice are stacked over each other in an eclipsed fashion. Each Mo sits in the center of a trigonal prismatic cage formed by 6 sulfur atoms (Fig. 1.1 a). Quite remarkably in the context of this thesis, the natural stable structure of free-standing monolayer MoS_2 is a honeycomb lattice with inequivalent bipartite coloring, breaking the inversion symmetry (Fig. 1.1 b). Such breaking of the inversion symmetry is related to the valley physics and new selection rules that we will discuss in the following chapters.

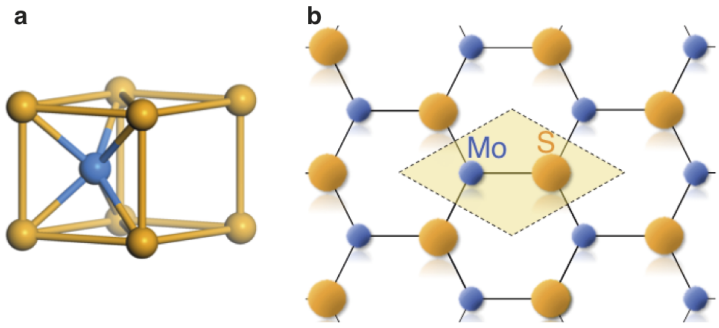

Figure 1.1: The crystal structure of monolayer MoS_2. (a) Coordination environment of Mo (blue sphere) in the structure. Sulfur is shown as golden spheres. (b) A top view of the monolayer MoS_2 lattice, emphasizing the connection to a honeycomb lattice.

Including MoS_2, the transition metal dichalcogenide monolayers MX_2 (M = Mo, W; X = S, Se), as a group, have recently emerged as an important class of two-dimensional materials with potential for electronic and optoelectronic applications. Unlike semi-metallic graphene, the layered transition metal dichalcogenides in the 2H form have a sizable bandgap [28, 30]. More interestingly, when thinned down to a monolayer, these transition metal dichalcogenides transform from indirect-bandgap to direct-bandgap semiconductors [28, 30], exhibiting a number of intriguing optical phenomena such as valley-selective circular dichroism [1, 2], doping-dependent charged excitons [31] and strong photocurrent responses [32]. In chapter III, we will discuss the excitonic origin underlying such a strong light-matter interaction, and show the distinct behavior of excitons in this materials family.

Chapter 2

Valley Physics in Two-Dimensional Materials

The study of two-dimensional semiconductors has received significant attention over the last decade, partially due to the valley physics and related phenomena discovered and experimentally demonstrated originally in monolayer transition metal dichalcogenides [1, 2, 33, 34]. In this chapter, we will review the study of the valley physics, especially the valley-selective circular dichroism, in monolayer transition metal dichalcogenides [1, 2]. These studies build the foundation of unusual optical selection rules and excitonic physics that we discuss in chapter III and chapter IV.

2.1 Valley-Selective Circular Dichroism in Transition Metal Dichalcogenide Monolayers

A two-dimensional honeycomb lattice harbors a pair of inequivalent electronic band valleys in the $\boldsymbol{k}$-space electronic structure, in the vicinities of the vertices of a hexagonal Brillouin zone, K and K'. It is particularly appealing to exploit this emergent degree of freedom of charge carriers, in what is termed "valleytronics". The physics of valleys mimics that of spin, and will make possible devices, analogous to spintronics, such as valley filter and valve, and optoelectronic Hall devices, all very promising for next-generation electronics. The key challenge lies with achieving high degree of valley polarization, of which a convincing demonstration in a two-dimensional honeycomb structure remains evasive. We show in this section, using first-principles calculations, that monolayer MoS_2 is an ideal material for valleytronics, for which valley polarization is achievable via valley-selective circular dichroism arising from its unique symmetry [1]. The same physics also applies to other transition metal dichalcogenide monolayers in the 2H phase.

A non-equilibrium charge carrier population imbalance between valleys is the key to creating

valleytronic devices [2, 35–43]. The principal mechanism invoked here is circularly polarized optical excitation [37, 38]. In this approach, the two valleys absorb left- and right-handed photons differently, a phenomenon referred to as circular dichroism. An essential condition for valley-selective circular dichroism in a honeycomb lattice is the absence of a center of inversion in the crystal structure. In the case of graphene, it was suggested that by interacting graphene with a substrate such that the center of inversion can be obliterated, whereupon a gap opens up in each valley [44, 45]. This strategy, however, is quite challenging experimentally. This is because i) the perturbation to graphene's electronic structure is hindered by the large van der Waals separations between graphene and the substrate [45], ii) the perturbation potential has to be commensurate with the graphene lattice.

Quite remarkably in the context of current discussion, the natural stable structure of free-standing monolayer transition metal dichalcogenides in the 2H form is a honeycomb lattice with inequivalent bipartite coloring, breaking the inversion symmetry (the crystal structure of a typical transition metal dichalcogenide, MoS_2, is shown in Fig. 1.1 b). Also, because monolayer transition metal dichalcogenides are direct bandgap semiconductors with large oscillator strength [28], charge carriers could be generated by optical excitation.

Relevant to the creation of a non-equilibrium charge carrier imbalance between the two valleys by circularly polarized light, the key quantity to assess is the $\boldsymbol{k}$-resolved degree of optical circular polarization, $\eta(\boldsymbol{k})$, between the top of the valence band and the bottom of the conduction band [38].

$$\eta_{cv}(\boldsymbol{k}) = \frac{|\mathcal{P}_{cv,+}(\boldsymbol{k})|^2 - |\mathcal{P}_{cv,-}(\boldsymbol{k})|^2}{|\mathcal{P}_{cv,+}(\boldsymbol{k})|^2 + |\mathcal{P}_{cv,-}(\boldsymbol{k})|^2}. \tag{2.1}$$

This quantity is the difference between the absorption (proportional to $|\mathcal{P}|^2$) of left- and right-handed lights ($\pm$), normalized by total absorption, at each $\boldsymbol{k}$-point and evaluated between the top of the valence bands (v) and the bottom of conduction bands (c). The density functional theory calculated band structure of monolayer MoS_2 is shown in Fig. 2.1 a. Note that the dependence on the transition energy, $\hbar\omega_{cv}(\boldsymbol{k}) = \epsilon_c(\boldsymbol{k}) - \epsilon_v(\boldsymbol{k})$, is implicit through $\boldsymbol{k}$. Here, the transition matrix element of circular polarization is $\mathcal{P}_{cv,\pm}(\boldsymbol{k}) = \frac{1}{\sqrt{2}}[P_{cv,x}(\boldsymbol{k}) \pm iP_{cv,y}(\boldsymbol{k})]$. Since in the K and K' valleys of monolayer MoS_2, the total absorption $|\mathcal{P}_{cv,+}(\boldsymbol{k})|^2 + |\mathcal{P}_{cv,-}(\boldsymbol{k})|^2$ is almost constant with $\boldsymbol{k}$, the degree of circular polarization $\eta_{cv}(\boldsymbol{k})$ directly reflects the contrast in the oscillator strength between the absorption of left- and right-handed lights. The interband matrix elements, $\mathcal{P}_{cv}(\boldsymbol{k}) = \langle\psi_{c\boldsymbol{k}}|\hat{\boldsymbol{p}}|\psi_{v\boldsymbol{k}}\rangle$, are evaluated using linear response theory, within the local density approximation of density functional theory [46], as implemented in VASP (the evaluated matrix element, rigorously speaking, is $\langle\psi_{c\boldsymbol{k}}|\hat{\boldsymbol{v}}|\psi_{v\boldsymbol{k}}\rangle$, the velocity matrix element. This is because the contribution from the non-local part of the pseudopotential has to be accounted. Relativistic effect, i.e., spin-orbit coupling, was not taken into account in this chapter) [47]. Briefly, a planewave basis set is employed at a cut-off energy 600 eV,

and a total of 80 bands are included to ensure convergence of all computed quantities. A very dense $\boldsymbol{k}$-point mesh (15129 grid points) over the irreducible hexagonal Brillouin zone is sampled in our calculations. The excitonic effects are not included in this chapter.

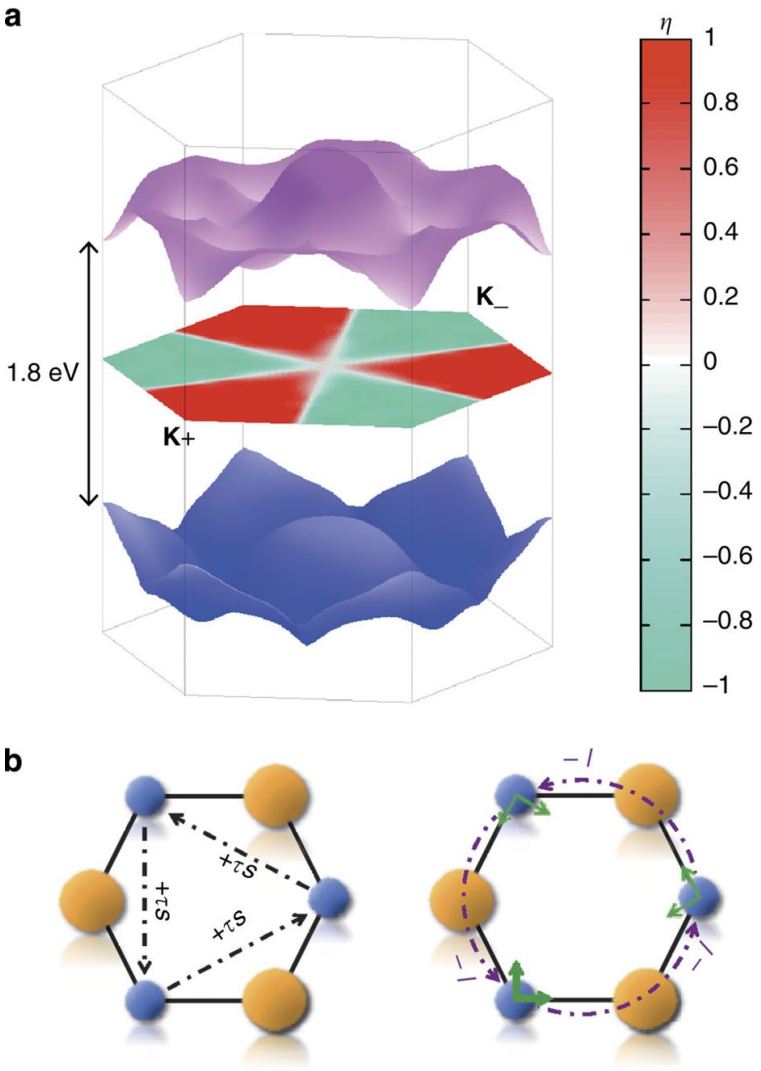

Figure 2.1: Valley-selective circular dichroism of monolayer MoS_2. (a) Top valence band (blue) and bottom conduction band (pink). The center hexagon is the Brillouin zone color-coded by the degree of circular polarization, $\eta(\boldsymbol{k})$, as defined in the text. The vector connecting K (K_+) and K' (K_-) is perpendicular to Mo-S bond in the crystal structure in Fig. 1.1 b. (b) Schematic of phase winding on the MoS_2 lattice that gives rise to the chiral optical selectivity. Left panel: the contribution to phase winding from the Bloch lattice phase, where $\tau = \pm 1$ is the valley index, and $s = 1, 2$ corresponding to the S and Mo sites (isospin index). Right panel: the phase winding under a three-fold rotation. The green axes indicate the rotation of local atomic coordinates that leads to the azimuth dissynchronization.

As shown in Fig. 2.1 a, chiral absorption selectivity is indeed exact at K (K_+) and K' (K_-)

with $\eta = \pm 1$. The contrast in the chiral absorptivities between the valleys owes its origin to the symmetry of both lattice and local atomic orbitals, which is quite different from the gapped graphene case [38]. A band state relevant to the optical excitation mainly originates from local atomic states w, having a characteristic orbital magnetic quantum numbers, l,

$$w_l(\boldsymbol{r}) = e^{il\varphi} f(\theta, r), \tag{2.2}$$

where (r, θ, φ) are the standard spherical coordinates taking the z-direction perpendicular to the plane of MoS_2. In the case monolayer MoS_2, the states at the top of the valence bands involve only $d_{x^2-y^2}$ and d_{xy} on Mo, and p_x and p_y states on S. At K, the d-states on Mo hybridize as $\frac{1}{\sqrt{2}}(d_{x^2-y^2} + id_{xy})$ $(l = +2)$ to interact with $\frac{1}{\sqrt{2}}(p_x + ip_y)$ $(l = +1)$ on S. (Here, the hybridization between the $l = +2$ on Mo and $l = -1$ on S is forbidden, since the hybridized wavefunction does not have the symmetry of the Hamiltonian at K.) At K', the d-states on Mo hybridize as $\frac{1}{\sqrt{2}}(d_{x^2-y^2} - id_{xy})$ $(l = -2)$ to interact with $\frac{1}{\sqrt{2}}(p_x - ip_y)$ $(l = -1)$ on S. At the bottom of the conduction band, mainly d_{z^2} state on Mo $(l = 0)$ is involved with a minor contribution from the orbitals of S. These atomic orbitals form such linear combinations in accordance with the D_{3h} point group symmetry and the lattice translational symmetry.

The optical selection rule is rooted in the phase winding of the Bloch states under rotational symmetry, 3-fold rotation ($\hat{C}_3$) in this case. Given the symmetry-adapted linear combinations of the atomic orbitals, the azimuthal phase associated with the 3-fold rotation at K and K' is readily calculable,

$$\hat{C}_3|v(K))\rangle = |v(K)\rangle, \tag{2.3}$$

$$\hat{C}_3|v(K'))\rangle = |v(K')\rangle, \tag{2.4}$$

and

$$\hat{C}_3|c(K)\rangle = e^{-i2\pi/3}|c(K)\rangle, \tag{2.5}$$

$$\hat{C}_3|c(K')\rangle = e^{+i2\pi/3}|c(K')\rangle, \tag{2.6}$$

where v and c correspond to the valence and conduction band extrema, respectively. Notice, however, the phase winding associated with the rotation has two distinct contributions, as schematically illustrated in Fig. 2.1 b. The first comes from the Bloch phase shift in stepping

from one lattice site to a next, as in the case of gapped graphene [37]. The second phase factor arises as a consequence of dissynchronization of the azimuthal phase (associated with the magnetic quantum number, l) concomitant with rotation of local atomic coordinates (green axes in Fig. 2.1 b). Here, although the first contribution does not directly affect the angular momentum conservation in the optical transition and the selection rules (since the wavefunctions mainly arise from orbitals of Mo), this term is related to many other chiral properties of the valleys.

Now the chiral optical selectivity of the valleys can be deduced. The bottom of the conduction bands at the valleys, dominated by the $l = 0$ d-states on Mo, bears an overall azimuthal quantum number $m_\pm = \pm 1$, at K and K', respectively. At the top of the valence bands, $m_\pm = 0$. Then for an optical transition at K and K', the angular momentum selection rule indicates that $\delta m_\pm = \pm 1$, corresponding to the absorption of left- and right-handed photons. Therefore, our linear response results based on density functional theory concerning the close neighborhood of the valleys, which is most important to the proposed optical valley polarization, are in fact ensured by the symmetry of the material.

There is an important distinction, compared to gapped graphene, in the microscopic origin of chiral optical selection rule; that is, the selectivity arises directly from the local relative azimuthal phase of the atomic orbitals, in contrast to the sublattice-dependent Bloch phase winding in the case of gapped graphene [37]. The bonding of the electronic states in MoS_2 across the gap is also considerably more complex, exhibiting richer possibilities of variation owing to the symmetry of local atomic states. Remarkably, the selectivity is nearly perfect over the entire valleys, and only changes sign rapidly across valley boundaries (see Fig. 2.1 a). This is to say, the entire valley K absorbs almost purely left-handed photons, whereas the entire valley K' purely right-handed. The perfect intrinsic valley-contrasting circular dichroism is very much conducive to optical polarization of the valleys. When a left (right) -handed light is shone over the sample, a non-equilibrium state will be created where the charge carrier population resides mostly in K (K') valley (valley polarization).

2.2 Valley Hall Effect in Transition Metal Dichalcogenide Monolayers

Now that we have established the valley-selective circular dichroism in monolayer MoS_2 with ensuing non-equilibrium valley polarization, it is also interesting to inspect the Berry curvature, which, if present, has crucial influence on the electronic transport properties. Berry curvature enters into the semiclassical wavepacket dynamics via an anomalous velocity perpendicular to the applied electric field ($\sim \boldsymbol{E} \times \boldsymbol{\Omega}_n(\boldsymbol{k})$), in addition to the usual group velocity of a Bloch band state [48, 49]. Although Berry curvature is not exactly a ground-state property, it can be evaluated quite accurately for the Kohn-Sham one-particle states [50, 51]. The presence of non-vanishing Berry curvature is possible in the non-centrosymmetric honeycomb

lattice [37]. In Fig. 2.2, we plot the Berry curvature $\Omega_{n,z}(\boldsymbol{k}) = -2\mathrm{Im}\langle\partial u_{n\boldsymbol{k}}/\partial k_x|\partial u_{n\boldsymbol{k}}/\partial k_y\rangle$ along the $K'(K_-) - \Gamma - K(K_+)$ path. Because the system has time-reversal symmetry and not inversion symmetry, $\Omega_{n,z}(\boldsymbol{k})$ is an odd function in $\boldsymbol{k}$ with generally non-zero values, as expected. The charge carriers' anomalous velocities acquire opposite signs in the two valleys, exactly cancelling each other's contribution to the transverse current. At equilibrium, free-standing monolayer MoS_2 will not exhibit valley Hall effect, as expected. Comparing the Berry curvatures of the conduction and valence bands in Fig. 2.2, we observe that, at K and K' valleys, the Berry curvatures do not have the particle-hole symmetry. This is a clear indication that the physics of MoS_2 cannot be fully captured by a minimalistic two-band model, as is distinct from the case of gapped Dirac Fermion [37].

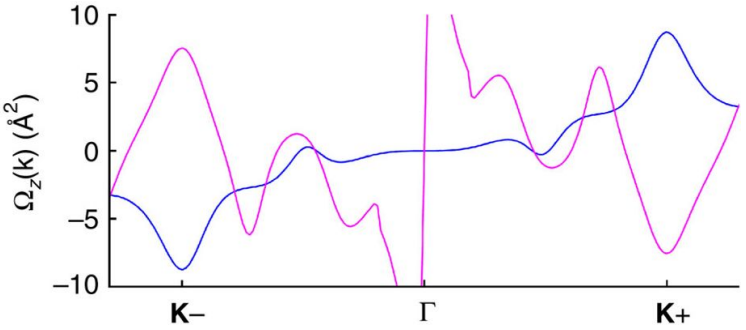

Figure 2.2: The blue curve corresponds to the top of valence bands. The red curve corresponds to the bottom of conduction bands. The Berry curvatures of the states along the $K'(K_-) - \Gamma - K(K_+)$ path of the Brillouin zone are plotted. The value of Berry curvature is large for the conduction band at the zone centre, where bands are degenerate.

On the basis of our results [1], a few further experiments are quite compelling. When valley polarization is induced by, say, valley-selective circular dichroism, only one valley has non-vanishing charge carrier population (ideally, assuming the absence of intervalley scattering). This can then lead to the Hall effect and magnetization without an applied magnetic field. The Berry curvature across the band edges near K and K' is most relevant to photo-excited charge carriers. We see that, at the band edges, both conduction and valence bands display significant Berry curvature with opposite signs. Consequently, when electrons and holes are generated by a circularly polarized irradiation, both types of charge carriers have an intrinsic additive contribution to the Hall conductivity. The valley Hall effect has been experimentally realized, although the Hall signal may arise from extrinsic effect rather than the intrinsic effects discussed above [52].

Chapter 3

Exciton Physics in Two-Dimensional Materials

Despite intensive research on the optical and transport properties of monolayer transition metal dichalcogenide, the fundamental mechanism underlying the strong light-matter interaction in these materials was unclear before 2013. In this chapter, I present several studies on the unusual optical properties of transition metal dichalcogenide monolayers arising from the novel exciton physics, including the strongly-bound non-hydrogenic exciton series [3], the light-like exciton dispersion [4], and the magnetic brightening of the dark states [5]. These results show the distinct optical properties of two-dimensional semiconductors compared with those in zero-, one-, and three-dimensional materials.

3.1 Stongly Bound Excitons in WS_2 Monolayers

In this section, we report the identification of a series of excitonic bright and dark states in monolayer WS_2 using first-principles GW-BSE calculations and two-photon excitation spectroscopy [3]. (In this section, we only consider like-spin excitons with $S_z = 0$, i.e., the electron and the hole forming the exciton have opposite spins. The different oscillator strength between the bright and dark states studied in this section arise from the orbital part of the wavefunction only.) We find that the excitons are of Wannier type, meaning that each exciton wavefunction extends over multiple unit cells, but with extraordinarily large binding energy (~ 0.7 eV) under a quasiparticle bandgap of 2.7 eV. These strongly bound exciton states are observed to be stable even at room temperature. We reveal an exciton series that deviates substantially from hydrogen models, with a novel energy dependence on the orbital angular momentum. These findings are consistent with an earlier GW-BSE calculations of the quasiparticle and excitonic properties of monolayer MoS_2 [53, 54], as well as other experimental and theoretical studies of transition metal dichalcogenide monolayers [55–57]. The discovery of excitonic dark states and large binding energy in this section not

only sheds light on the importance of many-electron effects in this two-dimensional gapped system, but also holds potential for the device application of transition metal dichalcogenide monolayers and their heterostructures in computing, communication and bio-sensing.

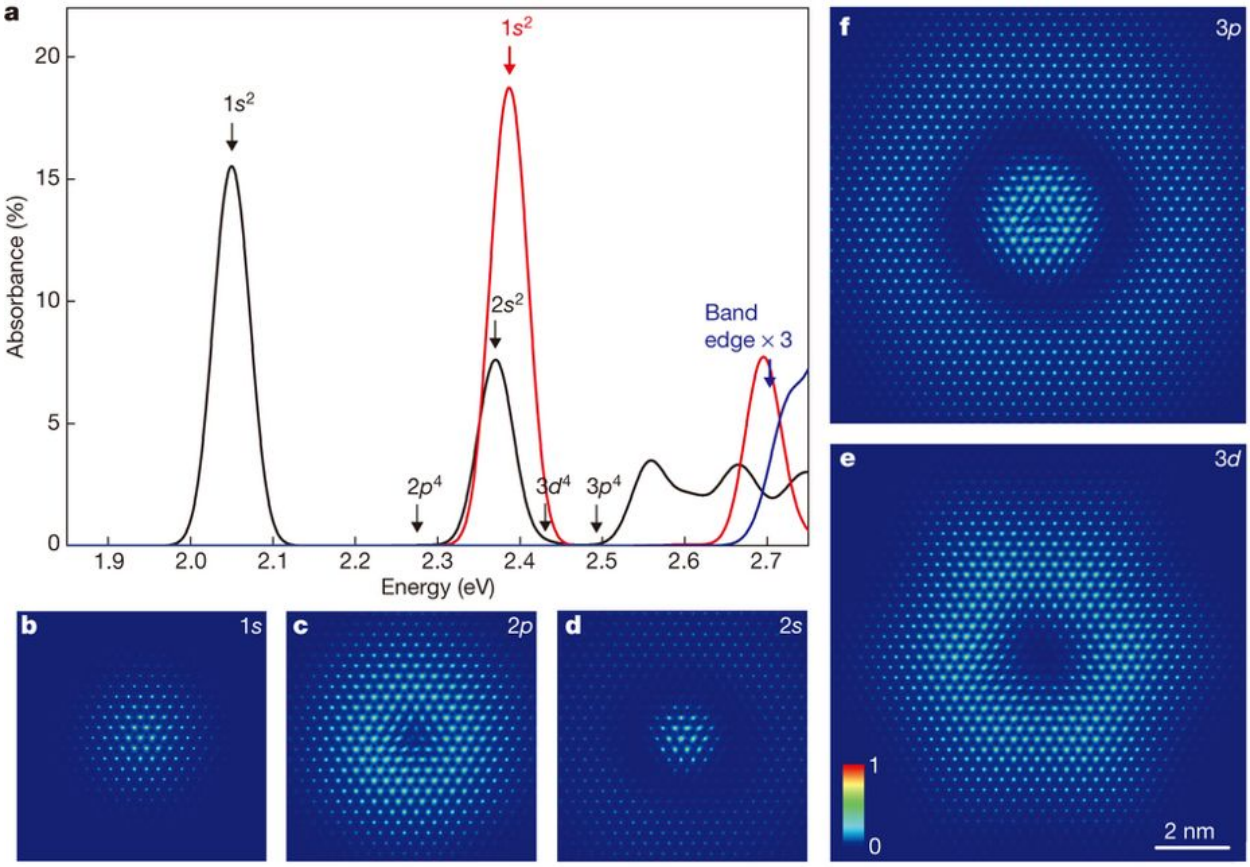

Figure 3.1: (a), The optical absorption of the A (black) and B (red) exciton series considering electron-hole interaction. The blue curve is the optical absorption spectrum, obtained without considering electron-hole interaction, where the quasiparticle bandgap is about 2.7 eV (blue arrow). The excitonic states of A and B exciton series, with electron-hole interaction included, are calculated (shown in (b)-(f), see below) and labeled (in a) by black and red arrows, respectively, up to 2.5 eV. The computed $1s$, $2p$ and $3p$ states of the A exciton are at 2.05 eV, 2.28 eV and 2.49 eV, respectively, and are in excellent agreement with the experimental measurements. Although the orbital notation of a two-dimensional hydrogen atom is adopted to label the exciton states, the excitonic series significantly deviates from a hydrogenic series, as discussed in the main text. The degeneracy labels in the superscript include both the degeneracy of valleys and orbital angular momentum. (b)-(f), The plots are modulus squared of the real-space exciton wavefunction projected onto the WS_2 plane, with the hole position fixed near a W atom at the center of the plot. These wavefunctions share similar in-plane nodal structures with the excited states in a hydrogen atom, and therefore enable the eigenstates to be labeled with a principal and an orbital quantum number. The Wannier nature of the excitons is clear, with the radii much larger than the unit cell. The color scale is the normalized wavefunction probability and applies to panels (b)-(f).

We used the first-principles GW method [20, 58] to calculate the quasiparticle band structure and the first-principles GW-BSE approach [22, 58] to calculate the excitonic states and optical spectrum of a WS_2 monolayer (Fig. 3.1 a), employing the BerkeleyGW package [58]. The principal and orbital quantum numbers of each exciton state are identified by analyzing the character of the excitons real-space wavefunction (Fig. 3.1 b-f). Specifically, the nodal characters along the radial direction are unique for each exciton state and have a one-to-one correspondence with those of the two-dimensional Rydberg series. Consistent with the selection rule of one-photon absorption for dipole-allowed materials [7], we find that the s state is one-photon active or bright, while the other (p and d) excitons are one-photon inactive or dark. Clearly, the calculated $2p$ and $3p$ states, marked at 2.28 and 2.49 eV in Fig. 3.1 a, agree well with the experimental results (Fig. 3.2), which confirms our observation of dark excitonic states in WS_2 monolayer. The calculated positions of the $1s$ state of the A exciton series (2.04 eV) and B exciton series (2.4 eV) also agree well with the experimental spectrum. As is evident from the real-space wavefunctions in Fig. 3.1 b-f, the excitons in monolayer WS_2 have a Wannier nature, with their in-plane radii much larger than the unit cell dimension. Owing to the multi-component orbital nature of the wavefunctions in the valleys, the linear absorption selection rule is not exact. The exciton p states acquire a small but finite oscillator strength in our calculation, with the oscillator strength 2 to 3 orders of magnitude smaller than that of the s state in the same shell.

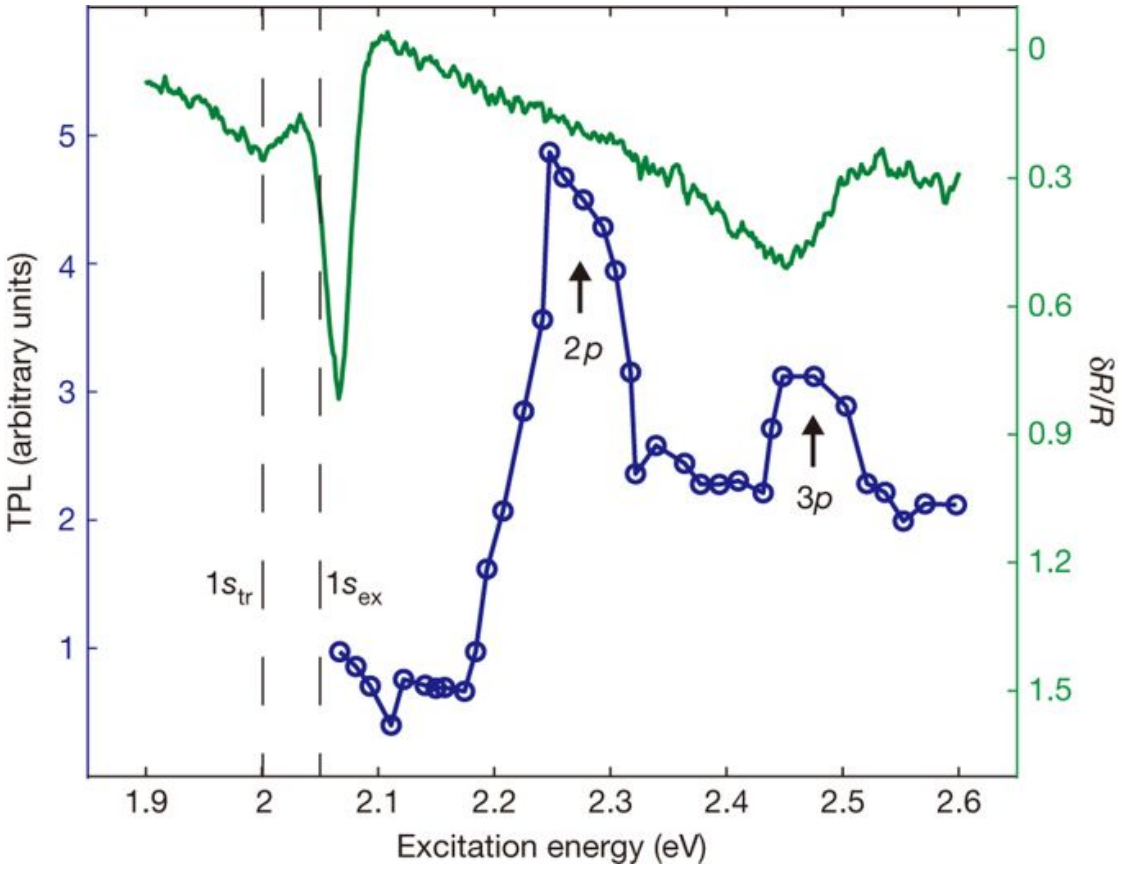

Figure 3.2: Two-photon absorption (blue) and one-photon absorption (green) spectra are measured in single-layer WS_2 at 10 K. In the two-photon absorption spectrum, $2p$ and $3p$ resonances are observed at 2.28 eV and 2.48 eV, respectively, on top of a plateau background. For comparison, the one-photon absorption spectrum, measured as the relative reflectance signal ($\delta R/R$), exhibits no corresponding features except a B exciton ($1s$) related absorption resonance at 2.45 eV. Additionally, the A exciton ($1s_{ex}$) and trion ($1s_{tr}$) absorption peaks are detected consistently with the two-photon luminescence peaks, with a 20 meV Stoke shift, and are marked at 2.04 and 2 eV, respectively, by black dashed lines. The energy difference between the A exciton 1s state emission peak and the 3p state absorption peak is 0.44 eV, which yields the lower bound for the exciton binding energy in monolayer WS_2. This binding energy is extraordinarily large for a Wannier exciton, and implies a dominating excitonic mechanism for the intense light-matter interaction in two-dimensional transition metal dichalcogenides. The total excitation scan is achieved by tuning an output beam of an optical parametric oscillator over a 600 meV span, with a scanning resolution of about 15 meV. Similar results are repeated in more than 5 flakes.

In spite of its Wannier character, we found that the exciton series in monolayer WS_2 deviates

significantly from a two-dimensional hydrogen model. Much smaller splitting between $1s$ and other excited states is observed, in accordance with other recent GW-BSE calculations [53, 54]. In addition, in a hydrogen model, orbitals with the same principal quantum number are degenerate. However, for the WS_2 excitons, our calculations show that states in the same shell but of higher orbital angular momenta are at lower energy levels, that is, $E_{3d} < E_{3p} < E_{3s}$. These two exotic energy-level behaviors are caused by a strong spatial-dependent dielectric screening: in an atomically thin semiconductor, the screening effect at more than a certain distance is weaker when the separation between the electron and hole is bigger, which is known as the anti-screening effect in one-dimensional carbon nanotubes [59] and as the dielectric confinement effect in two-dimensional quantum wells [60]. Since the wavefunction of excitonic states with higher principal or higher orbital quantum number is more extended (that is, a larger average electron-hole separation), weaker screening at larger separation leads to enhanced Coulomb attraction in the excited states and therefore a lowering of their excitation energies as compared with those of the hydrogen model [59]. Also, because of the degeneracy of the K and K' valleys in the transition metal dichalcogenides system, each s level has two degenerate states, while each p and d level has four degenerate states if the chirality of valleys were ignored (We note that such chirality could lift the degeneracy of p excitons [61, 62]). All of these features are expected to be quite general for two-dimensional excitons in transition metal dichalcogenide monolayers.

The GW quasiparticle bandgap is calculated to be ~ 2.7 eV, indicated by the blue arrow in Fig. 3.1. This value of the quasiparticle bandgap is obtained under a lattice constant of 3.13 Å, from a fully relaxed structure within the local density approximation. Comparing the quasiparticle bandgap with the 1s exciton energy found in either our experiments (Fig. 3.2) or our GW-BSE calculations, we obtain an exciton binding energy of ~ 0.7 eV. Such an exceptionally large binding energy is more than ten times that found for the excitons in bulk WS_2 [63] and other traditional bulk semiconductors such as Si and GaAs [64], and comparable to those found for excitons in carbon nanotubes [65, 66]. The large binding energy results from the combined effects of reduced dimensionality, relatively large effective masses and weak dielectric screening, which renders the excitons observable even at room temperature. The Wannier-like, strongly-bound excitons were also found in other transition metal dichalcogenide monolayers, carbon nanotubes, graphene nanoribbons, and inorganic-organic hybrid perovskites [53–55, 57, 65, 67, 68].

3.2 Exciton Dispersions in Transition Metal Dichalcogenide Monolayers

In this section, I present our study on the exciton dispersion in monolayer MoS_2 [4]. Exciton dispersion as a function of center-of-mass momentum $\boldsymbol{Q}$ is essential to the understanding of exciton dynamics. We use the first-principles GW-BSE method to calculate the dispersion of excitons in monolayer MoS_2 and find a nonanalytic light-like dispersion. This behavior arises

from an unusual $|\boldsymbol{Q}|$-term in both the intra- and intervalley-exchange of the electron-hole interaction, which concurrently gives rise to a valley quantum phase of winding number 2. The linear dispersion of excitons applies not only to monolayer transition metal dichalcogenides, but also to many other two-dimensional semiconductors, such as monolayer black phosphorus.

In previous sections, we have only considered excitons with 0 center-of-mass momentum with spin quantun number $S_z = 0$. However, an exciton is a neutral excitation of a periodic system, and should consist of a bound excited electron and hole with energy depending on its center-of-mass momentum, $\boldsymbol{Q}$, just like that of an electron (or hole). In crystals, the exciton dispersion relation (energy vs $\boldsymbol{Q}$) forms an exciton band structure. In optical absorption, the momentum of a photon is converted to that of an exciton, resulting in a small $\boldsymbol{Q}$ exciton for visible light. Recent model Hamiltonian calculations predict that the dispersion of the lowest energy optically active exciton bands in monolayer MoS_2 form a Dirac cone (as in graphene) due to the exchange interaction coupling electron-hole states in different valleys (the intervalley exchange) [69]. Another study based on a tight-binding formulation of the BSE approach hinted at also linear dispersion for the lowest energy bright excitons near $\boldsymbol{Q} = 0$, although the dispersion relation (on a 45×45 finite-$\boldsymbol{Q}$ grid) was not resolved at the length scale of the momentum of light [70]. The effects of the interplay of inter- and intravalley-exchange and local fields are not explicitly investigated in these model calculations, which also miss terms in both $\boldsymbol{Q}$ and $\boldsymbol{Q}^2$ orders.

In this work, we calculate the exciton dispersion of MoS_2, a prototypical transition metal dichalcogenide, from first-principles, using the GW-BSE method, and find a highly unusual low-energy dispersion consisting of a nonanalytic v-shaped upper band that is degenerate with a parabolic lower band at $\boldsymbol{Q} = 0$, consistent qualitatively with extrapolation of previous tight-binding results [70]. We show that the physical origin of this highly nonanalytic behavior (the $|\boldsymbol{Q}|$ dependence) comes from $|\boldsymbol{Q}|$-dependent terms in both the intravalley and intervalley exchange interaction, which arise from the unique electronic structure and the quasi-two-dimensional nature of the Coulomb interaction in atomically thin transition metal dichalcogenides. Local-field effects introduce additional interaction terms and are responsible for the splitting of optically bright and dark excitons. Moreover, the theory gives a valley quantum phase of winding number 2 (or chirality 2), which we show should manifest in optical experiments as a phase difference between the longitudinal and transverse response. A similar winding number is found in Ref. [69], although in this model Hamiltonian study, intravalley exchange is neglected resulting in a Dirac cone dispersion with both positive and negative energies. After including the intravalley exchange interactions, this model yields qualitatively similar results compared with our first-principles calculations [4, 71].

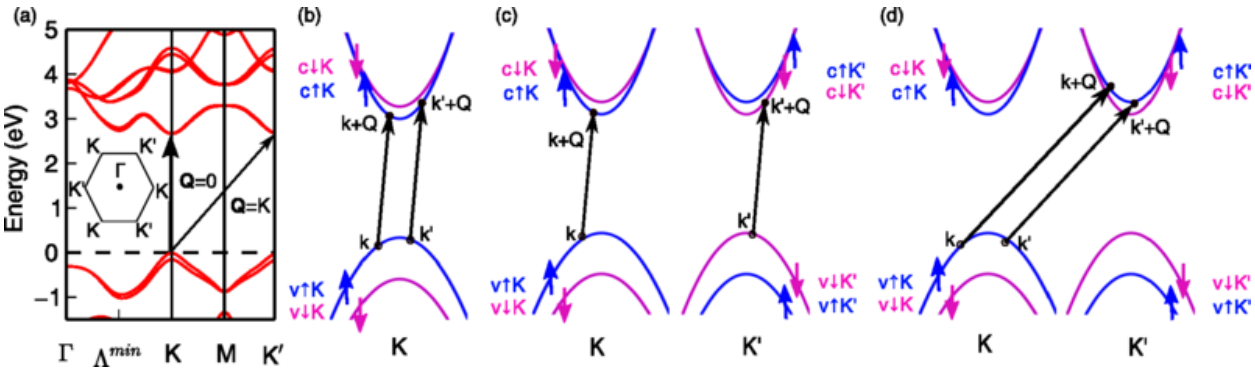

Figure 3.3: (a), Quasiparticle band structure of monolayer MoS_2. Lowest energy transitions corresponding to electron-hole excitations with momentum transfers of $\boldsymbol{Q} = 0$ and $\boldsymbol{Q} = \boldsymbol{K}$ are shown with the labeled arrows. (b-c), Schematics of interactions between two electron-hole pairs with momentum near $\boldsymbol{Q} = 0$, corresponding to BSE matrix elements $\langle cv, \boldsymbol{kQ}|\hat{K}^{eh}|c'v', \boldsymbol{k'Q}\rangle$ for (b), two like-spin transitions within one valley and (c), two like-spin transitions from different valleys. (d), Schematic of two electron-hole pairs with momentum near $\boldsymbol{Q} = \boldsymbol{K}$ giving rise to BSE matrix elements for like-spin transitions.

The quasiparticle band structure of monolayer MoS_2 calculated within the GW approximation is shown in Fig. 3.3. The direct gap of 2.67 eV is at the K and K' points. Spin-orbit coupling splits the valence band edge by 147 meV and the conduction band edge by 3 meV. Over an extended range in the K and K' valleys, S_z, the spin of the electron along the direction perpendicular to the layer is a good quantum number [72]. Thus, the concept of singlet and triplet exciton states is no longer well defined. Instead, the electron-hole Hamiltonian or BSE matrix can be decoupled into transitions between bands of like spin (Figs. 3.3) that are optically allowed and transitions between bands of unlike spin that are optically forbidden. We calculate the exciton dispersion of both the like-spin transition states and the unlike-spin transition states within the BSE formalism following Ref. [22]. The resulting exciton dispersion near $\boldsymbol{Q} = 0$ and $\boldsymbol{Q} = \boldsymbol{K}$ is shown in Fig. 3.4. Fig. 3.4 only presents exciton states involving predominantly transitions from the topmost valence band in each valley, which is the so-called A series in the literature. "B" states involving transitions from the second highest valence band are similar and shown in the Supplemental Material of [4].

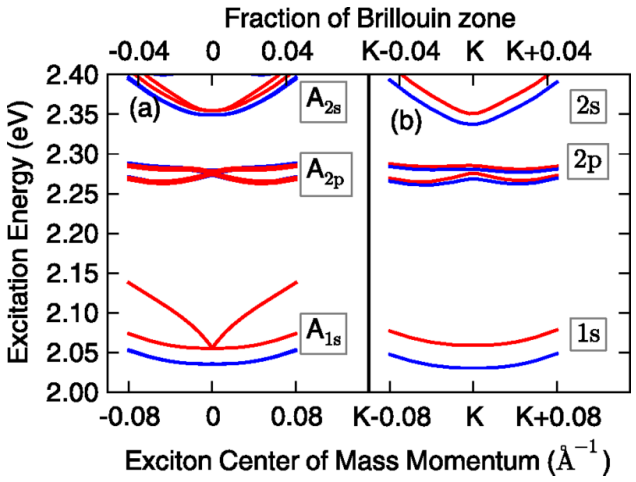

Figure 3.4: Exciton dispersion of monolayer MoS_2 near (a), $\boldsymbol{Q} = 0$ and (b), $\boldsymbol{Q} = \boldsymbol{K}$ along the $K - \Gamma - K'$ direction. Red (blue) lines indicate states arising from like-spin (unlike-spin) transitions. The label A refers to states involving transitions from the highest valence band at K and K'. "B" states involving transitions from the second highest valence band are similar and shown in the Supplemental Material of [4].

In Fig. 3.4, near $\boldsymbol{Q} = 0$, the lowest energy exciton complex shown is the $1s$-like states of the A series excitons, which has a binding energy of 0.63 eV for the like-spin transition states and 0.65 eV for the unlike-spin transition states. At $\boldsymbol{Q} = 0$, the twofold degeneracy of the exciton states due to K and K' valley degeneracy is protected by time-reversal symmetry. Away from $\boldsymbol{Q} = 0$, for optically active like-spin transition states, the degenerate bands split as $|\boldsymbol{Q}|$ increases. Consistent with previous model calculations [69–71, 73], this splitting of the like-spin transition states is due to intervalley exchange. The exciton bands for unlike-spin states, which have zero exchange interaction, remain doubly degenerate (the blue lines in Fig. 3.4). However, contrary to previous model predictions [69], our first-principles results do not find a Dirac cone near $\boldsymbol{Q} = 0$ in the dispersion of the like-spin transition 1s bands. In fact, we find a "v-shaped" nonanalytic upper band with a velocity of 3×10^5 m/s or 0.001 c and a parabolic lower band, with both bands increasing monotonically with $|\boldsymbol{Q}|$ down to the smallest sampled $|\boldsymbol{Q}|$ of 4×10^{-3}Å^{-1}, which corresponds to 0.3% of the distance from Γ to K in the Brillouin zone.

We also calculate the dispersion of the intervalley excitons (Fig. 3.4 b)-i.e., an exciton with the electron and hole in different valleys (with $\boldsymbol{Q} = \boldsymbol{K}$)-and find that the unlike-spin transition state is slightly lower in energy than the similar exciton at $\boldsymbol{Q} = 0$ as a consequence of the spin-orbit splitting of the conduction bands and the difference in screened Coulomb interactions.

We now provide the physical origin of the nonanalytic behavior of the dispersion seen in

Fig. 3.4. The exciton dispersion is obtained from first-principles by solving the BSE for electron-hole pair excitations with finite center-of-mass momentum $\boldsymbol{Q}$

$$(E_{c,\boldsymbol{k+Q}} - E_{v,\boldsymbol{k}})A^S_{vc,\boldsymbol{kQ}} + \sum_{v'c',\boldsymbol{k'}} \langle vc,\boldsymbol{kQ}|K^{eh}|v'c',\boldsymbol{k'Q}\rangle A^S_{v'c'\boldsymbol{k'Q}} = \Omega^S_{\boldsymbol{Q}} A^S_{vc,\boldsymbol{kQ}} \tag{3.1}$$

Here, S indexes the exciton states, $A^S_{vc,\boldsymbol{kQ}}$ is the amplitude of the free electron-hole pair consisting of an electron in $|c,\boldsymbol{k}+\boldsymbol{Q}\rangle$ and one missing from $|v,\boldsymbol{k}\rangle$, $\Omega^S_{\boldsymbol{Q}}$ is the exciton excitation energy, $E_{c,\boldsymbol{k+Q}}$ and $E_{v,\boldsymbol{k}}$ are the quasiparticle energies, and K^{eh} is the electron-hole interaction kernel. The kernel consists of a direct term and an exchange term [22] $\langle vc,\boldsymbol{kQ}|K^{eh}|v'c',\boldsymbol{k'Q}\rangle = \langle vc,\boldsymbol{kQ}|K^d + K^x|v'c',\boldsymbol{k'Q}\rangle$. The exchange term is,

$$\langle vc,\boldsymbol{kQ}|K^x|v'c',\boldsymbol{k'Q}\rangle = \sum_{\boldsymbol{G}} M_{cv}(\boldsymbol{k},\boldsymbol{Q},\boldsymbol{G}) v(\boldsymbol{Q}+\boldsymbol{G}) M^*_{c'v'}(\boldsymbol{k'},\boldsymbol{Q},\boldsymbol{G}) \tag{3.2}$$

where $\boldsymbol{G}$ are reciprocal lattice vectors, v is the bare Coulomb interaction, and M is defined as $M_{nn'}(\boldsymbol{k},\boldsymbol{Q},\boldsymbol{G}) = \langle n\boldsymbol{k}+\boldsymbol{Q}|e^{i(\boldsymbol{Q}+\boldsymbol{G})\cdot\boldsymbol{r}}|n'\boldsymbol{k}\rangle$. The exchange term is only non-zero for like-spin transitions (i.e., excitons with total spin along z equal to zero). The direct term is

$$\langle vc,\boldsymbol{kQ}|K^d|v'c',\boldsymbol{k'Q}\rangle = -\sum_{\boldsymbol{GG'}} M^*_{cc'}(\boldsymbol{k}+\boldsymbol{Q},\boldsymbol{q},\boldsymbol{G}) W_{\boldsymbol{GG'}}(\boldsymbol{q}) M_{vv'}(\boldsymbol{k},\boldsymbol{q},\boldsymbol{G}) \tag{3.3}$$

where $\boldsymbol{q} = \boldsymbol{k} - \boldsymbol{k'}$ and W is the screened Coulomb interaction.

The solutions of the BSE matrix are exciton states $|S_{\boldsymbol{Q}}\rangle = \sum_{vc,\boldsymbol{k}} A^S_{vc,\boldsymbol{kQ}}|vc,\boldsymbol{kQ}\rangle$. In the subspace spanned by the two lowest energy states, at exactly $\boldsymbol{Q} = 0$, the exchange matrix elements are also diagonal. At $\boldsymbol{Q} = 0$, the exchange term is the diagonal constant

$$\begin{aligned} C &\equiv \langle S_{\boldsymbol{0}}|K^x|S'_{\boldsymbol{0}}\rangle \\ &= \delta_{SS'} 2\pi e^2 \sum_{\boldsymbol{G}\neq 0} \sum_{vc\boldsymbol{k}v'c'\boldsymbol{k'}} A^{S*}_{vc,\boldsymbol{k0}} A^{S'}_{v'c',\boldsymbol{k'0}} \times \frac{\langle u_{c,\boldsymbol{k}}|e^{i\boldsymbol{G}\cdot\boldsymbol{r}}|u_{v,\boldsymbol{k}}\rangle \langle u_{c',\boldsymbol{k'}}|e^{i\boldsymbol{G}\cdot\boldsymbol{r}}|u_{v',\boldsymbol{k'}}\rangle^*}{|\boldsymbol{G}|}, \end{aligned} \tag{3.4}$$

where for small $\boldsymbol{Q}$'s in two dimension, $v(\boldsymbol{Q}+\boldsymbol{G}) = 2\pi e^2/|\boldsymbol{Q}+\boldsymbol{G}| \approx (2\pi e^2/|\boldsymbol{G}|)$. This constant term is 20 meV in our first-principles calculation. It is purely a local-field effect and is responsible for the splitting between the like-spin (bright) and unlike-spin (dark) states at $\boldsymbol{Q} = 0$. We note that this constant C takes a different value in other transition metal dichalcognide monolayers. For example, in monolayer WSe_2, C is smaller than 10 meV

[5]. This difference could arise from the different binding energies and different electron-hole overlaps.

We now derive an effective Hamiltonian (H^{BSE}) to describe the main physics for the $1s$ complex in a basis of "excitonic" functions from the individual valleys in the tight-binding limit, given in Eq. 3.5 below. At $\boldsymbol{Q} = 0$, both the like- and unlike-spin excitonic levels are doubly degenerate, with the amplitude $A^S_{vc,\boldsymbol{k0}}$ of one state ($|S^K_{\boldsymbol{0}}\rangle$) confined to the K valley and that of the other ($|S^{K'}_{\boldsymbol{0}}\rangle$) confined to the K' valley. Near $\boldsymbol{Q} = 0$, it is sufficient to use the following basis functions (which are of the Bloch form of excitons from a specific valley in the tight-binding limit) to expand the true exciton state $|S_{\boldsymbol{Q}}\rangle$:

$$|S^K_{\boldsymbol{Q}}\rangle \approx |e^{i\boldsymbol{Q}\cdot\boldsymbol{R}} S^K_{\boldsymbol{0}}\rangle \equiv \begin{pmatrix} 1 \\ 0 \end{pmatrix}_{\boldsymbol{Q}}, \; |S^{K'}_{\boldsymbol{Q}}\rangle \approx |e^{i\boldsymbol{Q}\cdot\boldsymbol{R}} S^{K'}_{\boldsymbol{0}}\rangle \equiv \begin{pmatrix} 0 \\ 1 \end{pmatrix}_{\boldsymbol{Q}}, \tag{3.5}$$

where $\boldsymbol{R} = [(\boldsymbol{r}_e + \boldsymbol{r}_h)/2]$, $\begin{pmatrix} 1 \\ 0 \end{pmatrix}_{\boldsymbol{Q}}$ and $\begin{pmatrix} 0 \\ 1 \end{pmatrix}_{\boldsymbol{Q}}$ are pseudospinors denoting, respectively, basis functions on K and K' valleys, and $|e^{i\boldsymbol{Q}\cdot\boldsymbol{R}} S^K_{\boldsymbol{0}}\rangle = \sum_{vc,\boldsymbol{k}} A^S_{vc,\boldsymbol{k0}} |vc, \boldsymbol{kQ}\rangle$.

In this basis, H^{BSE} is a 2×2 matrix and the intravalley exchange term (matrix element between basis functions in the same valley) is

$$\langle S^K_{\boldsymbol{Q}} | K^x | S^K_{\boldsymbol{Q}} \rangle = \sum_{vc\boldsymbol{k}v'c'\boldsymbol{k'}} A^{S^K *}_{vc,\boldsymbol{k0}} A^{S^K}_{v'c',\boldsymbol{k'0}} \langle vc, \boldsymbol{kQ} | K^x | v'c', \boldsymbol{k'Q} \rangle. \tag{3.6}$$

Using a $\boldsymbol{Q}\cdot\boldsymbol{p}$ expansion of the quasiparticle states in the M matrix elements (Eq. 3.2) to second order in $\boldsymbol{Q}\cdot\boldsymbol{p}$, the intravalley exchange term (Eq. 3.6) becomes

$$\begin{aligned} \langle S^K_{\boldsymbol{Q}} | K^x | S^K_{\boldsymbol{Q}} \rangle &= \langle S^{K'}_{\boldsymbol{Q}} | K^x | S^{K'}_{\boldsymbol{Q}} \rangle \\ &= \sum_{vc\boldsymbol{k}v'c'\boldsymbol{k'}} A^{S^K *}_{vc,\boldsymbol{k0}} A^{S^K}_{v'c',\boldsymbol{k'0}} (\boldsymbol{Q}\cdot a(\langle u_{v,\boldsymbol{k}} | \boldsymbol{p} | u_{c,\boldsymbol{k}} \rangle)^* \boldsymbol{Q}\cdot a' \langle u_{v',\boldsymbol{k'}} | \boldsymbol{p} | u_{c',\boldsymbol{k'}} \rangle v(\boldsymbol{Q}) \\ &+ \sum_{\boldsymbol{G}\neq 0} v(\boldsymbol{Q}+\boldsymbol{G}) \{ c + O(\boldsymbol{Q}\cdot\boldsymbol{p}) + O[(\boldsymbol{Q}\cdot\boldsymbol{p})^2] \}) \end{aligned} \tag{3.7}$$

Here, we have separated contributions from the $\boldsymbol{G} = 0$ and $\boldsymbol{G} \neq 0$ Fourier components. We note that a, a', and c are factors that depend on the quasiparticle states but are independent of $\boldsymbol{Q}$. In Eq. 3.7, the $\boldsymbol{G} = 0$-term has a nonanalytic dependence on $|\boldsymbol{Q}|$

$$|\boldsymbol{Q}\cdot\sum_{vc,\boldsymbol{k}} aA^{S^K}_{vc,\boldsymbol{k0}}\langle u_{v,\boldsymbol{k}}|\boldsymbol{p}|u_{c,\boldsymbol{k}}\rangle|^2 v(\boldsymbol{Q}) \propto A|\boldsymbol{Q}| \tag{3.8}$$

Here, A is a proportionality constant, and we have made use of the fact that for small $\boldsymbol{Q}$ in two dimensions, $v(\boldsymbol{Q}) \approx (2\pi e^2/|\boldsymbol{Q}|)$, and the fact that $\langle 0|\boldsymbol{p}|S^K_{\boldsymbol{0}}\rangle \propto \hat{x} + i\hat{y}$ due to the C_3 symmetry [1], which eliminates the dependence on the orientation of $\boldsymbol{Q}$. Up to order Q^2, the intravalley exchange (Eq. 3.6) has the form

$$\langle S^K_{\boldsymbol{Q}}|K^x|S^K_{\boldsymbol{Q}}\rangle = \langle S^{K'}_{\boldsymbol{Q}}|K^x|S^{K'}_{\boldsymbol{Q}}\rangle = C + A|\boldsymbol{Q}| + \beta Q^2 \tag{3.9}$$

C is the splitting of bright and dark states given in Eq. 3.4, and β is a proportionality constant that is a real number, which arises from the local fields. Likewise, the intervalley exchange may be shown to be

$$\langle S^K_{\boldsymbol{Q}}|K^x|S^{K'}_{\boldsymbol{Q}}\rangle = \langle S^{K'}_{\boldsymbol{Q}}|K^x|S^K_{\boldsymbol{Q}}\rangle^* = A|\boldsymbol{Q}|e^{-i2\theta} + \beta' Q^2 \tag{3.10}$$

where θ is the angle of $\boldsymbol{Q}$ defined with respect to the x axis and β' is a complex number.

After performing a similar analysis of the direct term, we find an effective Hamiltonian

$$\begin{aligned} H^{BSE}(\boldsymbol{Q}) = \Omega_{\boldsymbol{0}}1 + A[1 + \cos(2\theta)\sigma_x + \sin(2\theta)\sigma_y]|\boldsymbol{Q}| \\ + \{(\frac{\hbar^2}{2M} + \alpha + \beta)1 + |\beta'|[\cos(2\theta)\sigma_x + \sin(2\theta)\sigma_y]\}Q^2 \end{aligned} \tag{3.11}$$

where $\Omega_{\boldsymbol{0}}$ is the excitation energy of the exciton with $\boldsymbol{Q} = 0$, 1 is the identity matrix, $M = m_e + m_h$ is the quasiparticle band mass of the free electron-hole pair at K or K', α is a constant from the order of the Q^2 contribution from the direct term, β and β' are constants from the order of the Q^2 contribution from the intravalley and intervalley exchange, respectively, and σ_x and σ_y are the Pauli matrices. An effective Hamiltonian may be obtained for the other exciton complexes through similar analyses.

Diagonalizing the effective Hamiltonian (Eq. 3.11) gives us two solutions: one with a parabolic dispersion

$$\Omega_-(\boldsymbol{Q}) = \Omega_{\boldsymbol{0}} + (\frac{\hbar^2}{2M} + \alpha + \beta - |\beta'|)Q^2 \tag{3.12}$$

and the other with a nonanalytic dispersion

$$\Omega_+(\boldsymbol{Q}) = \Omega_{\mathbf{0}} + 2A|\boldsymbol{Q}| + (\frac{\hbar^2}{2M} + \alpha + \beta + |\beta'|)Q^2 \tag{3.13}$$

Hence, it is the combination of intervalley and intravalley exchange that results in a lower band with a parabolic dispersion (Eq. 3.12) and an upper band with a nonanalytic dependence on $|\boldsymbol{Q}|$ (Eq. 3.13), as seen in our first-principles calculation (Fig. 3.5 a). We emphasize that this $|\boldsymbol{Q}|$ dependence at small $\boldsymbol{Q}$ is a consequence of the two-dimensional Coulomb interaction and the opposite angular polarization of the electronic states in the K and K' valleys, which removes the dependence on the direction of $\boldsymbol{Q}$.

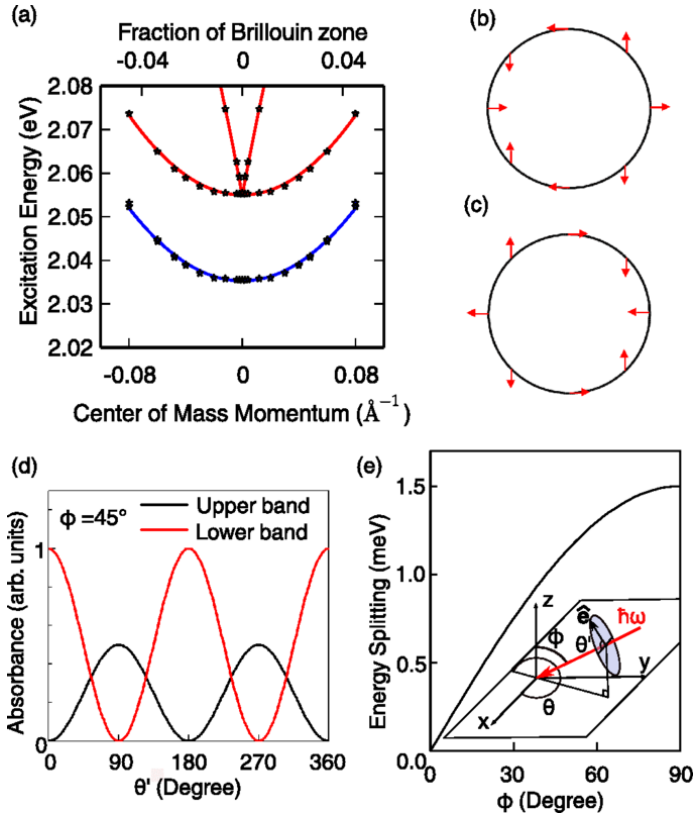

Figure 3.5: (a) Closeup of dispersion of A_{1s} near $\boldsymbol{Q} = 0$. first-principles results are stars. Fit to effective Hamiltonian (Eq. 3.12) are solid lines. Red (blue) lines indicate states arising from like-spin (unlike-spin) transitions. (b) Valley pseudospin texture of the (upper) nonanalytic like-spin transition band around $\boldsymbol{Q} = 0$ for states of fixed energy in $\boldsymbol{Q}$ space. (c) Valley pseudospin texture of the (lower) parabolic like-spin transition band. (d) Optical absorbance of linearly polarized light at fixed incidence as the polarization vector $\hat{\boldsymbol{e}}$ is rotated over 360°. The angle of the polarization vector, θ', is defined with respect to the vector formed by the intersection of the polarization plane (blue) and the $x-y$ plane. Red (black) indicates the absorbance of states arising from the lower (upper) like-spin band. (e) Energy difference between the upper and lower like-spin bands that is probed as ϕ, the angle between the wave vector of light and the z axis is changed, for light of $\hbar\omega \approx 2eV$. The inset shows how θ, ϕ, and θ' are defined.

We fit Eq. 3.12 and Eq. 3.13 to our first-principles calculation (Fig. 3.5 a) to obtain the values of the proportionality constants, A, α, β, and β'. From the slope of the linear branch, we find $A = 0.9$ eV Å. Normally, the dominant Q^2-term comes from the quasiparticle effective mass term $\hbar^2 Q^2/2M$. M for monolayer MoS_2 is roughly 1.1 m_0. From the dispersion of the unlike-spin states in which exchange interaction is zero, we find that $\alpha = -0.9$ eV Å^2, and the effective mass of the unlike-spin transition (dark) ls exciton is roughly $M^* = 1.5m_0$.

The effective mass of the parabolically dispersing like-spin transition (bright) $1s$ exciton is $M^* = 1.4m_0$, indicating that $\beta - |\beta'|$, the difference between quadratic terms in the intervalley and intravalley exchange, is small, only about 0.2 eV Å^2, while the magnitude of β is about 4 eV Å^2. Our results demonstrate an enhancement of about 30% in the center-of-mass effective mass M^* of the parabolic band excitons due to the electron-hole interaction.

Since the difference between the magnitude of the quadratic terms in the intervalley and intravalley exchange, $\beta - |\beta'|$, is small, we may to good approximation neglect this difference (i.e., we take $\beta' = e^{-i2\theta}\beta$). Then, the solution for the parabolic like-spin transition exciton band simplifies to

$$\frac{1}{\sqrt{2}}(e^{-i\theta}|S^K_{\boldsymbol{Q}}\rangle - e^{i\theta}|S^{K'}_{\boldsymbol{Q}}\rangle), \tag{3.14}$$

and the solution for the nonanalytic like-spin transition exciton band simplifies to

$$\frac{1}{\sqrt{2}}(e^{-i\theta}|S^K_{\boldsymbol{Q}}\rangle + e^{i\theta}|S^{K'}_{\boldsymbol{Q}}\rangle). \tag{3.15}$$

For both states, the valley pseudospin winding number around $\boldsymbol{Q} = 0$ is 2. The pseudospin texture of these states in a circle in $\boldsymbol{Q}$ space is shown in Figs. 3.5 b,c. To study the optical response, we project the momentum and polarization of incident linearly polarized light into the layer two-dimensional plane. The momentum $\boldsymbol{Q}$ of the excited exciton is equivalent to the in-plane component of the wave vector of the light. The in-plane projection of the electric field polarization vector can be decomposed into components perpendicular (transverse) to and parallel (longitudinal) to the momentum transfer $\boldsymbol{Q}$. We define the angle of the polarization vector with respect to the transverse projection as θ'. The absorbance of the upper and lower bands with respect to θ' has a phase difference of 90°, and the intensity of each band peaks twice as the polarization angle is rotated over 360° (Fig. 3.5 d). The different pseudospin texture results in the upper band coupling to the longitudinal component of the in-plane projection of the electric field and the lower band coupling to the transverse component of the in-plane electric field. Since the transverse projection is always in the two-dimensional plane, only the intensity of optical absorbance from the upper band changes with the angle of the incident light with respect to the z axis (ϕ) . Intensity is maximum at normal incidence ($\phi = 0$) and and minimum at grazing incidence ($\phi = 90°$). The energy difference between the upper and lower band for different $\boldsymbol{Q}$ on the dispersion curve can also be probed by changing ϕ. For photons with $\hbar\omega \approx 2$ eV, the largest energy difference is about 1.5 meV when the wave vector of the light is nearly parallel to the plane.

In summary, we have computed the exciton dispersion of MoS_2 from first principles and find an unusual dispersion with a parabolic lower band and a v-shaped upper band for the

lowest energy like-spin transition exciton complex near $\boldsymbol{Q} = 0$. This dispersion is due to the interplay of the intervalley and intravalley exchange, both of which have a $|\boldsymbol{Q}|$-dependent behavior. We have derived a simple effective Hamiltonian and analytic solutions describing this physics and predict that the splitting of the exciton bands can be measured with a linearly polarized optical beam tilted away from normal incidence. We expect any two-dimensional semiconductor with excitons with an amplitude concentrated in a small portion of the Brillouin zone to exhibit similar nonanalytic exciton dispersion near $\boldsymbol{Q} = 0$. We also show that interaction effects increase the exciton mass M^* by > 30 %. First-principles results for the intervalley excitons with $\boldsymbol{Q} = K$ and other finite-$\boldsymbol{Q}$ excitons are also obtained.

3.3 Exciton Dark States and Magneto-Optics in Transition Metal Dichalcogenide Monolayers

Because of their spin-polarized valence bands and a predicted spin splitting at the conduction band edges [72], the lowest-lying excitons in WX_2 (X = S, Se) are expected to be spin-forbidden and optically dark for out-of-plane light emissions (In MoX_2, the relative energy difference between the unlike-spin dark state and the like-spin bright states is still debated [74]). In this section, we show that an in-plane magnetic field can brighten the dark excitons in monolayer WSe_2 and permit their properties to be observed in photoluminescence [5]. Precise energy levels for both the neutral and charged dark excitons are obtained by first-principles calculations using the GW-BSE approach [20, 22, 58].

Despite the aforementioned strongly-bound non-hydrogenic (section I) and light-like dispersive excitons (section II) of transition metal dichalcogenide monolayers, the spin structure of excitons in these systems remains elusive prior to this work [5]. This information is essential for understanding the radiative properties of the materials, since allowed optical transitions in semiconductors usually occur without change in the spin of the electron. In the simple analysis at the non-interacting level, the spin structures of the excitons in the transition metal dichalcogenide monolayers directly arise from the spin splitting in the conduction bands. As a result, when the electron spins are polarized along the out-of-plane (z) direction, excitons with zero spin ($S_z = 0$, corresponding to bands with the same electron spin) are bright, while excitons with non-zero spin ($S_z = \pm 1$, corresponding to bands with opposite spin) are dark. (The spin of the hole is opposite to that of the electron for a given band state. In this section, the bright state refers to the like-spin $1s$ exciton with $S_z = 0$ and spin-allowed transitions; the dark state to the unlike-spin 1s exciton with $S_z = \pm 1$ and spin-forbidden transitions. This is different from the exciton physics discussed in section I.) In transition metal dichalcogenide monolayers, the conduction bands have been theoretically predicted to be fully spin polarized [72, 75, 76], just like the more strongly split valence bands. The spin splitting of the conduction bands is expected to be relatively modest, with a size comparable to room-temperature thermal energy and, significantly, exhibiting different signs (compared to the valence band splitting) depending on the chemical composition of the transition metal

dichalcogenide crystals. Specifically, in Mo compounds, electrons in the lowest conduction band are expected to have the same spin as those in the highest valence band (It should be noted that this conclusion is based on density functional theory calculations. In monolayer MoS_2, the conduction band splitting could be as small as 3 meV in a density functional theory calculation with local density approximation.). In contrast, the opposite spin ordering is expected in W compounds (Fig. 3.6 b), and, correspondingly, the lowest energy exciton is expected to be optically dark for in-plane polarization directions. The existence of this lower-lying dark state will quench light emission in the out-of-plane direction, particularly at low temperatures. Although distinct behavior for the thermal activation of light emission has been observed in different transition metal dichalcogenide monolayer semiconductors [74, 77, 78], the exact energy- and spin-structures of the excitonic states have not been fully determined nor understood prior to this work [5]. The latter is of critical importance for valley and spin transport and of their manipulation in these systems.

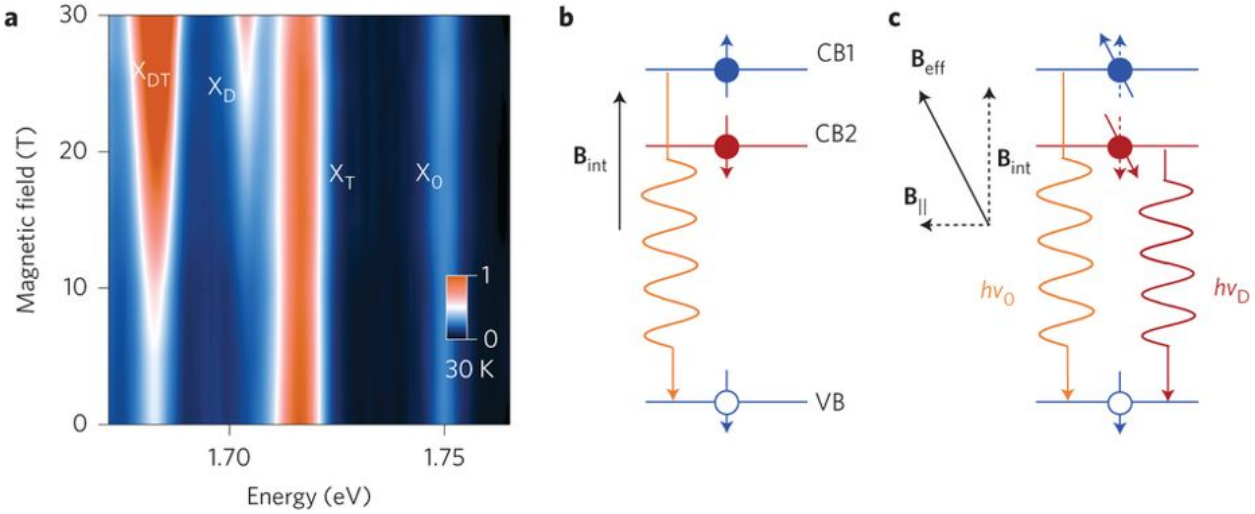

Figure 3.6: (a), False-color plot of the measured emission spectrum for monolayer WSe_2 at a temperature of 30 K as a function of the strength of the applied $\boldsymbol{B}_{\parallel}$. The displayed energy range includes emission from the neutral A exciton (X_0) and the associated trion state (X_T). Emission features from the dark exciton (X_D) and dark trion (X_{DT}) grow with increasing $\boldsymbol{B}_{\parallel}$. The scale bar represents the normalized photoluminescence intensity. (b), For monolayer WSe_2, electrons in the lower conduction band (CB2) have spin opposite that in the upper valence band (VB), rendering the lowest transition optically dark. Only transitions from the upper CB (at energy $h\nu_0$) are allowed. The spin-split CBs, CB1 and CB2, can be described as the result of an effective out-of-plane magnetic field $\boldsymbol{B}_{int}$ acting on the electron magnetic moment. The blue and red lines represent bands with electrons' spin up and down, respectively. The arrows indicate the spin of the electron/hole in an excitonic state. (c), Under an external in-plane magnetic field $B_{\parallel}$, the total effective field $\boldsymbol{B}_{eff} = \boldsymbol{B}_{int} + \boldsymbol{B}_{\parallel}$ is tilted away from the surface normal, resulting in tilted spin polarization of the CB electrons. Optical transitions at energy $h\nu_D$ from an exciton formed mainly from the lower CB and corresponding to the dark exciton then become weakly allowed.

We applied the first-principles GW-BSE approach [20, 22, 58] to calculate the quasiparticle band structure, and both bright and dark excitonic states in monolayer WSe_2. Our calculation shows that the binding energy difference between the bright and dark $1s$ excitons is 17 meV (not to be confused with the difference in their excitation energies). As the calculated wavefunctions of the bright and dark excitons exhibit very similar spatial distributions, the difference in their binding energy could be understood by using a simple perturbation theory, in which the binding energy difference between the bright and dark states comes from the zeroth order energy correction caused by their different Hamiltonians. This difference in Hamiltonian arises from two factors: the different spin configuration of the bright and dark excitons, and the different effective masses of electrons in CB1 and CB2. For the former,

relative to the $S_z = \pm 1$ dark exciton, the $S_z = 0$ bright exciton experiences an additional repulsive electron-hole (e-h) exchange interaction, which shifts the bright exciton energy upwards by E^x (Fig. 3.7 a). For the latter, from the quasiparticle band structure, CB2 in WSe_2 has a larger mass than higher-lying CB1. This leads to an increased binding energy for the dark exciton; we denote the corresponding mass-induced shift as δE_0. Including the band splitting with the two many-body corrections, the bright-dark neutral exciton shift is $\Delta E_D \approx \Delta E_{CB}(40 \text{ meV}) + E^x(6 \text{ meV}) + \delta E_0(11 \text{ meV})$. For the overall shift, we obtain a value of $\Delta E_D = 57$ meV from our first-principles GW-BSE calculations, in good agreement with the experimental value of 47 meV [5].

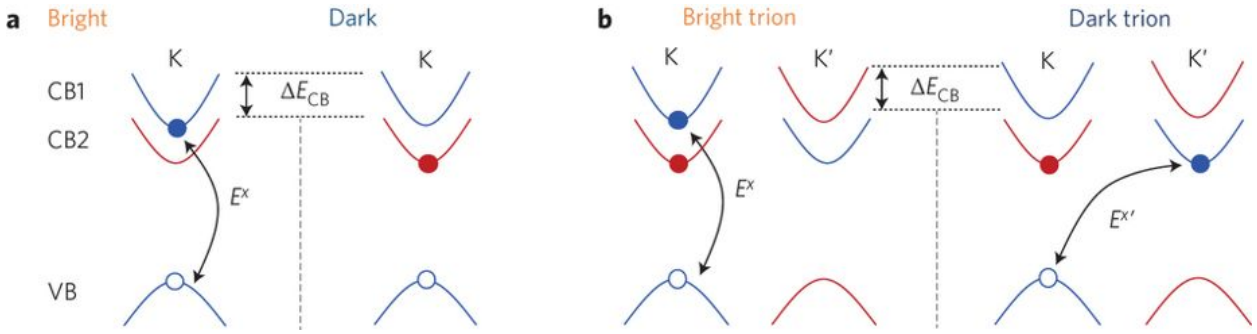

Figure 3.7: The blue and red lines represent spin-up and spin-down bands, respectively. (a), The spin-valley configuration of neutral bright and dark excitons. ΔE_{CB} denotes the energy splitting of the two CBs. The black line represents the e-h exchange interaction E^x for the ($S_z = 0$) bright exciton, which is absent for the ($S_z = \pm 1$) dark exciton. (b), Spin-valley configuration of the lowest-energy n-type bright and dark trion states. An e-h exchange interaction $E^{x'}$ is present for the intervalley ($S_z = 0$) e-h pair, as shown.

For the bright and dark states of the trions, the first-principles method that directly calculates their energy levels has not been implemented yet. However, we could estimate their energy difference by considering additional many-body effects in this three-body correlated state. For n-type trions, which are relevant for most experimental observations, the expected lowest-energy configurations for the bright and dark states are shown in Fig. 3.7, as dictated by having different electron valley-spin configurations. For the trions, ΔE_{CB} still gives the same single-particle contribution to ΔE_{DT}. However, unlike the neutral excitons, both the bright and dark trions experience e-h exchange interactions (Fig. 3.7 b): in the bright case, an intravalley exchange (E^x) and, in the dark case, an intervalley exchange interaction ($E^{x'}$). As the e-h wavefunction overlap of the $S_z = 0$ exciton is almost identical for the intervalley and intravalley configurations, our calculation indicates that E^x and $E^{x'}$ are very similar (within ~ 1 meV, estimated from the exchange energy differences between an interlayer exciton and an intravalley exciton). Therefore ΔE_{DT} can be approximated as $\Delta E_{DT} \approx \Delta E_{CB} + \delta E_T$, where δE_T is the mass-induced binding energy difference between

the bright and dark trions. Because δE_T is expected to be smaller than δE_0, we expect that ΔE_D exceeds ΔE_{DT}.

Despite their presence, the dark excitons and trions do not directly emit photons in the out-of-plane direction. The observation of the photoluminescence from these dark states hence requires either an in-plane magnetic field to allow photon emission in the out-of-plane direction, or an sensitive measurement of photons with its wavevector in the two-dimensional plane. We now discuss the first approach, which leads to the experimental observations of the dark exciton and trion states in monolayer WSe_2. In our experiment, we directly observed the emergence of dark states with application of an in-plane magnetic field. The color plot (Fig. 3.6 a) provides an overview of the photoluminescence spectra from an exfoliated WSe_2 monolayer for in-plane magnetic fields up to $\boldsymbol{B}_{\parallel} = 31\ T$. Two new states, labeled X_D and X_{DT}, are seen to emerge and become progressively more intense with increasing field.

The spin-orbit-induced splitting of the conduction bands can be attributed to an effective internal magnetic field $\boldsymbol{B}_{int}$, oriented perpendicular to the plane of the two-dimensional layer and acting on the electron spin (Fig. 3.6 b). If we apply an external in-plane magnetic field $\boldsymbol{B}_{\parallel}$, the total effective magnetic field acting on the conduction band electrons, $\boldsymbol{B}_{eff} = \boldsymbol{B}_{int} + \boldsymbol{B}_{\parallel}$, is now tilted away from the normal direction by an angle $\sim \frac{\boldsymbol{B}_{\parallel}}{\boldsymbol{B}_{int}}$ in small $\boldsymbol{B}_{\parallel}$ limit (Fig. 3.6 c). Since the expected spin splitting of conduction band of a few tens of millielectronvolts [75, 76] corresponds to $\boldsymbol{B}_{int}$ of hundreds of teslas, an appreciable tilt angle is achievable for $\boldsymbol{B}_{\parallel}$ of tens of teslas. On the other hand, the spin splitting in the VBs is ~ 10 times greater than in the conduction bands. $\boldsymbol{B}_{int}$ is correspondingly larger for the valence bands, and the tilting of $\boldsymbol{B}_{eff}$ for valence bands can be neglected. Consequently, $\boldsymbol{B}_{\parallel}$ causes the spin state of electrons in the lower conduction band to have a finite projection on the zero-field state in the upper valence band, and radiative recombination becomes weakly allowed for this otherwise forbidden transition (Fig. 3.6 b). We note that while an out-of-plane magnetic field causes measurable Zeeman shifts [79–81] and Landau quantization of valleys [82], the in-plane field produces only very minor Zeeman shifts and does not couple to the in-plane motion of electrons. The in-plane field thus allows us to probe directly the effects of spin mixing. Although the oscillator strength induced in the dark exciton by $\boldsymbol{B}_{\parallel}$ remains small, emission from the brightened dark states can still be significant at low temperature as a result of the large occupation number of the lower-lying dark state. In-plane magnetic fields have also been used to brighten optically dark excitons in quantum dots [83], carbon nanotubes [84] and quantum wells [85], although the physical mechanisms differ.

We now compare the energy shifts of the dark exciton and dark trion relative to the corresponding bright states. Based on the spectra presented above in Fig. 3.6, we find a bright-dark splitting of $\Delta E_D = 47 \pm 1$ meV for the neutral exciton. A similar analysis of the bright-dark splitting for the trion states yields $\Delta E_{DT} = 32 \pm 1$ meV. These values are in good agreement with our theory.

Chapter 4

Topological Effects and Optical Selection Rules

Identification and classification of topological characteristics in physical systems have revolutionized many areas of modern physics, providing deep insights to numerous phenomena ranging from the emergence of defects to new phases and phase transitions in matter [86–89]. It has been widely acknowledged that the topology of the electronic ground state greatly affects materials properties through mechanisms such as bulk-boundary correspondence [88, 89], quantum spin Hall effects [90, 91], and magnetoelectric polarizability [92]. However, the role of the topology in the optically excited states, and how it affects the properties of materials has largely remained unexplored. In this chapter, we present the discovery that the six-decade-old optical selection rule for conventional semiconductors must be replaced in two dimensions by a new simpler formula, owing to a topological characteristic inherent to the photoexcitation of excitons (correlated electron-hole states) [6]. The new selection rule states that optically active exciton states must have an angular momentum quantum number equal to the winding number of the interband optical transition matrix elements (a heretofore unrecognized topological invariant with the optical matrix elements viewed as a two-dimensional vector field in $\boldsymbol{k}$-space). This appealingly simple rule is illustrated with three gapped graphene systems - monolayer graphene with inequivalent sublattices and electrically biased bi- and tri-layer graphene, where highly unusual exciton series are discovered. Topology-related circular dichroism is predicted and verified through first-principles many-body theory calculations, and may be unambiguously detected using optical spectroscopy. This discovery reveals yet another important manifestation of topology in physics; it also opens opportunities for use of these predicted effects in gapped graphene systems for potential valleytronic applications.

Owing to the similarity between the electron-hole binding in a semiconductor and the electron-proton binding in a hydrogen atom, the hydrogenic model and their variants (for example, including electron-hole-separation-dependent screening effects) are usually adopted

in describing excitons in various dimensions, when the electron-hole correlation length of the exciton of interest is large compared to the unit cell size [93, 94]. Within this picture, the envelope functions of the excitonic states are hydrogen-like wave functions with even or odd parity and characterized by a series of quantum numbers. In linear optical spectroscopy, an exciton may be created or annihilated by absorbing or emitting a photon, respectively. Such coupling is allowed if the full many-body excitonic states have different parity from the ground state (these states are called optically active or bright excitons). For conventional semiconductors in which the electron (hole) states in the conduction (valence) band extreme forming the exciton are of single orbital character, this parity law together with the hydrogenic picture leads to the well-known optical selection rules [7], which would say: in dipole-allowed materials (e.g., GaAs, monolayer transition metal dichalcogenide, etc. [3, 55, 56, 94]), s-like excitons are optically active, whereas p-like excitons are optically inactive; in dipole-forbidden materials (e.g., Cu_2O [95]), the optically active excitons are p-like states, while s-like states are optically inactive.

However, for many reduced-dimensional systems of current interest, the states near the band extrema are of multiple orbital and spin components, and the bands can have nontrivial topological characteristics. Such nontrivial topological bands may be characterized by the behavior of the amplitudes of the components that compose a band state, viewed as a multicomponent spinor (the pseudospin) in $\boldsymbol{k}$ space. The pseudospins of the electron and hole states can develop a complex texture with respect to the crystal momentum $\boldsymbol{k}$ around the band extrema [88, 89, 96–99]. The pseudospin texture (viewed as a spinor field of $\boldsymbol{k}$) could in principle affect the energy levels, optical selection rules, and many other properties of the excitons. Recent studies have shown that Berry curvature flux leads to a fine energy-level splitting of the otherwise doubly degenerate hydrogenic $2p$ excitons in monolayer transition metal dichalcogenides [61, 62]. Yet, it remains unexplored whether central properties such as the optical selection rules are altered in materials with topological band characteristics.

4.1 A New Selection Rule at Two-Dimensions: Topology and Winding Numbers

We show here that the conventional optical selection rules, referencing to the exciton envelope functions, are not valid for two-dimensional systems with nontrivial band topology; they need to be distinctly replaced, in fact by a simple formula Eq. 4.4, incorporating topological effects [6]. In the important class of two-dimensional materials in which the pseudospins of states near the band extrema gain a nonzero winding number (topological invariant) as the carrier adiabatically traverses around the extremal k point (e.g., the K or K' valley in gapped graphene systems), a highly unconventional exciton series appears and exhibits novel valley-dependent optical selection rules and other photoactivities.

The exciton energies and wave functions in a semiconductor may be obtained from the so-

lutions of the Bethe-Salpeter equation of the interacting two-particle Green's function Eq. 1.12 [22]. Here for the purpose of illustration, we include a single conduction and a single valence band, forming a direct bandgap at a high symmetry point of the Brillouin zone. Generalization to the multiband case is straightforward, and our explicit first-principles results given below were performed with multiple valence and conduction bands. The simplified Bethe-Salpeter equation reads,

$$A^S_{\boldsymbol{k}}(E_{c,\boldsymbol{k}} - E_{v,\boldsymbol{k}}) + \Sigma_{\boldsymbol{k'}} A^S_{\boldsymbol{k'}} \langle cv, \boldsymbol{k}|\hat{K}^{eh}|cv, \boldsymbol{k'}\rangle = A^S_{\boldsymbol{k}}\Omega^S \tag{4.1}$$

The eigenstate of an exciton S is a coherent superposition of free electron-hole pairs at different $\boldsymbol{k}$ points $|S\rangle = \Sigma_{\boldsymbol{k}} A^S_{\boldsymbol{k}} |cv, \boldsymbol{k}\rangle$. The oscillator strength that relates to the intensity for optical transition to exciton S is given by Eq. 4.2.

$$I^S_e = \frac{2|\Sigma_{\boldsymbol{k}} A^S_{\boldsymbol{k}} \boldsymbol{e} \cdot \langle \phi_{c,\boldsymbol{k}}|\hat{\boldsymbol{p}}|\phi_{v,\boldsymbol{k}}\rangle|^2}{\Omega^S} \tag{4.2}$$

Although the exciton energies and oscillator strengths are physical observables and thus gauge invariant, the individual components in Eq. 4.2 the exciton envelope functions in $\boldsymbol{k}$ space and the interband optical matrix elements) may separately look different depending on a chosen gauge. This ambiguity arises because $|cv, \boldsymbol{k}\rangle$ could have an arbitrary phase, which would be canceled out by the complex conjugate of the same phase in $A_{\boldsymbol{k}}$. This gauge arbitrariness can be eliminated by requiring $A_{\boldsymbol{k}}$ of the lowest-energy s-like excitonic state to resemble that of a conventional hydrogenlike s orbital. Under this well-defined and intrinsically smooth gauge, we find that an analysis of Eq. 4.2 illuminates clearly the physical role of the exciton envelope function and of the topological characteristics of the interband optical matrix elements in optical transitions. In dipole-allowed conventional semiconductors, the interband optical matrix elements are nearly a constant around the extremal $\boldsymbol{k}$ point [7, 94]. Therefore, only s-like excitons have nonzero oscillator strength, as its envelope function in $\boldsymbol{k}$ space is isotropic in phase (i.e., no phase winding around the extremal $\boldsymbol{k}$ point).

Having topologically nontrivial bands in two dimensions with associated pseudospin texture of nonzero winding numbers will lead to both magnitude and phase modulations of the interband optical matrix elements with $\boldsymbol{k}$, represented by a two-dimensional vector field with a certain winding pattern. To illustrate this effect, we decompose the interband optical matrix element $\langle \phi_{c,\boldsymbol{k}}|\hat{\boldsymbol{p}}|\phi_{v,\boldsymbol{k}}\rangle$ into $p_{\boldsymbol{k}+} = \boldsymbol{e}_+ \cdot \langle \phi_{c,\boldsymbol{k}}|\hat{\boldsymbol{p}}|\phi_{v,\boldsymbol{k}}\rangle$ and $p_{\boldsymbol{k}-} = \boldsymbol{e}_- \cdot \langle \phi_{c,\boldsymbol{k}}|\hat{\boldsymbol{p}}|\phi_{v,\boldsymbol{k}}\rangle$, which correspond to coupling to left- and right-circularly polarized photon modes (σ_- and σ_+) respectively. The opposite sign between $\boldsymbol{e}$ and photon polarization arises because of a convention that we use in the light-matter coupling Hamiltonian, which reads $\boldsymbol{A} \cdot \boldsymbol{p}$ rather than $\boldsymbol{A}^* \cdot \boldsymbol{p}$. For topologically nontrivial bands, as illustrated below, $p_{\boldsymbol{k}+}$ and $p_{\boldsymbol{k}-}$ are typically

nonzero (except possibly at the extremal $\boldsymbol{k}$ point), and can be viewed as two vector fields that may differ in their winding patterns. (Note: The interband optical matrix elements $p_{\boldsymbol{k}\pm}$ are complex numbers determined only by the band states and are independent of the specific excitonic states.)

We shall show that the transition strength (brightness) and the specific light polarization needed for an excitonic optical transition are dictated by the phase winding of the exciton envelope function and that of the interband optical matrix elements. For an excitonic state of which the $\boldsymbol{k}$-space envelope function $A^S_{\boldsymbol{k}}$ is a highly localized function around an extremal $\boldsymbol{k}$ point (Wannier excitons), $A^S_{\boldsymbol{k}}$ and $p_{\boldsymbol{k}\pm}$ in the relevant small part of the Brillouin zone are dominated by a cylindrical angular phase dependence of $\sim e^{im\theta_{\boldsymbol{k}}}$ and $e^{il_\pm\theta_{\boldsymbol{k}}}$, respectively ($\theta_{\boldsymbol{k}}$ is defined as the angle $\boldsymbol{k}$ made with respect to the k_x axis) [7, 94]. Here, and in subsequent discussion, we shall define $\boldsymbol{k}$ as the wave vector measured from the extremal $\boldsymbol{k}$ point. Thus, m is the cylindrical angular quantum number of the exciton envelope function and $l_\pm$ are the winding numbers of $p_{\boldsymbol{k}_\pm}$. From Eq. 4.2, the oscillator strength for an optical transition to an excitonic state S by $\sigma_\pm$ photon (coupling to $p_{\boldsymbol{k}_\mp}$) is,

$$I^S_{\sigma_\pm} = \frac{2|\Sigma_{\boldsymbol{k}} f(|\boldsymbol{k}|)e^{i(m+l_\mp)\theta_{\boldsymbol{k}}}|^2}{\Omega^S} \tag{4.3}$$

where $f(|\boldsymbol{k}|)$ is the radial part in the summation. $I^S_{\sigma_\pm}$ is thus nonzero *only* when $m = -l_\mp$.

This set of selection rules is distinctly different from that in conventional semiconductors. For a system with discrete n-fold rotational symmetry, the general selection rule is

$$m = -l_\mp (\text{mod } n) \tag{4.4}$$

A generalization to systems with discrete rotational symmetries is given in the supplemental material of Ref. [6]. As a result, excitons with different angular quantum numbers (i.e., different m) would couple differently to $p_{\boldsymbol{k}+}$ and $p_{\boldsymbol{k}-}$, causing multiple bright excitons each accessible by σ_- and σ_+ photons. We note that Eq. 4.4 thus incorporates and generalizes the conventional selection rules for Wannier excitons to all two-dimensional semiconductors with a single critical point (or no critical point) where excitonic optical transitions happen. Similar selection rules on a gapped chiral fermion model have been obtained in Ref. [100].

4.2 Applications of the Selection Rule: Gapped Graphene Systems

An ideal set of materials to illustrate the predicted novel excitonic physics is the gapped graphene systems, in which a band gap and a layer-number-dependent pseudospin texture emerge from an induced broken inversion symmetry that may be tuned. We consider three (already experimentally achieved) systems based on 1-3 layers of graphene [101–104]. For monolayer graphene, inversion symmetry is broken by placing the graphene layer on top of a monolayer of hexagonal boron nitride (the graphene and boron nitride monolayer are taken to be commensurate here, with the two sublattices A and B of graphene sitting directly on top of the boron and nitrogen atoms, respectively. We note that lattice incommensurability between the two materials and the moiré pattern in realistic devices may change the measured bandgap from the calculated value here.). For bilayer (in a Bernal stacking order) and trilayer graphene (in a rhombohedral stacking order), inversion symmetry is broken by applying an external electric field along the out-of-plane direction. In our first-principles GW-BSE calculations presented below, the applied electric field was set to 0.13 V/Å, an experimentally studied value [103]. Modifying the applied electric field strength, which determines the size of the induced band gap, does not change the physics discussed here.

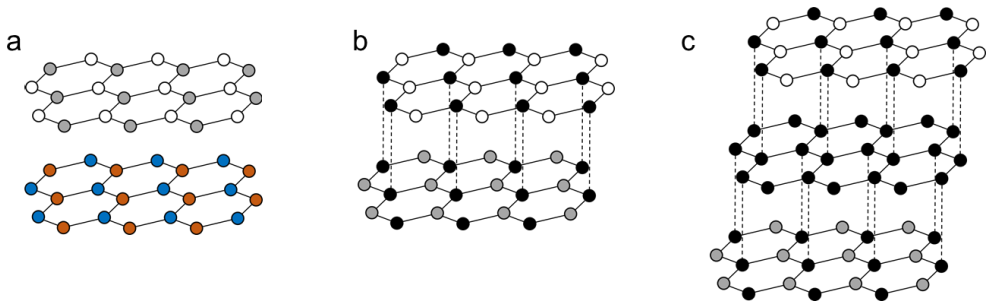

Figure 4.1: Schematic structures of gapped graphene systems. (a) Structure of monolayer graphene with inequivalent sublattices. The carbon atoms on top of boron and nitrogen atoms are colored white and grey, respectively. The hexagonal boron nitride monolayer placed below the graphene layer makes the two graphene sublattices inequivalent. (b, c) Structure of Bernal-stacked bilayer and rhombohedral- (ABC-) stacked trilayer graphene. The dashed lines represent vertical carbon bonds between neighboring layers. The carbon atoms forming these bonds are colored black

For the gapped graphene systems studied, density functional theory calculations are performed within the local density approximation formalism using the Quantum Espresso package [25, 105] to determine their ground-state properties. First-principles GW [20] and GW-BSE [22] methods are employed to calculate the quasiparticle band structure and excitonic states, respectively, using the BerkeleyGW package [58].

In the GW and GW-BSE calculations, the dielectric matrix for the screened Coulomb interaction is constructed with a two-dimensional truncation scheme and with an energy cutoff of 8 Ry. Close scrutiny is needed for the Brillouin zone sampling in the excited-state calculations. For calculations of the quasiparticle band structure, a 150×150 $\boldsymbol{k}$-point mesh in the Brillouin zone is necessary to converge the bandgap within 3 meV. For the calculation of excitons, a patched sampling scheme is used to solve the BSE for the excitonic states in the individual K and K' valleys. The sampling density is equivalent to a uniform 450×450 $\boldsymbol{k}$-point mesh in the Brillouin zone. For monolayer graphene, a 450×450 $\boldsymbol{k}$-point mesh is moreover interpolated into a 1500×1500 mesh to converge the exciton energy levels to within 2 meV.

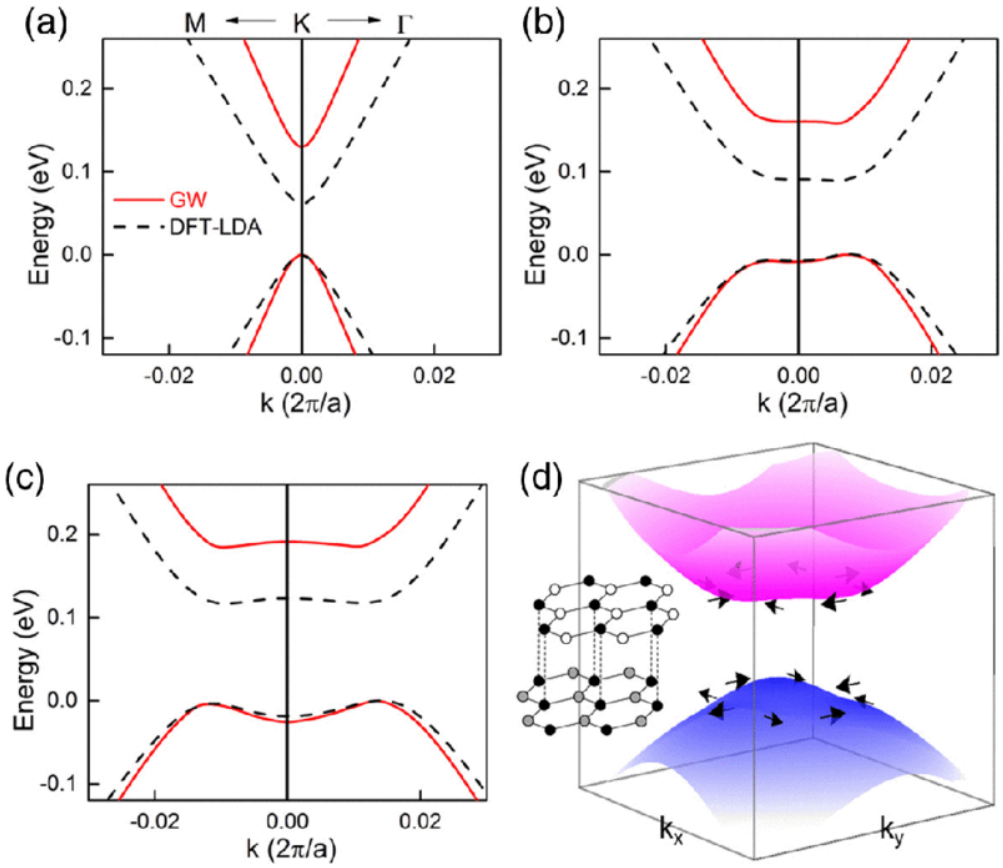

Figure 4.2: Calculated band structure and pseudospin (orbital components) winding of gapped graphene systems. Bottom conduction band and top valence band of monolayer graphene with broken A and B sublattice symmetry (a), biased Bernal-stacked bilayer graphene (b), and biased rhombohedral-stacked trilayer graphene (c). Red solid lines and black dashed lines are GW and DFT-LDA bands, respectively. The K point is set at $k = 0$. Positive and negative k values denote the $K - \Gamma$ and $K - M$ direction, respectively. (d) Orbital pseudospin winding in biased bilayer graphene. Inset: Structure of biased bilayer graphene. The carbon atoms forming bonds with a neighboring layer are colored black.

The gapped graphene systems of 1, 2, and 3 atomic layers studied have GW quasiparticle band gaps of 130, 159, and 185 meV (Fig. 4.2), respectively. These values are much larger than their corresponding Kohn-Sham band gaps (within the local density approximation) of 62, 90, and 118 meV, respectively, owing to electron self-energy effects. For biased bilayer and trilayer graphene, the top valence and bottom conduction bands at the K and K' valleys develop a Mexican-hat-like shape. The pseudospin texture of the states in bilayer graphene is schematically shown in Fig. 4.2 (d), where the amplitude of the carbon π orbitals develops a phase winding around the band extreme [106].

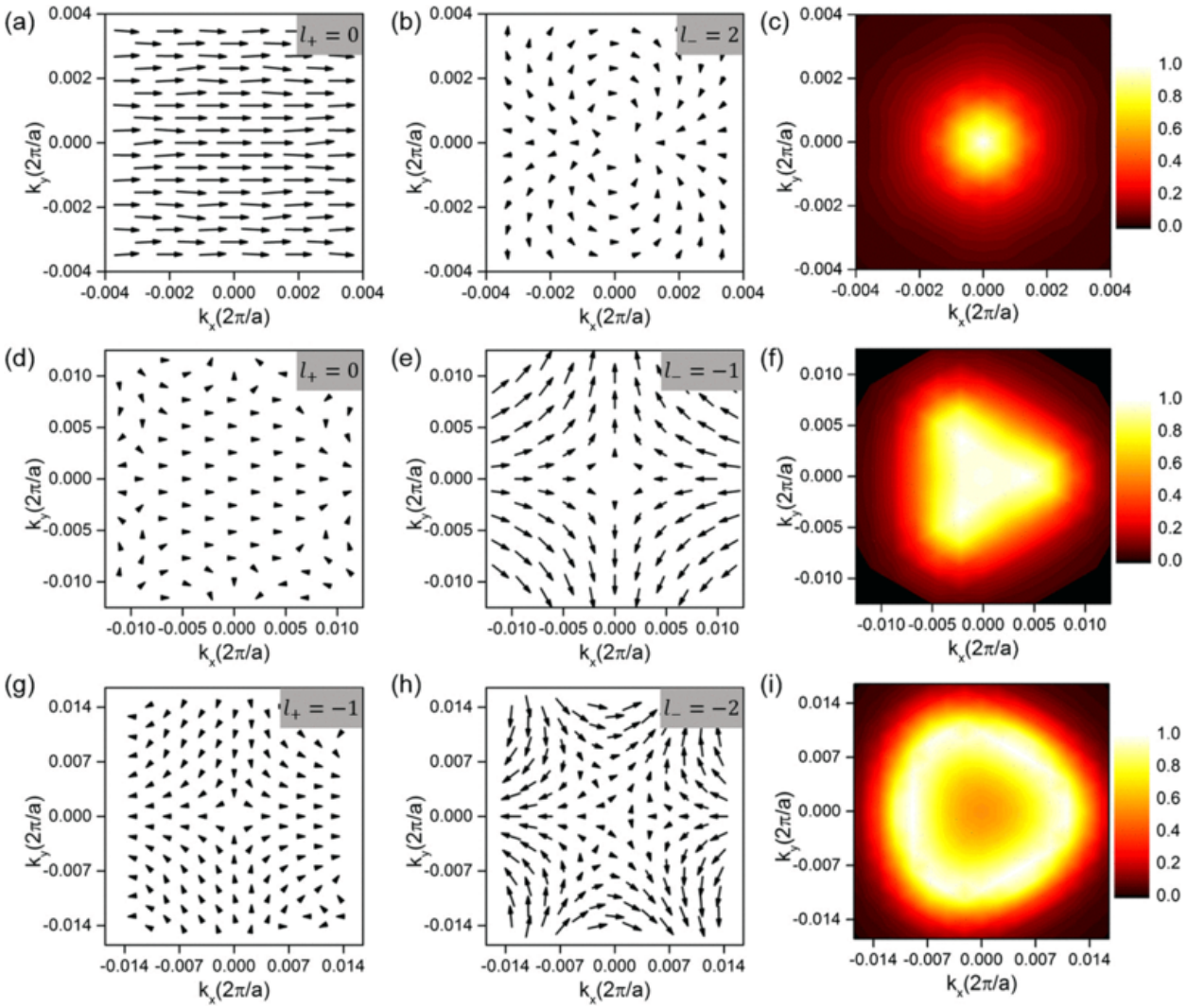

Figure 4.3: $K-$valley interband optical transition matrix elements and $1s$ exciton envelope function in $\boldsymbol{k}$-space. The K point is placed at the origin. Optical interband transition matrix element and its winding number for light of (a) left circular polarization $p_{\boldsymbol{k}_+}$ and (b) right circular polarization $p_{\boldsymbol{k}_-}$ in monolayer graphene with inequivalent sublattices. The direction and length of an arrow denote, respectively, the phase and the magnitude of the corresponding matrix element. (d) $p_{\boldsymbol{k}_+}$ and (e) $p_{\boldsymbol{k}_-}$ in biased bilayer graphene. (g) $p_{\boldsymbol{k}_+}$ and (h) $p_{\boldsymbol{k}_-}$ in biased trilayer graphene. (c),(f),(i) $1s$ exciton envelope function in $\boldsymbol{k}$-space in gapped monolayer graphene, biased bilayer graphene, and biased trilayer graphene, respectively. The envelope functions show in color scale the magnitude of the free electron-hole pair excitation at each $\boldsymbol{k}$, normalized to its largest value in each plot.

The very different pseudospin texture of the bands in the three gapped graphene systems

gives a strong layer-number- and valley-index-dependent interband optical matrix element winding pattern for each. We show in Fig. 4.3 the winding pattern of $p_{\boldsymbol{k}_+}$ and $p_{\boldsymbol{k}_-}$ in the K valley, defined using the gauge procedure as described above. The complex quantity $p_{\boldsymbol{k}_+}$ or $p_{\boldsymbol{k}_-}$ (given by a magnitude and a phase $\phi_{\boldsymbol{k}}$) are represented by an arrow with its length proportional to the magnitude and its orientation pointing along the direction with angle $\phi_{\boldsymbol{k}}$ to the x axis. In monolayer graphene with inequivalent A and B sublattices (Fig. 4.3 (a) and (b)), $p_{\boldsymbol{k}_+}$ is nearly constant in magnitude and phase (arrows with constant length and orientation) and has a winding number $l_+ = 0$ for any contours enclosing K, whereas $p_{\boldsymbol{k}_-}$ is much smaller in magnitude and its phase (the orientation of the arrows) winds counter clockwise around the K point twice after completing any counter clockwise contour enclosing K (winding number of $l_- = 2$). This analysis, making use of the selection rules deduced above, predicts an optically active s exciton series, as well as a weakly active d exciton series ($m = -2$ in the K valley). In biased bilayer graphene, the pseudospin texture Fig. 4.2 (d) leads to a winding number of $l_- = -1$ for the interband optical matrix element $p_{\boldsymbol{k}_-}$ [Fig. 4.3 (e)]. Compared with $p_{\boldsymbol{k}_-}$, $p_{\boldsymbol{k}_+}$ is much smaller in magnitude (Fig. 4.3 (d)), but remains constant in both magnitude and phase around the K point (winding number $l_+ = 0$). We therefore predict that (i) unlike the case of gapped monolayer graphene, the p exciton series ($m = 1$ in the K valley) is now optically very active, (ii) the s exciton series is still somewhat optically active, but has a much smaller oscillator strength than the p exciton series, and (iii) importantly, the photoexcitation of the s excitons and p excitons at a given valley (K or K') requires opposite circular polarization in biased bilayer graphene. The interband optical matrix elements in biased trilayer graphene have even more features (Fig. 4.3 (g) and (h)), leading to a winding number of $l_+ = -1$ and $l_- = -2$ for $p_{\boldsymbol{k}_+}$ and $p_{\boldsymbol{k}_-}$, respectively, at the K valley. Moreover, near the extremal k-point, the amplitude of $p_{\boldsymbol{k}_+}$ depends linearly on $|\boldsymbol{k}|$, while that of $p_{\boldsymbol{k}_-}$ depends quadratically on $|\boldsymbol{k}|$. In the $\boldsymbol{k}$-space area where excitons reside (see Fig. 4.3 (i)), the amplitude of $p_{\boldsymbol{k}_-}$ is much larger than that of $p_{\boldsymbol{k}_+}$. Eq. 4.4 above therefore predicts: (i) unlike the case of either monolayer or bilayer gapped graphene, the s exciton series is optically inactive; (ii) the p exciton series are somewhat optically active, but having a much smaller oscillator strength than the d exciton series; and (iii) the p excitons and d excitons at a given valley (K- or K'- valley) have opposite helicity. The $1s$ exciton envelope functions of the three gapped graphene systems studied are shown in Figs. 4.3 (c), (f), and (i). Our new selection-rule predictions based on topological effects are completely borne out by our explicit GW-BSE calculations of the optical absorption spectra.

The physics of interband optical matrix element winding numbers thus leads to novel exciton series in the gapped graphene systems, with each valley hosting multiple optically active excitons whose creation requires different circular polarization. We show in Fig. 4.4 the first-principles GW-BSE calculated energy levels, required circular polarization, and oscillator strength of the first six lowest-energy excitons in the K and K' valley of each system. The calculated binding energies of the lowest-energy exciton state of the 1-, 2-, and 3-layer systems are 34, 52, and 45 meV, respectively. In gapped monolayer graphene with inequivalent sublattices (Fig. 4.4 (a)), as expected, the s-like excitons are optically bright.

The $1s$ exciton in the K and K' valleys can be selectively excited by σ_- and σ_+ light, respectively, similar to monolayer transition metal dichalcogenides [1, 2, 33, 34]. In biased bilayer graphene (Fig. 4.4 (b)), however, the optically most active exciton becomes a $2p$ state that is located at 13 meV above the lowest-energy $1s$ state, with an oscillator strength ~ 20 times larger than that of the $1s$ exciton. Moreover, the circular polarization needed for excitation of the $2p$ state is opposite to that of the $1s$ state, a feature that is directly predicted from the interband optical matrix element winding patterns depicted in Figs. 4.3 (d) and (e). In the biased trilayer graphene (Fig. 4.4 (c)), the lowest-energy $1s$ exciton is optically inactive from the matrix element winding patterns in Figs. 4.3 (g) and (h). Because of a significant deviation of the band dispersion from a parabola, we are no longer able to associate the higher-energy excitonic states with a clear principal quantum number. However, a pair of nearly degenerate excitons with p-like and d-like orbital characters could still be identified, located at ~ 9 meV above the $1s$ state. These two states are mixed by a trigonal wrapping mechanism. In the K valley, both states are excitable with σ_+ polarized light, and couple strongly (optically bright) to the ground state via $p_{\boldsymbol{k}_-}$ in Fig. 4.3 (h), either directly or through a trigonal warping effect. (There is also a weakly active p-like exciton at ~ 4 meV above the $1s$ state, but couple to light of an opposite helicity than the above-mentioned $p-d$ exciton). In all three cases, the circular polarization for excitation of every bright exciton in the K' valley is opposite to that of a degenerate-in-energy counterpart in the K valley due to time-reversal symmetry.

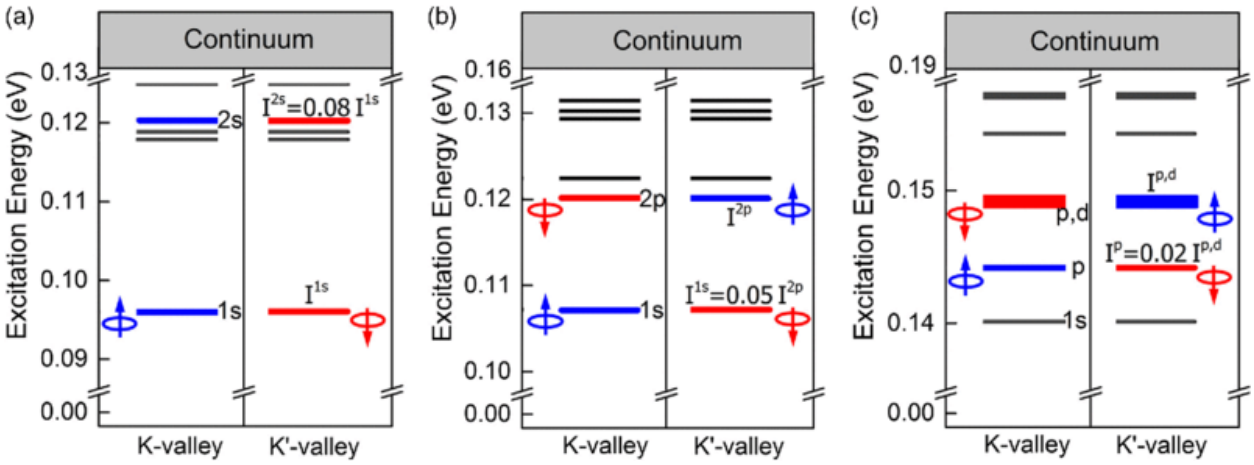

Figure 4.4: K-valley and K'-valley exciton energy levels and valley-exciton selective circular dichroism in (a) monolayer graphene with inequivalent A and B sublattices, (b) biased bilayer graphene, and (c) biased-trilayer graphene. Left (right) part of each panel depicts the K-valley (K'-valley) exciton energy levels. The first six lowest-energy excitons are shown in each plot. Black lines indicate dark states (with maximum oscillator strength $< 1\%$ of the brightest exciton in each plot). The oscillator strength (I) of each bright state is expressed in terms of that of the brightest state, for unpolarized light. Blue and red lines (or circles) indicate bright states that are excitable from the ground state with left- and right- circularly polarized light, respectively.

Until now, we have presented the discovery of a set of new unifying optical selection rules, as well as results of novel bright exciton series, arising from band topological effects in two-dimensional semiconductors. All two-dimensional systems, with or without nontrivial band topology, have optical selection rules given by Eq. 4.4 replacing the conventional ones for Wannier excitons. Owing to the Poincaré-Hopf theorem, which in the present context states that the sum of the winding numbers from all band extrema in the two-dimensional Brillouin zone should equal to zero (the Euler characteristics of a two-dimensional torus), one should look for the predicted nonconventional selection rules in the excitonic spectra of multivalley two-dimensional materials. We note here that the Poincaré-Hopf theorem applies to the two polarizations separately.

In three dimensions, we expect that the optical selection rules would also be affected by the band topology and winding number physics. The winding patterns should be more complicated, and possibly involve more than one "winding number" around a high-symmetry $\boldsymbol{k}$ point in the Brillouin zone. One should look for such phenomena in materials with non-trivial band topology.

4.3 The Experimental Probe of Excitons in Gapped Bilayer Graphene and Other Proposed Experiments

The excitons in gapped bilayer graphene systems have been experimentally observed [8]. The experiment uses a photocurrent spectroscopy to measure the excitons in high-quality hBN-encapsulated bilayer graphene devices. The BN-bilayer graphene-BN stack sits on a piece of graphite local back gate, and a 14-nm layer of nickel/chrome alloy is deposited on top as the semitransparent top gate. Source and drain electrodes are used to apply voltage bias and measure photocurrent generated in the device. Under infrared illumination, electron-hole pairs are generated in bilayer graphene, and they lead to a significant photocurrent proportional to the optical absorption in the bilayer. Optical absorption spectra can be obtained by a modified Fourier transform infrared (FTIR) spectroscopy, where the bilayer graphene photocurrent signal as a function of the delay in the FTIR spectroscopy is recorded.

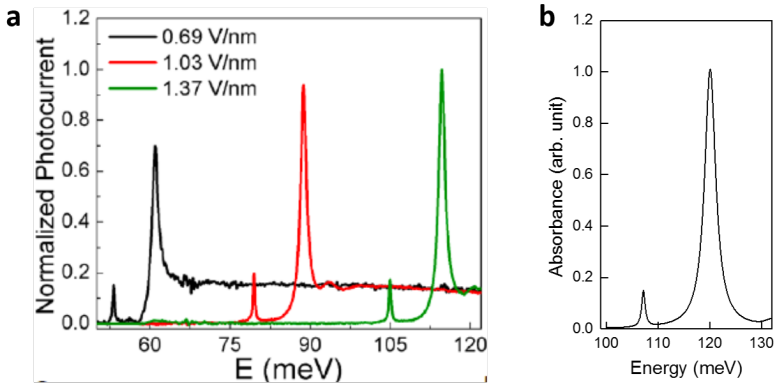

Figure 4.5: (a) Normalized photocurrent spectrum at displacement field D = 0.69, 1.03, and 1.37 V/nm in gapped bilayer graphene. Both exciton peaks blue-shift as D increases and the bandgap opens more. All spectra converge to a line at energies above the higher-energy peak. (b) Calculated optical absorbance as a function of energy at D = 1.3 V/nm in gapped bilayer graphene.

A typical photocurrent interferogram for gapped bilayer graphene in the frequency domain has two sharp absorption peaks, and a continuous smooth absorption above the higher-energy peak. Fig. 4.5 a shows three normalized photocurrent spectra taken at displacement fields of D = 0.69, 1.03, and 1.37 V/nm, which are achieved by controlling the top and bottom gate

voltages. As the bandgap widens with increasing D, the two peaks shift to higher energies. The calculated optical absorption spectrum in Fig. 4.5 b agrees well the experiments.

The magneto-optical spectra of the gapped bilayer graphene show more interesting features due to a combination of excitonic and Berry phase effects. Some results, such as the nearly absent magnetic moment of the excitonic $2p$ states, are not well understood. Interested readers should refer to Ref. [8] for details.

Moreover, the new selection rule predicted can lead to a new valley-state selective circular dichroism. We now show how our predicted novel excitonic physics may be experimentally verified by polarization-resolved optical spectroscopy. This proposed experiment is based on the fact that the phonon-assisted intravalley exciton energy relaxation is much more efficient than phonon-assisted intervalley exciton energy relaxation [33, 107–109]. As a result, optically created excitons in one valley will predominantly relax to the lowest-energy exciton in the same valley (due to the scattering between intermediate excitonic band states by acoustic phonons or the interlayer breathing mode). Taking biased bilayer graphene as an example, resonant σ_- excitations of the K-valley $1s$ exciton will induce a σ_- photoluminescence from the excited excitons themselves, whereas resonant σ_- excitations of the K'-valley $2p$ exciton will induce photoluminescence from the K'-valley $1s$ exciton following energy relaxation from the $2p$ state to the $1s$ state (Fig. 4.6). As the optical circular polarization needed to couple the ground state to the $1s$ exciton is opposite to that of the $2p$ exciton in the same valley (Fig. 4.4 b), the latter process would produce a σ_+ photoluminescence. This predicted new phenomenon in biased bilayer graphene is distinctly different from the behavior of photoluminescence in monolayer transition metal dichalcogenides or gapped monolayer graphene [1, 2, 33, 34], because the circular polarization of the luminescence light for the former would depend not only on the polarization of the incident light, but also on the excitation energy (i.e., whether it is in the range of the $1s$ or $2p$ exciton energy)

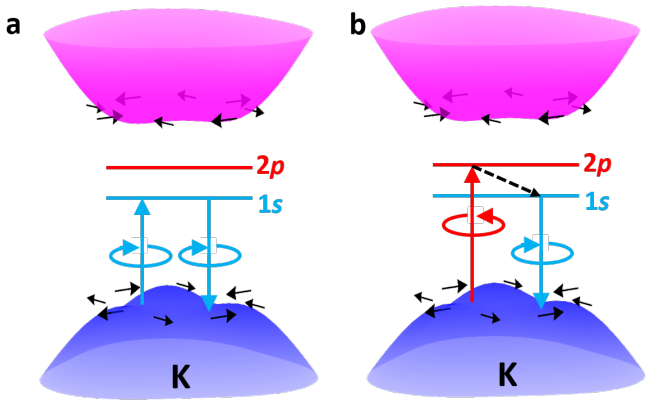

Figure 4.6: In gapped bilayer graphene, (a) schematic optical excitation and photoluminescence in the K valley using resonant σ_- excitations of the $1s$ exciton; (b) schematic optical excitation and photoluminescence in the K valley using resonant σ_+ excitations of the $2p$ exciton.

Chapter 5

Van der Waals Engineering of Optical Transitions

The last chapter of this thesis will focus on the materials engineering aspect of the van der Waals layered materials. Engineering the properties of materials is of central importance in modern science and technology. In conventional bulk materials, the property changes are realized mainly through modifying the chemical bonds and crystalline structures, or introducing dopant atoms. Recent studies in van der Waals coupled two-dimensional layered materials have demonstrated a different way of materials engineering through modifying interlayer interactions at the material interfaces [6, 8, 9, 103, 110–114], because the interlayer interactions in these materials can be easily controlled by changing interlayer stacking configurations and/or applying external fields. In this chapter, we discuss the engineering of interlayer interactions of transition metal dichalcogenides and black phosphorus bilayers, which significantly tunes the optical transitions in these materials [9, 10].

Recent studies on van der Waals coupled 2D layered materials have unveiled a wide range of novel phenomena distinctly different from their bulk counterparts [110, 115, 116]. Engineering the properties of these materials, in particular through the interlayer interactions, has opened up a new regime of materials engineering. In sharp contrast to conventional bulk materials, the interlayer interactions in van der Waals coupled materials can be controlled mainly by two approaches, that is, designing interlayer stacking configurations [9, 111–113] and/or applying external fields [6, 8, 103, 114]. The former approach relies on the relatively weak van der Waals interaction between neighboring layers. Compared with the interfaces of bulk semiconductors, where strong covalent or ionic bonds between heteroatoms lead to a well-aligned interface, van der Waals coupled materials can have various stacking configurations with different twist angle between neighboring layers. These twist structures can either be realized by direct growth methods or controlled by transfer methods, depending on the specific van der Waals material of interest. The latter approach for engineering interlayer interactions relies on the possibility to electrically gate ultrathin van der Waals coupled layers

without changing the pristine material structure, a goal harder to realize in bulk semiconductors. When a gate voltage is applied along the out-of-plane direction, the displacement field between the layers can be as large as 0.3 V/Å [103]. For van der Waals coupled materials, both approaches are effective in tuning their electronic, mechanical, optical properties, etc. The band structures can be easily modified, since the hybridization of the electronic states from adjacent layers significantly depends on both the stacking configuration and the out-of-plane electric field.

These two approaches have been successfully deployed in a variety of materials systems, leading to unusual materials properties distinct from either monolayer- or few-layer-van der Waals crystals exfoliated from the bulk. For example, in bilayer graphene, by changing the relative twist angle between the two layers, van Hove singularities (vHs) emerge in its band structure [111]. Furthermore, the energy and density of states of the vHs are controllable by the twist angle. At the so called "magic angle", the density of states near the Fermi level become very large arising from to a "flat" band [117]. This enhanced electron density of states is closely related to the origin of the Mott insulating and superconducting phases observed [118, 119]. In bilayers transition metal dichalcogenide, the circularly polarized photoluminescence can be continuously tuned via an electric field applied perpendicular to the two-dimensional film [114]. Indeed, an increasing number of works have shown that the interfacial engineering of van der Waals coupling is of significant promise in the contemporary material engineering, for future high-performance electronic, photovoltaic, photonics, and optoelectronic devices. The rapid expansion in two-dimensional materials species, ranging from metallic monolayer such as $NbSe_2$ [120, 121] to newly discovered magnetic semiconductors such as CrI_3 and $Cr_2Ge_2Te_6$ [122, 123] also fuel the rapid development of this research area.

In this chapter, two theoretical works on the van der Waal interfacial engineering of optical transitions will be discussed together with related experimental results [9, 10].

5.1 Twist-Angle Dependent Optical Properties of Transition Metal Dichalcogenide Bilayers

The aim of this study is to investigate how the electronic structures and optical transitions of a layered semiconductor two-dimensional material is modified by changing its interlayer stacking configuration. The initial speculation of this study was that, for a few-layer semiconducting two-dimensional material, the modulation of its electronic and optical properties caused by the tuning of its interlayer coupling would be more significant than the modulations in few-layer graphene under the same tuning condition. The simplest model system that we consider here is a MoS_2 bilayer, where the degree of freedoms in the tuning of the interlayer stacking configurations are the interlayer lateral shift of the atomic registry and the interlayer twist angles.

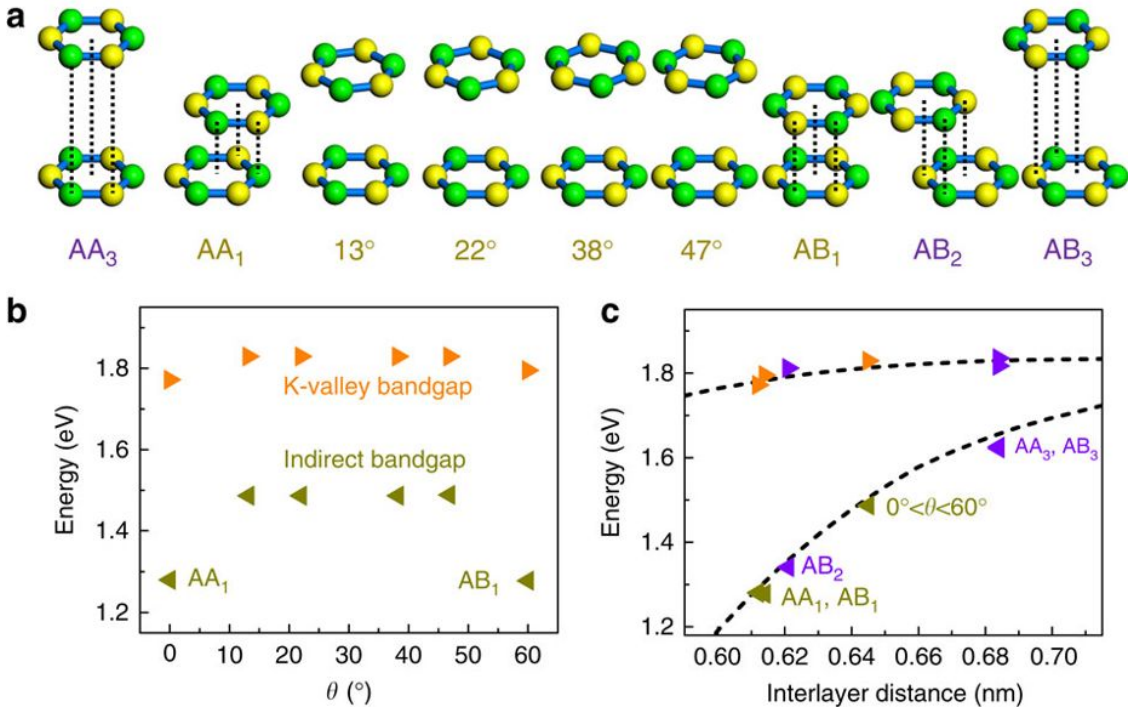

Figure 5.1: (a) Schematics of MoS_2 bilayers with AA, AB and different twisted configurations. Mo atoms are shown as green spheres; two S atoms of the same horizontal position are presented by one yellow sphere. Interlayer distance variations are exaggerated for illustration. The interlayer separation is $\sim$ 0.61 nm for AA_1 and AB_1 stacking, $\sim$ 0.62 nm for AB_2 stacking, $\sim$ 0.68 nm for AA_3 and AB_3 stacking and $\sim$ 0.65 nm for the four twisted bilayers. (b) Calculated values for the Kohn-Sham K-valley direct bandgap (orange) and indirect bandgap (dark yellow) for the energetically favorable structures at each twist angle. (c) The calculated Kohn-Sham bandgap as a function of the interlayer distance for different stacking configurations (symbols). The dashed curve shows the bandgap values for AA_1 stacking with artificially varied interlayer separation. Their comparison indicates that the electronic coupling in MoS_2 bilayer is largely determined by the interlayer separation and does not depend explicitly on the horizontal registration of the two layers.

We perform first-principles calculations on the twist-angle- and interlayer-lateral-shift- dependent ground state energies and band structures of MoS_2 bilayers from density functional theory within the local density approximation [25, 105]. Spin-orbit coupling is not included in the calculations, since the coupling would most possibly induce a constant shift in ground state energies/bandgaps, rather than change the trend of the stacking dependent results. A supercell approach is used to describe the twisted bilayers, with the crystalline alignment of the top layer oriented at a commensurate angle with respect to the bottom layer. $\theta = 0°$, $60°$ and four intermediate commensurate angles ($\theta \approx 13°, 22°, 38°$, and $47°$) are studied in

our calculations Fig. 5.1 a. When $\theta = 0^\circ$ (AA) or 60° (AB), there are three high-symmetry stacking configurations: the S atoms in the top layer are placed above (1) the Mo atoms (AA_1 and AB_1), (2) the hexagonal centers (AA_2 and AB_2), or (3) the S atoms in the bottom layer (AA_3 and AB_3). As the AA_1 and the AA_2 configurations are related by spatial inversion, we use AA_1 to denote these two equivalent structures. Among these high-symmetry configurations, AA_1 and AB_1 have the lowest energies and are presumably the most stable (they are almost degenerate in energy).

In Fig. 5.2 d, We show the density functional theory calculated band structure of the AA_1 stacked bilayer (the band structures of the AB_1 and AB_2 stacked bilayers are similar). Comparing with the band structure of a monolayer (Fig. 5.2 c) that has a direct bandgap (transition I) of around 1.85 eV, the bilayers have an indirect bandgap resulting from the interlayer electronic coupling, in which the doubly degenerate valence band splits into two branches near the Γ point and the upper branch rises to an energy higher than the valence band at the K point in the monolayer Brillouin zone (Fig. 5.2 d). Therefore, the indirect bandgap (transition II) energy reflects directly the interlayer electronic coupling strength: the smaller the indirect bandgap, the stronger the coupling strength.

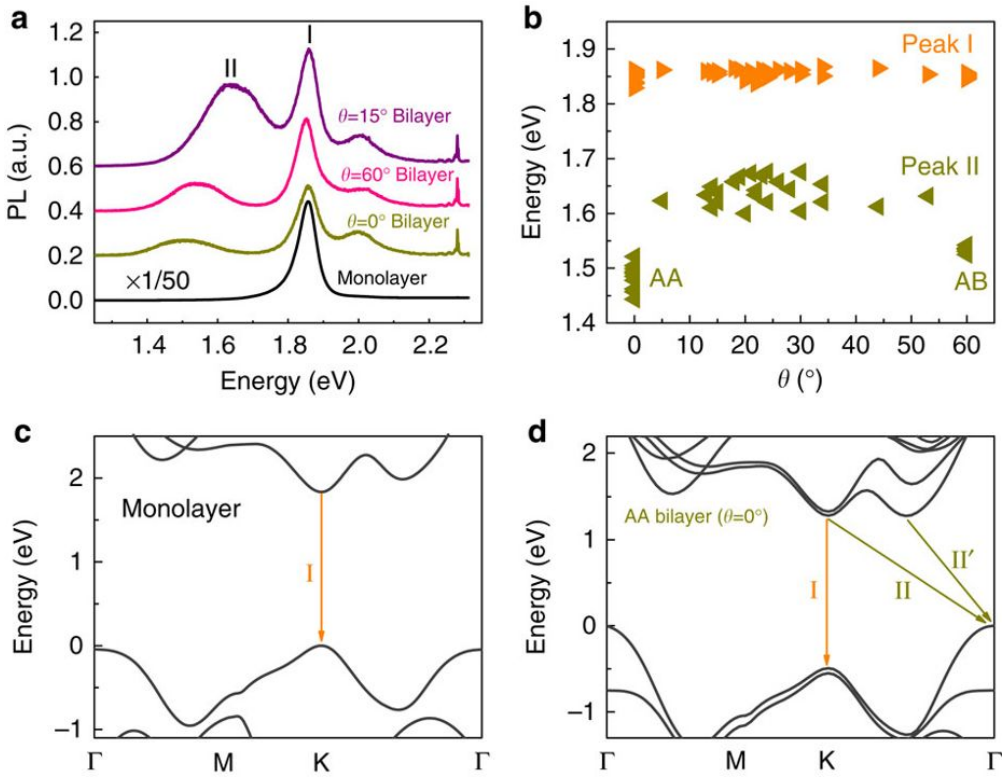

Figure 5.2: (a) Photoluminescence spectra of MoS_2 monolayer and bilayers with twist angles of $\theta = 0°$, 15° and 60°. (b) Dependence of photoluminescence peak energies on the twist angle for 44 MoS_2 bilayers. The peak I energy is almost identical for all bilayers. The peak II energy is lowest for AA- and AB-stacked bilayers, and is higher but at a nearly constant value for other twist angles. (c,d) Calculated Kohn-Sham band structure of a MoS_2 monolayer using the local density approximation (c) and of the most energetically favorable AA-stacked bilayer (d). Transition I is associated with the K-valley direct bandgap (peak I in photoluminescence spectra). The indirect bandgap transitions II and II have nearly degenerate energy and either may be associated with the peak II in the photoluminescence spectra.

For the four twisted configurations, there are no high-symmetry configurations, and the atoms in the two layers have nearly random relative distributions. As a result, the total energy of the system is virtually independent on the lateral shift for a twisted bilayer. Our calculated Kohn-Sham K-valley direct bandgaps (that is, bandgaps responsible for the direct optical transition originating from the K-valley of the first Brillouin zone of a monolayer MoS_2 unit cell) and the indirect bandgaps (that is, the smallest bandgap between the valence band top and the conduction band minimum) for AA_1, AB_1 and the four twisted configurations are shown in Fig. 5.1.b. We find that the trend in bandgap variation with the twist angle matches well with the experimental observation in Fig. 2b: The K-valley

direct bandgap remains largely unchanged, but the indirect bandgap is much smaller in AA- and AB-stacked bilayers compared with all other twist angles. We note that the Kohn-Sham bandgaps should not be directly compared with the measured optical bandgaps because of the neglect of the quasiparticle self-energy and electron-hole interaction effect [53, 54]; however, these effects tend to cancel each other in the transition energies. The trends in the twist angle dependence should be correct.

In experiments, we systematically studied 44 MoS_2 bilayers with various twist angles. Fig. 5.2 b displays the transition energies of I and II in all measured bilayers that exhibit interesting dependence on the twist angle. In contrast to a virtually unchanged transition I energy (direct exciton transition), the II energy (indirect transition) is lowest for perfect registered (that is, AA- and AB-stacked) bilayers, and has a higher but nearly constant value for all other twist angles. This means that the interlayer electronic coupling is significant for all twist angles, but is the strongest in AA- or AB-stacked MoS_2 bilayers.

We further examine the evolution of the calculated interlayer distance (defined by the averaged Mo-Mo interlayer separation). A strong variation of the interlayer distance on the stacking configuration is found, as illustrated in an exaggerated fashion in Fig. 5.1 a (see detailed value in Table 5.1). The higher energy AA_3 and AB_3 configurations have the largest interlayer distance of ~ 0.68 nm; the two energetically favorable AA_1, and AB_1 configurations are found to have the smallest interlayer distance of ~ 0.61 nm, and all the twisted configurations have almost identical interlayer distances at ~ 0.65 nm. If we only focus on the lower energy configurations (AA_1, AB_1 and the four twisted configurations), this trend in interlayer distance evolution with twist angle is similar to the evolution of the indirect bandgap (Fig. 5.1 b).

The configuration-dependent interlayer distance in bilayer MoS_2 can be understood physically by steric effects that arise from the fact that each atom occupies a certain amount of space that strongly repulse other atoms owing to a significant energy cost from overlapping electron clouds. Between two vertically stacked MoS_2 layers, the only interlayer adjacent atoms are S atoms. In the energetically unfavorable AA_3 or AB_3 stacking configurations, the S atoms of the top layer sit directly on the S atoms of the bottom layer in an eclipsed fashion, leading to a strong repulsion and the largest interlayer distance. In the energetically favorable AA_1 or AB_1 stacking configurations, on the other hand, the S atoms of the top layer sit on the trigonal vacancies of the S atoms of the bottom layer in a staggered fashion, resulting in reduced repulsion and the smallest interlayer distance. For other twist angles, the S atoms of the top layer sit nearly randomly relative to the S atoms of the bottom layer, and therefore, the interlayer distance is constant and roughly at the average of that of the most stable AA_1 (AB_1) and unstable AA_3 (AB_3) stacking configurations. Consequently, the variation in interlayer distance has a simple geometric origin, which is determined by the lateral registration of adjacent S layers. Such steric effects determine the interlayer distance that in turn modifies both the interlayer electronic coupling strengths and indirect optical

transition energies.

Interestingly, if we examine separately the explicit dependence of the electronic coupling (and the corresponding indirect bandgap energy) on the interlayer vertical separation and horizontal registration, only the former has a significant effect. For example, we can artificially vary the interlayer distance of the AA_1-stacked bilayer in our first-principles calculation and calculate the resulting changes in the direct and indirect Kohn-Sham bandgaps (dashed curves in Fig. 5.1 c). Surprisingly, the bandgap versus interlayer distance relation for different stacking configurations (symbols in Fig. 5.1 c) all lie on the dashed curves, which are from the AA_1 configuration at different separation. It shows that in MoS_2 bilayers, the interlayer coupling strength of the electronic states near the band edges depends only explicitly on the interlayer distance, but not on the relative horizontal lattice alignment. (We note that there is an implicit dependence because the interlayer separation varies with the horizontal lattice registration). We notice that the photoluminescence measurement of transition II energies can vary significantly for AA- and AB-stacked bilayers. Presumably, it arises from uncontrollable interlayer distance variation in the CVD-grown bilayers. For example, the thermal expansion coefficient of MoS_2 is one order of magnitude larger than the fused silica substrate that can induce a mechanical strain in the bilayer and lead to relative slipping between the two layers. This will result in a change in average distance for AA- and AB-stacked bilayers and variations of the indirect bandgap, but has little effect on bilayers with twisting angle between 0° and 60°.

Configuration	LDA interlayer distance (nm)	Van der Waals functional (PBE-D) interlayer distance (nm)
AA_1	0.61	0.62
AA_3	0.68	0.68
AB_1	0.61	0.62
AB_2	0.62	0.62
AB_3	0.68	0.68
13.2°	0.65	0.65
21.8°	0.65	0.65
38.2°	0.65	0.65
46.8°	0.65	0.65

Table 5.1: Calculated interlayer distance of MoS_2 bilayers in different configurations.

Our discovery indicates that the steric repulsion effects, which have been extensively studied in surface reactions and nano-bio interfaces, also have an important role in understanding the electronic and vibrational properties of van der Waals-coupled two-dimensional atomic layers. Our calculations show that the steric effects in two-dimensional atomic layers strongly

depend on the atomic size and the in-plane atom-atom distance. Comparing MoS_2 with graphene, it was found that not only is the size of S atoms bigger than the size of C atoms but also the in-plane S-S distance (0.32 nm) much larger than the in-plane C-C distance (0.14 nm). As a result, the steric effect is expected to be ~ 3 times stronger in MoS_2 bilayers than graphene bilayers. Still, steric effects are present in graphene bilayers in which the interlayer distance of Bernal-stacked graphene bilayers is 0.01 nm smaller than that of other twisted bilayers (See supplementary information of Ref. [9]).

5.2 Electric Field Tunable Optical Properties of Black Phosphorus Bilayers

Anisotropy describes the directional dependence of a materials properties such as transport and optical response. In conventional bulk materials, anisotropy is intrinsically related to the crystal structure and thus not tunable by the gating techniques used in modern electronics. Here we show that, in bilayer black phosphorus with an interlayer twist angle of 90°, the anisotropy of its electronic structure and optical transitions is tunable by gating [10]. Using first-principles calculations, we predict that a laboratory-accessible gate voltage can induce a hole effective mass that is 30 times larger along one Cartesian axis than along the other axis, and the two axes can be exchanged by flipping the sign of the gate voltage. This gate-controllable band structure also leads to a switchable optical linear dichroism, where the polarization of the lowest-energy optical transitions (absorption or luminescence) is tunable by gating. Thus, anisotropy is a tunable degree of freedom in twisted bilayer black phosphorus.

A recently realized 2D crystal, few-layer black phosphorus [124], has attracted a lot of attention due to its anisotropic transport and optical properties [125–129]. Few-layer black phosphorus in its natural stacking order, which has the crystalline orientations of the layers aligned parallel to one another, exhibits similar anisotropy as those of a monolayer [125–127, 130]. Here, we explore the effects of changing the relative crystalline orientation of two adjacent layers on the system's anisotropic properties, especially when the relative orientation is at the perpendicular limit (i.e., at 90°).

We performed first-principles calculations on bilayer black phosphorus with an interlayer twist angle of 90° (Fig. 5.3 a). We employ a supercell approach [131], taking the in-plane (x-y) dimension of the supercell to be 5×7 times that of a unit cell of monolayer black phosphorus, resulting in nearly commensurate top and bottom layers with a small lattice mismatch of $< 1\%$. The separation between a bilayer and its replica in the neighboring supercell is taken to be 25 Å. The relaxed interlayer distance of the 90° twisted bilayer black phosphorus is 3.3 Å (Fig. 5.3 a), which is about 0.2 Å larger than that of the naturally stacked bilayer. The reciprocal space geometry is shown in Fig. 5.3 b, in which the rectangular Brillouin zone of the naturally stacked bilayer has been folded onto the square-shaped

Brillouin zone of the supercell structure.

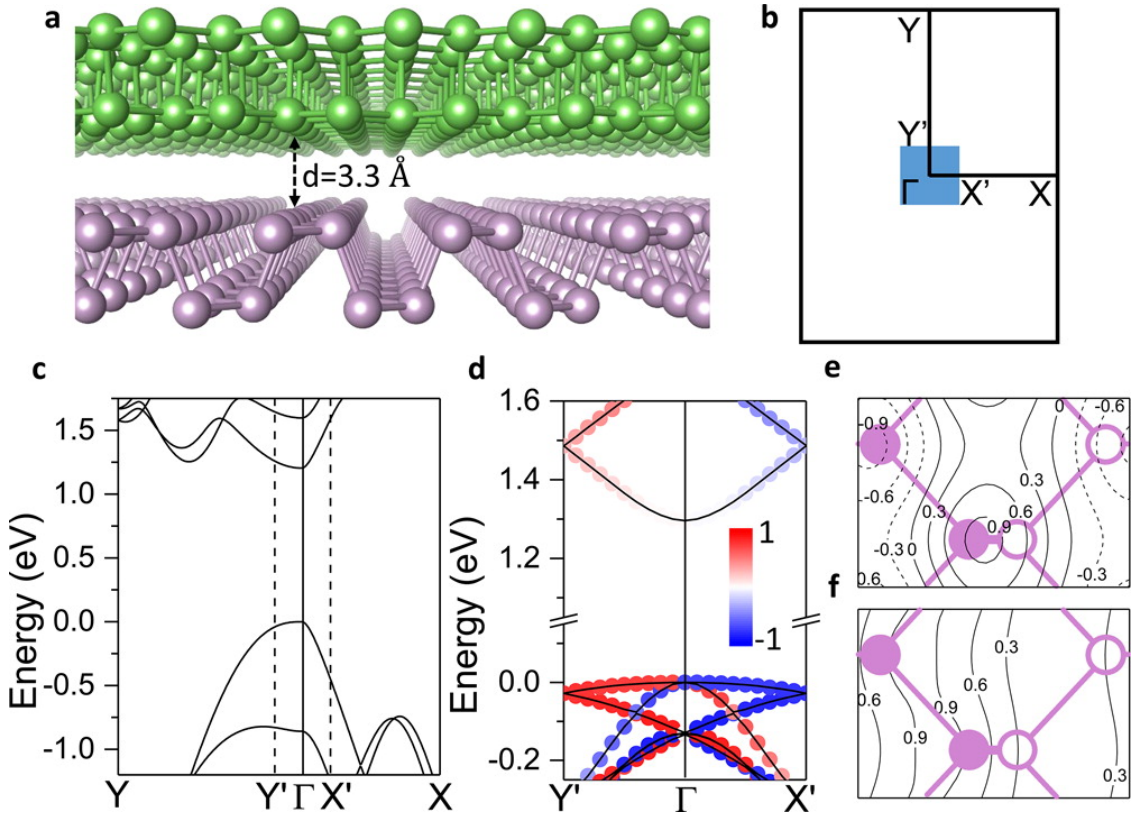

Figure 5.3: Structure and electronic structure of 90° twisted bilayer black phosphorus. (a) Structure of a 90° twisted bilayer black phosphorus. The phosphorus atoms in the top and bottom layers are colored by cyan and purple, respectively. The interlayer distance is 3.3 Å from first-principles density functional theory calculations using the PBE functional with a van der Waals correction. (b) Schematic of the Brillouin zone of bilayer black phosphorus in its natural stacking order (rectangle) and the Brillouin zone of a 5×7 supercell of 90° twisted bilayer black phosphorus (shaded square). (c) GW quasiparticle band structure of naturally stacked bilayer black phosphorus. (d) GW quasiparticle band structure of 90° twisted bilayer black phosphorus, with the color representing the layer localization function defined in the main text. (e, f) Contour plots of the wave functions of (e) The valence band maximum and (f) the conduction band minimum of a monolayer black phosphorus at a height of 1.6 Å above the phosphorus atoms, respectively. The wave function is normalized to its maximum amplitude in each plot. The solid and dashed lines represent positive and negative values of the wave functions, respectively. The solid and hollow purple circles denote the phosphorus atoms at the top and bottom of a monolayer, respectively.

The quasiparticle band structure of the 90° twisted bilayer under zero bias voltage has

4-fold rotational symmetry (and is nearly isotropic near the Γ point, the Brillouin zone center), which is distinct from that of the naturally stacked bilayer. In a naturally stacked bilayer, the quasiparticle band structure only has 2-fold rotational symmetry with a singly degenerate (not counting the spin degree of freedom) conduction band minimum (CBM) and a singly degenerate valence band maximum (VBM) at Γ (Fig. 5.3 c). Around the Γ point, the bands are considerably more dispersive along the Γ-X direction than along the Γ-Y direction, corresponding to the armchair direction and zigzag direction in real space, respectively. These singly degenerate CBM and VBM states arise because of interlayer interaction, which splits the otherwise degenerate bands from having two layers. The band splitting between interlayer bonding and antibonding orbitals for the CBM and VBM at Γ is 0.4 and 0.9 eV, respectively. However, for the 90° twisted bilayer (Fig. 5.3 d), although the CBM remains singly degenerate, a 2-fold degeneracy appears for the states at the VBM (the energy splitting is < 0.1 meV in our calculation). Moreover, the anisotropic features of the band structure disappear. The energy dispersions along the Γ-X' direction for various bands are identical as those along the Γ-Y' direction. To better illustrate the energy dispersions of bands, we plot the top valence band and the bottom conduction band as energy surfaces in the Brillouin zone, shown in Fig. 5.4.

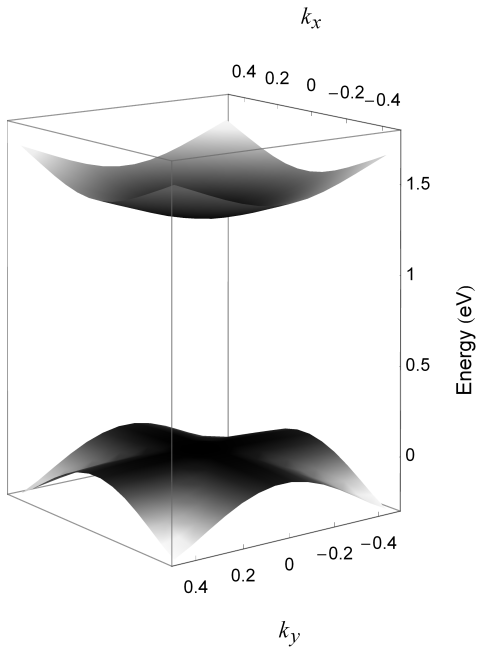

Figure 5.4: Top valence band and bottom conduction band in the first Brillouin zone of 90° twisted black phosphorus bilayer. A three-dimensional plot (energy vs. in-plane wavevector) of the top valence band and the bottom conduction band are shown.

The absence of anisotropy in the 90° twisted bilayer is accompanied by an interesting layer

texture of the quasiparticle band states: different bands have distinctly different localization of charge density on the two layers. This is illustrated by a band-index n and wavevector $\boldsymbol{k}$ dependent layer localization function $\eta_n(\boldsymbol{k})$, defined as,

$$\eta_n(\boldsymbol{k}) = \frac{\Sigma_{i\in t}|\left\langle \Psi_i|\phi_n(\boldsymbol{k})\right\rangle|^2 - \Sigma_{i\in b}|\left\langle \Psi_i|\phi_n(\boldsymbol{k})\right\rangle|^2}{\Sigma_{i\in t}|\left\langle \Psi_i|\phi_n(\boldsymbol{k})\right\rangle|^2 + \Sigma_{i\in b}|\left\langle \Psi_i|\phi_n(\boldsymbol{k})\right\rangle|^2}. \tag{5.1}$$

where $\eta_n(\boldsymbol{k})$ is the electron wave function and Ψ_i denotes an active atomic orbital i of a phosphorus atom in the top layer (t) or the bottom layer (b). $\eta_n(\boldsymbol{k})$ quantitatively depicts the spatial distribution of wave function of the electronic state, with its value ranging from -1 (i.e., the wave function completely localizes in the bottom layer) to 1 (i.e., the wave function completely localizes in the top layer). Surprisingly, although $\eta_n(\boldsymbol{k})$ is virtually 0 for all states in naturally stacked bilayer (Fig. 5.3 c), it shows large variations for different states in the 90° twisted bilayer (Fig. 5.3 d): the charge density of the states from the lowest unoccupied band near the CBM is equally distributed on both layers, whereas, for the states from the highest occupied band complex, they are separated into two sets of bands-either localized in the top layer (the red bands) or the bottom layer (the blue bands). They are akin to the bands near the VBM of a monolayer, but the two sets of bands (red and blue) are rotated in k-space by 90° with respect to each other. We therefore label these two sets of band of different spatial localizations using the nomenclature of VBt and VBb for valence band states in the top and bottom layers, respectively.

The appearance of two identical sets of valence bands, located on the different layers and rotated by 90° in k-space, arises from a lack of interlayer hybridization between the states of the two individual layers near the VBM in the 90° twisted structure. Therefore, there are two nearly independent sets of bands that are otherwise identical except for their spatial localization and dispersion. The different behavior between CBM and VBM states in the 90° twisted structure is evident by analyzing the wave function symmetry of these states. In Fig. 5.3 e and f, we plot the wave functions of the VBM and the CBM of an isolated monolayer, at a height of 1.6 Å above the phosphorus atoms. This distance corresponds to half of the interlayer separation in the bilayer case, where the wave function overlap between layers is most significant. Along the armchair direction (the horizontal direction in Fig. 5.3 e and f), the CBM wave function (Fig. 5.3 f) has the same sign, whereas the VBM wave function (Fig. 5.3 e) shows alternating positive and negative signs. Consequently, for the CBM states of the two individual layers, their interlayer couplings are always finite regardless of the twist angle. But for the VBM states of the two individual layers, their interlayer coupling become zero as the twist angle approaches 90°. A detailed analysis including the Umklapp processes in a 5×7 supercell is included in the Supporting Information of [10].

An out-of-plane electric field can shift the energy of the VBt red bands from that of the VBb blue bands by creating a potential difference between the two layers. This gate tunable

band structure change leads to a switchable effective mass anisotropy. In our calculation, the effects of gating were simulated by adding a sawtooth like potential to the supercell including the dipole corrections [132]. In Fig. 5.5 a and b, we plot the calculated quasiparticle band structure under an out-of-plane electric displacement field of 0.2 V/Å and -0.2 V/Å, as examples of positive and negative bias conditions, respectively. Under positive bias, the VBb complex (blue valence bands) shifts to higher energy compared to the VBt complex (red valence bands). As a result, the hole effective mass along the Γ-X' direction ($\sim 3.7m_0$) is considerably larger than that along the Γ-Y' direction ($\sim 0.14m_0$) at the band edge (i.e., near the new VBM), where m_0 is the electron rest mass in vacuum (Fig. 5.5 c). In comparison, as the bias switches to negative, the VBt complex (red valence bands) becomes higher in energy, resulting in a larger hole effective mass along the Γ-Y' direction than along the Γ-X' direction (Fig. 5.5 d). For carriers in states near the CBM, however, the electron effective mass remains nearly isotropic and shows less than 20% difference between the two field directions (Fig. 5.5 c and d).

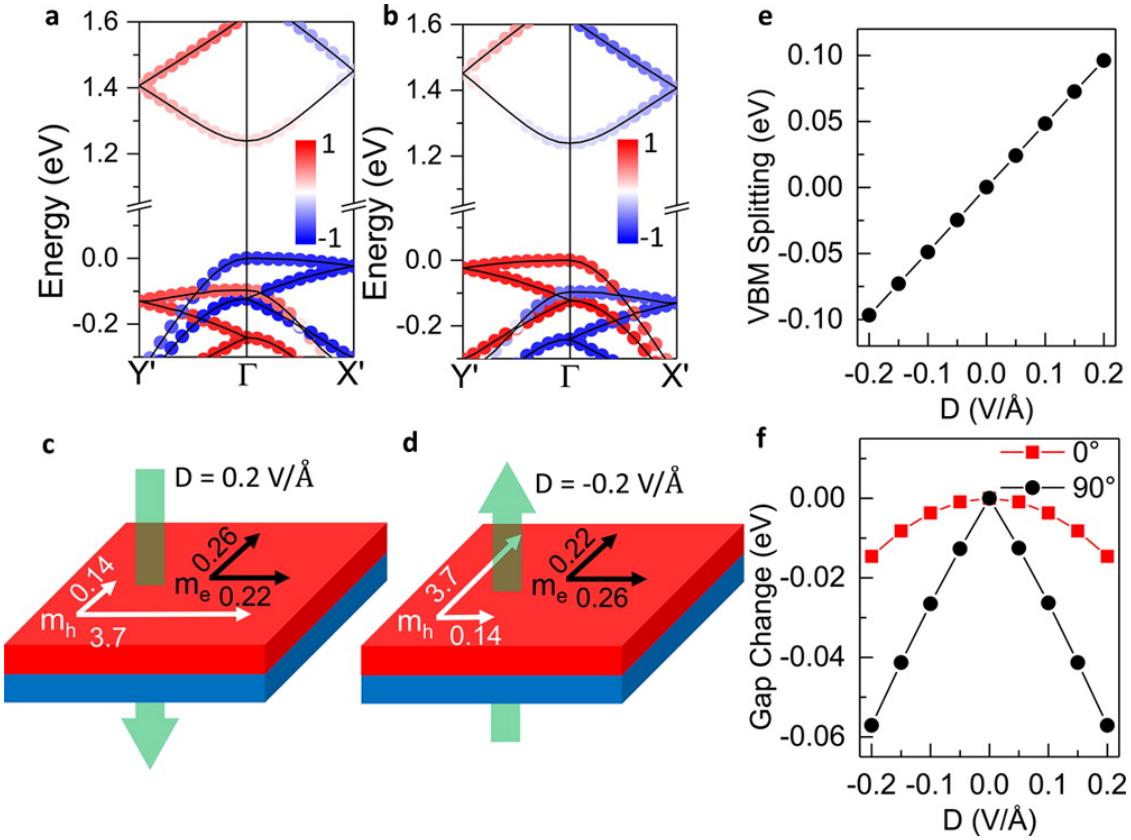

Figure 5.5: Electronic structure of the 90° twisted bilayer black phosphorus under out-of-plane electric displacement field. (a,b) GW quasiparticle band structure of the 90° twisted bilayer black phosphorus in a perpendicular electric displacement field of 0.2 V/Å and -0.2 V/Å, respectively. The color represents the layer localization function defined in the main text. (c,d) Schematics of effective mass under electric displacement field of (c) 0.2 V/Å and (d) -0.2 V/Å. The hole and electron effective masses are shown in white and black, respectively. The effective masses are in unit of the bare electron mass. The green arrow denotes the direction of the displacement field. (e) Splitting of the 2-fold degenerate valence band maximum (VBM) as a function of the electric displacement field. The lines are visual guides. (f) The change in bandgap as a function of the electric displacement field. Red squares and black circles denote the bandgap change in 0° naturally stacked bilayer and 90° twisted bilayer, respectively. The lines are visual guides.

In Fig. 5.5 e, we plot the energy difference between the VBb and the VBt at Γ as a function of the electric displacement field. The observed linear dependence in the splitting of the 2-fold degenerate level is understood as a Stark effect, splitting between two spatially separated nearly degenerate and decoupled states by an applied field. Quite remarkably, the size of the splitting, even at a relatively low field, exceeds the thermal broadening energy at

room temperature (26 meV). For example, under an electric displacement field of 0.1 V/Å, the splitting is $\sim$ 50 meV, suggesting measurable anisotropic hole transport even at room temperature. In Fig. 5.5 f, we compare the bandgap variations of the naturally stacked and 90° twisted bilayer as a function of the electric displacement field. For the naturally stacked bilayer, the bandgap variation shows a quadratic dependence on the field strength; whereas for the 90° twisted bilayer, the bandgap variation shows a close-to-linear dependence mainly due to the Stark splitting of the VBMs. Within the field strength considered in our calculations, the twisted bilayer demonstrates a higher tunability of the bandgap. For example, under a displacement field of 0.2 V/Å, the change of the bandgap in the 90° twisted bilayer, 0.1 eV, is more than 3 times larger than that in the naturally stacked bilayer.

The band structure of the 90° twisted bilayer black phosphorus also brings about two sets of optical transitions, corresponding to transitions from the VBt states to the CB and from the VBb states to the CB (Fig. 5.6 a). These two sets of optical transitions are both linearly polarized but have polarization directions perpendicular to each other. We demonstrate this effect by calculating the polarization direction dependent oscillator strength at the absorption edges, namely, $\frac{|\langle\phi_{CB}|\hat{\boldsymbol{e}}\cdot\boldsymbol{v}|\phi_{VBt}\rangle|^2}{E_{CB}-E_{VBt}}$ and $\frac{|\langle\phi_{CB}|\hat{\boldsymbol{e}}\cdot\boldsymbol{v}|\phi_{VBb}\rangle|^2}{E_{CB}-E_{VBb}}$ where the unit vector $\hat{\boldsymbol{e}}$ represents the polarization of the incident light and $\boldsymbol{v}$ the velocity operator. For optical transitions from VBt-CB, the oscillator strength is consistently 4 orders of magnitude larger for light polarized along the x axis than along the y axis, whereas those from VBb-CB show the opposite behavior. This oscillator strength difference between the two linear polarizations is robust even with an applied electric field. Fig. 5.6 b shows an example of the polarization-dependent oscillator strength of the two sets of optical transitions under an electric displacement field of 0.2 V/Å, where the two sets of transitions both demonstrate perfect linear dichroism but show orthogonal polarizations.

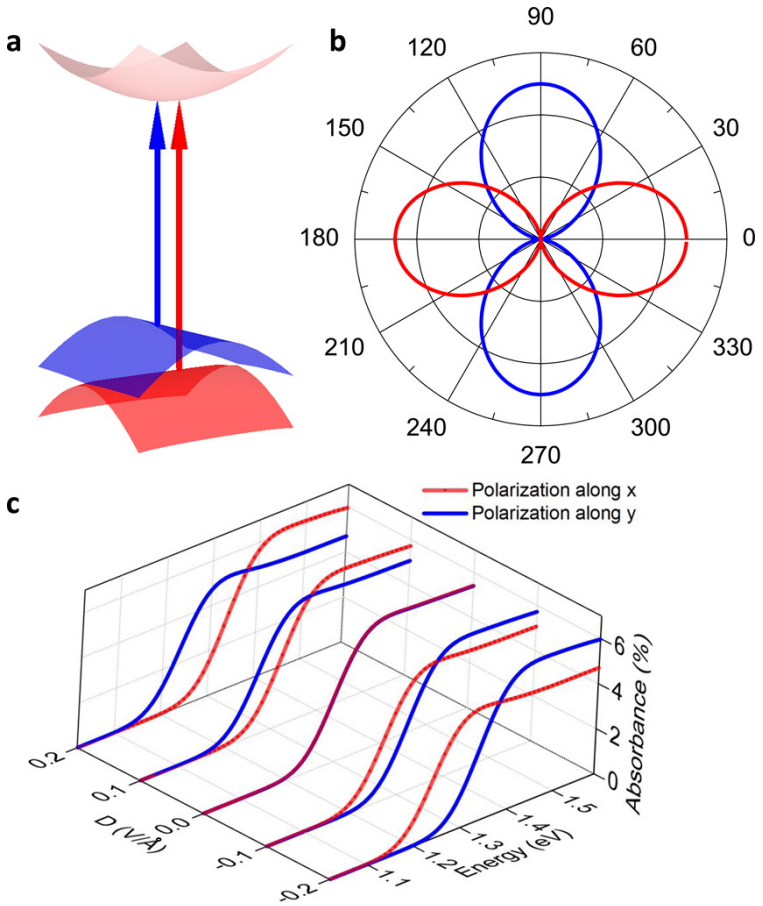

Figure 5.6: Optical transitions of the 90° twisted black phosphorus bilayer under different electric displacement field from first principles. (a) Schematic of optical transitions from VBb states to CB states (blue arrow) and VBt states to CB states (red arrow) under the electric displacement field of 0.2 V/Å. (b) Oscillator strength of optical transitions from VBb-CB (blue) and VBt-CB (red) at Γ as a function of the direction of the light polarization. The oscillator strength is plotted in arbitrary unit as a function of the polarization angle, with 0° along the x axis, and 90° along the y axis. (c) Optical absorption spectra of linearly polarized light along x-axis (red) and y-axis (blue) under electric displacement field from -0.2 V/Å to 0.2 V/Å.

Owing to the Stark splitting of the VBt and VBb complexes, the excitation energy difference between VBt-CB and VBb-CB transitions can be controlled by applying an electric field. We show the calculated optical absorption spectra with linearly polarized light along the x- and y-axes under different electric displacement fields in Fig. 5.6 c. At zero bias, the absorption spectra of light polarized along x and along y give rise to the same absorption onset at ∼1.3 eV and are identical. The optical absorbance, within this interband transition framework, is

∼5% above the absorption onset and shows a step-function feature with excitation energy, originating from the joint density of states of a direct-bandgap two-dimensional semiconductor. Applying an electric field breaks the degeneracy between the two sets of transitions, leading to higher energy absorption onset for light polarized along one axis than along the other axis (Fig. 5.6 c). Therefore, by tuning the direction of the applied electric field, the polarization of the lowest energy optical transition can be switched between two orthogonal directions. Under the electric displacement field of 0.2 V/Å, the onset energy difference between the two spectra is 0.1 eV, which is equal to the Stark splitting of the two band complexes under the same field strength (Fig. 5.5 e). Here we have not included excitonic effects in the discussion, but such effects would not change the main conclusions since the lowest energy excitons are linear combination of interband transitions of either VBt-CB or VBb-CB types with weak mixing between them because of the spatial separation of VBt and VBb hole states from each other.

The 90° twisted bilayer black phosphorus may also be used as a platform for polarization-dependent photovoltaic effects. Considering light polarized along the x-axis which excites the VBt-CB transitions, the generated photoelectrons at the CB are distributed equally in both layers, whereas the holes at the VBt are mostly localized in the top layer. This imbalanced charge carrier distribution would lead to a transient voltage drop from the top layer to the bottom layer. As this effect originates from the polarization-dependent linear dichroism, the photovoltage between the two layers can switch from positive to negative, when the polarization direction rotates from the x-axis to the y-axis. We estimate that the maximum size of the transient voltage from a photocarrier density of $10^{13}/cm^2$ is ∼0.03 V, if light is polarized along one axis.

Experimentally, samples of 90° twisted bilayer black phosphorus may be realized by stacking two monolayers with perpendicular crystalline orientations. The electric displacement field can be controlled by using a dual-gate setup, for which earlier experiments have demonstrated a tunable field strength up to 0.3 V/Å in bilayer graphene [103]. Meanwhile, as ambipolar and high mobility transport have been achieved in black phosphorus field effect transistors [124, 133], we expect that the gate-switchable, anisotropic hole effective mass may be confirmed by transport measurements with a dual-gate setup. The switchable optical linear dichroism may also be detected in polarization-dependent absorption measurements.

As a perfect alignment of the two layers at exactly 90° from each other might be difficult to achieve experimentally, we also performed calculations on bilayers with an 82° twist angle to investigate the robustness of the field switchable anisotropy with a certain misalignment. For an 82° twisted bilayer, the calculated band structure shows a small splitting of ∼ 8 meV of the otherwise 2-fold degenerate VBM at 90°. This result indicates a finite but very weak interlayer coupling of the valence band wave functions, when the interlayer twist angle deviates from 90°. However, the small splitting of ∼ 8 meV at 82° is still much smaller than the field induced Stark splitting of the VBMs separating the VBt from the VBb, which can

be as large as $\sim$ 100 meV under a displacement field of 0.2 V/Å. Therefore, the predicted switchable anisotropy is expected to be robust against an interlayer twist angle misalignment that is $\sim 10^\circ$.

As the coupling between the VBM wave functions of two native bilayers at 90°, in principle, has the same symmetry property as that between two monolayers, the field switchable anisotropy predicted here also applies to the stacking of two native bilayers. In summary, we demonstrate gate-switchable effective mass anisotropy and gate-switchable optical linear dichroism in 90° twisted bilayer black phosphorus from first-principles calculations. Our study suggests that anisotropy in stacked two-dimensional crystals may serve as a tunable degree of freedom for their future electronic and optoelectronic applications and largely increases the functionality of black phosphorus and a range of other two-dimensional materials where anisotropy exists, such as Re-based chalcogenides [134], as well as Sn- and Ge-based monochalcogenides [135].

Bibliography

1. Cao, T. *et al.* Valley-selective circular dichroism of monolayer molybdenum disulphide. *Nature Communi.* **3,** 887 (2012).
2. Xiao, D., Liu, G.-B., Feng, W., Xu, X. & Yao, W. Coupled spin and valley physics in monolayers of MoS_2 and other Group-VI dichalcogenides. *Phys. Rev. Lett.* **108,** 196802 (2012).
3. Ye, Z. *et al.* Probing excitonic dark states in single-layer tungsten disulphide. *Nature* **513,** 214–218 (2014).
4. Qiu, D. Y., Cao, T. & Louie, S. G. Nonanalyticity, valley quantum phases, and lightlike exciton dispersion in monolayer transition metal dichalcogenides: theory and first-principles calculations. *Phys. Rev. Lett.* **115,** 176801 (2015).
5. Zhang, X.-X. *et al.* Magnetic brightening and control of dark excitons in monolayer WSe_2. *Nature Nanotechnol.* **12,** 883–888 (2017).
6. Cao, T., Wu, M. & Louie, S. G. Unifying optical selection rules for excitons in two dimensions: band topology and winding numbers. *Phys. Rev. Lett.* **120,** 087402 (2018).
7. Elliott, R. Intensity of optical absorption by excitons. *Phys. Rev.* **108,** 1384 (1957).
8. Ju, L. *et al.* Tunable excitons in bilayer graphene. *Science* **358,** 907–910 (2017).
9. Liu, K. *et al.* Evolution of interlayer coupling in twisted molybdenum disulfide bilayers. *Nature Communi.* **5,** 4966 (2014).
10. Cao, T., Li, Z., Qiu, D. Y. & Louie, S. G. Gate switchable transport and optical anisotropy in 90° twisted bilayer black phosphorus. *Nano Lett.* **16,** 5542–5546 (2016).
11. Tsui, D. C., Stormer, H. L. & Gossard, A. C. Two-dimensional magnetotransport in the extreme quantum limit. *Phys. Rev. Lett.* **48,** 1559–1562 (1982).
12. Laughlin, R. B. Anomalous quantum Hall effect: an incompressible quantum fluid with fractionally charged excitations. *Phys. Rev. Lett.* **50,** 1395–1398 (1983).
13. Osheroff, D. D., Richardson, R. C. & Lee, D. M. Evidence for a new phase of solid He^3. *Phys. Rev. Lett.* **28,** 885–888 (1972).

14. Klitzing, K. v., Dorda, G. & Pepper, M. New method for high-accuracy determination of the fine-structure constant based on quantized Hall resistance. *Phys. Rev. Lett.* **45,** 494–497 (1980).
15. Sachdev, S. & Ye, J. Gapless spin-fluid ground state in a random quantum Heisenberg magnet. *Phys. Rev. Lett.* **70,** 3339–3342 (1993).
16. Maldacena, J. & Stanford, D. Remarks on the Sachdev-Ye-Kitaev model. *Phys. Rev. D* **94,** 106002 (2016).
17. Dittrich, T. *et al. Quantum transport and dissipation* (Wiley-Vch Weinheim, 1998).
18. Runge, E. & Gross, E. K. U. Density-functional theory for time-dependent systems. *Phys. Rev. Lett.* **52,** 997–1000 (1984).
19. Hedin, L. New method for calculating the one-particle Green's function with application to the electron-gas problem. *Phys. Rev.* **139,** A796–A823 (1965).
20. Hybertsen, M. S. & Louie, S. G. Electron correlation in semiconductors and insulators: Band gaps and quasiparticle energies. *Phys. Rev. B* **34,** 5390–5413 (1986).
21. Strinati, G. Application of the Green's functions method to the study of the optical properties of semiconductors. *Riv. Nuovo Cimento* **11,** 1–86 (1988).
22. Rohlfing, M. & Louie, S. G. Electron-hole excitations and optical spectra from first principles. *Phys. Rev. B* **62,** 4927–4944 (2000).
23. Hybertsen, M. S. & Louie, S. G. First-principles theory of quasiparticles: calculation of band gaps in semiconductors and insulators. *Phys. Rev. Lett.* **55,** 1418–1421 (1985).
24. Rohlfing, M. & Louie, S. G. Electron-hole excitations in semiconductors and insulators. *Phys. Rev. Lett.* **81,** 2312–2315 (1998).
25. Hohenberg, P. & Kohn, W. Inhomogeneous electron gas. *Phys. Rev.* **136,** B864–B871 (1964).
26. Kohn, W. & Sham, L. J. Self-consistent equations including exchange and correlation effects. *Phys. Rev.* **140,** A1133–A1138 (1965).
27. Metropolis, N., Rosenbluth, A. W., Rosenbluth, M. N., Teller, A. H. & Teller, E. Equation of state calculations by fast computing machines. *J. Chem. Phys.* **21,** 1087–1092 (1953).
28. Mak, K. F., Lee, C., Hone, J., Shan, J. & Heinz, T. F. Atomically thin MoS_2: a new direct-gap semiconductor. *Phys. Rev. Lett.* **105,** 136805 (2010).
29. Lee, C. *et al.* Anomalous lattice vibrations of single- and few-Layer MoS_2. *ACS Nano* **4,** 2695–2700 (2010).
30. Splendiani, A. *et al.* Emerging photoluminescence in monolayer MoS_2. *Nano Lett.* **10,** 1271–1275 (2010).
31. Mak, K. F. *et al.* Tightly bound trions in monolayer MoS_2. *Nature Mater.* **12,** 207–211 (2013).

32. Britnell, L. *et al.* Strong light-matter interactions in heterostructures of atomically thin films. *Science* **340,** 1311–1314 (2013).

33. Mak, K. F., He, K., Shan, J. & Heinz, T. F. Control of valley polarization in monolayer MoS_2 by optical helicity. *Nature Nanotechnol.* **7,** 494–498 (2012).

34. Zeng, H., Dai, J., Yao, W., Xiao, D. & Cui, X. Valley polarization in MoS_2 monolayers by optical pumping. *Nature Nanotechnol.* **7,** 490–493 (2012).

35. Rycerz, A., Tworzydło, J. & Beenakker, C. W. J. Valley filter and valley valve in graphene. *Nature Phys.* **3,** 172–175 (2007).

36. Akhmerov, A. R. & Beenakker, C. W. J. Detection of valley polarization in graphene by a superconducting contact. *Phys. Rev. Lett.* **98,** 157003 (2007).

37. Xiao, D., Yao, W. & Niu, Q. Valley-contrasting physics in graphene: magnetic moment and topological transport. *Phys. Rev. Lett.* **99,** 236809 (2007).

38. Yao, W., Xiao, D. & Niu, Q. Valley-dependent optoelectronics from inversion symmetry breaking. *Phys. Rev. B* **77,** 235406 (2008).

39. Gunawan, O. *et al.* Valley susceptibility of an interacting two-dimensional electron system. *Phys. Rev. Lett.* **97,** 186404 (2006).

40. Takashina, K., Ono, Y., Fujiwara, A., Takahashi, Y. & Hirayama, Y. Valley polarization in Si(100) at zero magnetic field. *Phys. Rev. Lett.* **96,** 236801 (2006).

41. Bishop, N. C. *et al.* Valley polarization and susceptibility of composite fermions around a filling factor $\nu = \frac{3}{2}$. *Phys. Rev. Lett.* **98,** 266404 (2007).

42. Eng, K., McFarland, R. N. & Kane, B. E. Integer quantum hall effect on a six-valley Hydrogen-passivated Silicon (111) surface. *Phys. Rev. Lett.* **99,** 016801 (2007).

43. Zhu, Z., Collaudin, A., Fauqué, B., Kang, W. & Behnia, K. Field-induced polarization of Dirac valleys in bismuth. *Nature Phys.* **8,** 89–94 (2012).

44. Giovannetti, G., Khomyakov, P. A., Brocks, G., Kelly, P. J. & van den Brink, J. Substrate-induced band gap in graphene on hexagonal boron nitride: Ab initio density functional calculations. *Phys. Rev. B* **76,** 073103 (2007).

45. Zhou, S. Y. *et al.* Substrate-induced bandgap opening in epitaxial graphene. *Nature Mater.* **6,** 770–775 (2007).

46. Ceperley, D. M. & Alder, B. J. Ground state of the electron gas by a stochastic method. *Phys. Rev. Lett.* **45,** 566–569 (1980).

47. Gajdoš, M., Hummer, K., Kresse, G., Furthmüller, J. & Bechstedt, F. Linear optical properties in the projector-augmented wave methodology. *Phys. Rev. B* **73,** 045112 (2006).

48. Karplus, R. & Luttinger, J. M. Hall effect in ferromagnetics. *Phys. Rev.* **95,** 1154–1160 (1954).

49. Chang, M.-C. & Niu, Q. Berry phase, hyperorbits, and the Hofstadter spectrum. *Phys. Rev. Lett.* **75,** 1348–1351 (1995).

50. Yao, Y. *et al.* First principles calculation of anomalous Hall conductivity in ferromagnetic bcc Fe. *Phys. Rev. Lett.* **92,** 037204 (2004).

51. Malashevich, A. & Vanderbilt, D. First principles study of improper ferroelectricity in $TbMnO_3$. *Phys. Rev. Lett.* **101,** 037210 (2008).

52. Mak, K. F., McGill, K. L., Park, J. & McEuen, P. L. The valley Hall effect in MoS_2 transistors. *Science* **344,** 1489–1492 (2014).

53. Qiu, D. Y., da Jornada, F. H. & Louie, S. G. Optical spectrum of MoS_2: many-body effects and diversity of exciton states. *Phys. Rev. Lett.* **111,** 216805 (2013).

54. Qiu, D. Y., da Jornada, F. H. & Louie, S. G. Erratum: Optical spectrum of MoS_2: Many-body effects and diversity of exciton states [Phys. Rev. Lett. 111, 216805 (2013)]. *Phys. Rev. Lett.* **115,** 119901 (2015).

55. Chernikov, A. *et al.* Exciton binding energy and nonhydrogenic Rydberg series in monolayer WS_2. *Phys. Rev. Lett.* **113,** 076802 (2014).

56. He, K. *et al.* Tightly bound excitons in monolayer WSe_2. *Phys. Rev. Lett.* **113,** 026803 (2014).

57. Ugeda, M. M. *et al.* Giant bandgap renormalization and excitonic effects in a monolayer transition metal dichalcogenide semiconductor. *Nature Mater.* **13,** 1091–1095 (2014).

58. Deslippe, J. *et al.* BerkeleyGW: A massively parallel computer package for the calculation of the quasiparticle and optical properties of materials and nanostructures. *Comput. Phys. Commun.* **183,** 1269 –1289 (2012).

59. Deslippe, J. *et al.* Electron-hole interaction in carbon nanotubes: novel screening and exciton excitation spectra. *Nano Lett.* **9,** 1330–1334 (2009).

60. Keldysh, L. Coulomb interaction in thin semiconductor and semimetal films. *JETP Lett.* **29,** 658 (1979).

61. Zhou, J., Shan, W.-Y., Yao, W. & Xiao, D. Berry phase modification to the energy spectrum of excitons. *Phys. Rev. Lett.* **115,** 166803 (2015).

62. Srivastava, A. & Imamoğlu, A. Signatures of Bloch-band geometry on excitons: nonhydrogenic spectra in transition-metal dichalcogenides. *Phys. Rev. Lett.* **115,** 166802 (2015).

63. Beal, A., Knights, J. & Liang, W. Transmission spectra of some transition metal dichalcogenides. II. Group VIA: trigonal prismatic coordination. *J. Phys. C: Solid State Physics* **5,** 3540 (1972).

64. Knox, R. S. Theory of excitons. *Solid State Phys.* **5** (1963).

65. Wang, F., Dukovic, G., Brus, L. E. & Heinz, T. F. The optical resonances in carbon nanotubes arise from excitons. *Science* **308,** 838–841 (2005).

66. Spataru, C. D., Ismail-Beigi, S., Benedict, L. X. & Louie, S. G. Excitonic effects and optical spectra of single-walled carbon nanotubes. *Phys. Rev. Lett.* **92,** 077402 (2004).

67. Yang, L., Cohen, M. L. & Louie, S. G. Excitonic effects in the optical spectra of graphene nanoribbons. *Nano Lett.* **7,** 3112–3115 (2007).

68. Ishihara, T., Takahashi, J. & Goto, T. Optical properties due to electronic transitions in two-dimensional semiconductors $(C_nH_{2n+1}NH_3)_2PbI_4$. *Phys. Rev. B* **42,** 11099–11107 (1990).

69. Yu, H., Liu, G.-B., Gong, P., Xu, X. & Yao, W. Dirac cones and Dirac saddle points of bright excitons in monolayer transition metal dichalcogenides. *Nature Communi.* **5,** 3876 (2014).

70. Wu, F., Qu, F. & MacDonald, A. H. Exciton band structure of monolayer MoS_2. *Phys. Rev. B* **91,** 075310 (2015).

71. Yu, T. & Wu, M. W. Valley depolarization due to intervalley and intravalley electron-hole exchange interactions in monolayer MoS_2. *Phys. Rev. B* **89,** 205303 (2014).

72. Zhu, Z. Y., Cheng, Y. C. & Schwingenschlögl, U. Giant spin-orbit-induced spin splitting in two-dimensional transition-metal dichalcogenide semiconductors. *Phys. Rev. B* **84,** 153402 (2011).

73. Glazov, M. M. *et al.* Exciton fine structure and spin decoherence in monolayers of transition metal dichalcogenides. *Phys. Rev. B* **89,** 201302 (2014).

74. Zhang, X.-X., You, Y., Zhao, S. Y. F. & Heinz, T. F. Experimental evidence for dark excitons in monolayer WSe_2. *Phys. Rev. Lett.* **115,** 257403 (2015).

75. Liu, G.-B., Shan, W.-Y., Yao, Y., Yao, W. & Xiao, D. Three-band tight-binding model for monolayers of group-VIB transition metal dichalcogenides. *Phys. Rev. B* **88,** 085433 (2013).

76. Kormányos, A. *et al.* k· p theory for two-dimensional transition metal dichalcogenide semiconductors. *2D Mater.* **2,** 022001 (2015).

77. Withers, F. *et al.* WSe_2 light-emitting tunneling transistors with enhanced brightness at room temperature. *Nano Lett.* **15,** 8223–8228 (2015).

78. Wang, G. *et al.* Spin-orbit engineering in transition metal dichalcogenide alloy monolayers. *Nature Communi.* **6,** 10110 (2015).

79. Li, Y. *et al.* Valley splitting and polarization by the Zeeman effect in monolayer $MoSe_2$. *Phys. Rev. Lett.* **113,** 266804 (2014).

80. Srivastava, A. *et al.* Valley Zeeman effect in elementary optical excitations of monolayer WSe_2. *Nature Phys.* **11,** 141–147 (2015).

81. MacNeill, D. *et al.* Breaking of valley degeneracy by magnetic field in monolayer $MoSe_2$. *Phys. Rev. Lett.* **114,** 037401 (2015).

82. Wang, Z., Shan, J. & Mak, K. F. Valley- and spin-polarized Landau levels in monolayer WSe_2. *Nature Nanotechnol.* **12,** 144–149 (2017).

83. Bayer, M., Stern, O., Kuther, A. & Forchel, A. Spectroscopic study of dark excitons in $In_xGa_{1-x}As$ self-assembled quantum dots by a magnetic-field-induced symmetry breaking. *Phys. Rev. B* **61,** 7273–7276 (2000).

84. Zaric, S. *et al.* Optical Signatures of the Aharonov-Bohm Phase in Single-Walled Carbon Nanotubes. *Science* **304,** 1129–1131 (2004).

85. Glasberg, S., Shtrikman, H., Bar-Joseph, I. & Klipstein, P. C. Exciton exchange splitting in wide GaAs quantum wells. *Phys. Rev. B* **60,** R16295–R16298 (1999).

86. Thouless, D. J., Kohmoto, M., Nightingale, M. P. & den Nijs, M. Quantized Hall conductance in a two-dimensional periodic potential. *Phys. Rev. Lett.* **49,** 405–408 (1982).

87. Mermin, N. D. The topological theory of defects in ordered media. *Rev. Mod. Phys.* **51,** 591–648 (1979).

88. Qi, X.-L. & Zhang, S.-C. Topological insulators and superconductors. *Rev. Mod. Phys.* **83,** 1057–1110 (2011).

89. Hasan, M. Z. & Kane, C. L. Colloquium: Topological insulators. *Rev. Mod. Phys.* **82,** 3045–3067 (2010).

90. Bernevig, B. A., Hughes, T. L. & Zhang, S.-C. Quantum spin Hall effect and topological phase transition in HgTe quantum wells. *Science* **314,** 1757–1761 (2006).

91. Kane, C. L. & Mele, E. J. Quantum spin Hall effect in graphene. *Phys. Rev. Lett.* **95,** 226801 (2005).

92. Essin, A. M., Moore, J. E. & Vanderbilt, D. Magnetoelectric polarizability and axion electrodynamics in crystalline insulators. *Phys. Rev. Lett.* **102,** 146805 (2009).

93. Dresselhaus, G. Effective mass approximation for excitons. *J. Phys. Chem. Sol.* **1,** 14–22 (1956).

94. Cohen, M. L. & Louie, S. G. *Fundamentals of condensed matter physics* (Cambridge University Press, 2016).

95. Gross, E. F. Optical spectrum of excitons in the crystal lattice. *Il Nuovo Cimento (1955-1965)* **3,** 672–701 (1956).

96. McCann, E. & Koshino, M. The electronic properties of bilayer graphene. *Rep. Prog. Phys.* **76,** 056503 (2013).

97. Sui, M. *et al.* Gate-tunable topological valley transport in bilayer graphene. *Nature Phys.* **11,** 1027–1031 (2015).

98. Ju, L. *et al.* Topological valley transport at bilayer graphene domain walls. *Nature* **520,** 650–655 (2015).

99. Zhang, F., MacDonald, A. H. & Mele, E. J. Valley Chern numbers and boundary modes in gapped bilayer graphene. *Proc. Natl. Acad. Sci. USA* **110,** 10546–10551 (2013).

100. Zhang, X., Shan, W.-Y. & Xiao, D. Optical selection rule of excitons in gapped chiral fermion systems. *Phys. Rev. Lett.* **120,** 077401 (2018).

101. Bao, W. *et al.* Stacking-dependent band gap and quantum transport in trilayer graphene. *Nature Phys.* **7,** 948–952 (2011).

102. Lui, C. H., Li, Z., Mak, K. F., Cappelluti, E. & Heinz, T. F. Observation of an electrically tunable band gap in trilayer graphene. *Nature Phys.* **7,** 944–947 (2011).

103. Zhang, Y. *et al.* Direct observation of a widely tunable bandgap in bilayer graphene. *Nature* **459,** 820–823 (2009).

104. Gorbachev, R. *et al.* Detecting topological currents in graphene superlattices. *Science* **346,** 448–451 (2014).

105. Giannozzi, P. *et al.* QUANTUM ESPRESSO: a modular and open-source software project for quantum simulations of materials. *J. Phys. Condens. Matter* **21,** 395502 (2009).

106. Park, C.-H. & Louie, S. G. Tunable excitons in biased bilayer graphene. *Nano Lett.* **10,** 426–431 (2010).

107. Yan, J.-A., Ruan, W. Y. & Chou, M. Y. Phonon dispersions and vibrational properties of monolayer, bilayer, and trilayer graphene: Density-functional perturbation theory. *Phys. Rev. B* **77,** 125401 (2008).

108. Xu, X., Yao, W., Xiao, D. & Heinz, T. F. Spin and pseudospins in layered transition metal dichalcogenides. *Nature Phys.* **10,** 343–350 (2014).

109. Xiao, J. *et al.* Nonlinear optical selection rule based on valley-exciton locking in monolayer WS_2. *Light Sci. Appl.* **4,** e366 (2015).

110. Hong, H. *et al.* Interfacial engineering of van der Waals coupled 2D layered materials. *Adv. Mater. Interf.* **4,** 1601054 (2017).

111. Li, G. *et al.* Observation of van Hove singularities in twisted graphene layers. *Nature Phys.* **6,** 109–113 (2010).

112. Jiang, T. *et al.* Valley and band structure engineering of folded MoS_2 bilayers. *Nature Nanotechnol.* **9,** 825–829 (2014).

113. Van Der Zande, A. M. *et al.* Tailoring the electronic structure in bilayer molybdenum disulfide via interlayer twist. *Nano Lett.* **14,** 3869–3875 (2014).

114. Wu, S. *et al.* Electrical tuning of valley magnetic moment through symmetry control in bilayer MoS_2. *Nature Phys.* **9,** 149–153 (2013).

115. Geim, A. K. & Grigorieva, I. V. Van der Waals heterostructures. *Nature* **499,** 419–425 (2013).

116. Novoselov, K. S., Mishchenko, A., Carvalho, A. & Castro Neto, A. H. 2D materials and van der Waals heterostructures. *Science* **353,** aac9439 (2016).

117. Bistritzer, R. & MacDonald, A. H. Moiré bands in twisted double-layer graphene. *Proc. Natl. Acad. Sci. USA* **108,** 12233–12237 (2011).

118. Cao, Y. *et al.* Correlated insulator behaviour at half-filling in magic-angle graphene superlattices. *Nature* **556,** 80–84 (2018).

119. Cao, Y. *et al.* Unconventional superconductivity in magic-angle graphene superlattices. *Nature* **556,** 43–50 (2018).

120. Ugeda, M. M. *et al.* Characterization of collective ground states in single-layer $NbSe_2$. *Nature Phys.* **12,** 92–97 (2016).

121. Xi, X. *et al.* Strongly enhanced charge-density-wave order in monolayer $NbSe_2$. *Nature Nanotechnol.* **10,** 765–769 (2015).

122. Gong, C. *et al.* Discovery of intrinsic ferromagnetism in two-dimensional van der Waals crystals. *Nature* **546,** 265–269 (2017).

123. Huang, B. *et al.* Layer-dependent ferromagnetism in a van der Waals crystal down to the monolayer limit. *Nature* **546,** 270–273 (2017).

124. Li, L. *et al.* Black phosphorus field-effect transistors. *Nature Nanotechnol.* **9,** 372–377 (2014).

125. Qiao, J., Kong, X., Hu, Z.-X., Yang, F. & Ji, W. High-mobility transport anisotropy and linear dichroism in few-layer black phosphorus. *Nature Communi.* **5,** 4475 (2014).

126. Wang, X. *et al.* Highly anisotropic and robust excitons in monolayer black phosphorus. *Nature Nanotechnol.* **10,** 517–521 (2015).

127. Xia, F., Wang, H. & Jia, Y. Rediscovering black phosphorus as an anisotropic layered material for optoelectronics and electronics. *Nature Communi.* **5,** 4458 (2014).

128. Yuan, H. *et al.* Polarization-sensitive broadband photodetector using a black phosphorus vertical p–n junction. *Nature Nanotechnol.* **10,** 707–713 (2015).

129. Fei, R. & Yang, L. Strain-Engineering the Anisotropic Electrical Conductance of Few-Layer Black Phosphorus. *Nano Lett.* **14,** 2884–2889 (2014).

130. Tran, V., Soklaski, R., Liang, Y. & Yang, L. Layer-controlled band gap and anisotropic excitons in few-layer black phosphorus. *Phys. Rev. B* **89,** 235319 (2014).

131. Cohen, M. L., Schlüter, M., Chelikowsky, J. R. & Louie, S. G. Self-consistent pseudopotential method for localized configurations: Molecules. *Phys. Rev. B* **12,** 5575–5579 (1975).

132. Bengtsson, L. Dipole correction for surface supercell calculations. *Phys. Rev. B* **59,** 12301–12304 (1999).

133. Koenig, S. P., Doganov, R. A., Schmidt, H., Castro Neto, A. H. & Oezyilmaz, B. Electric field effect in ultrathin black phosphorus. *Appl. Phys. Lett.* **104,** 103106 (2014).

134. Aslan, O. B., Chenet, D. A., van der Zande, A. M., Hone, J. C. & Heinz, T. F. Linearly polarized excitons in single- and few-layer ReS_2 crystals. *ACS Photonics* **3,** 96–101 (2016).

135. Shi, G. & Kioupakis, E. Anisotropic spin transport and strong visible-light absorbance in few-layer SnSe and GeSe. *Nano Lett.* **15,** 6926–6931 (2015).